

**BINARY COLLISION AND MOLECULAR DYNAMICS SIMULATION OF Fe-  
Ni-Cr ALLOYS AT SUPERCRITICAL WATER CONDITION**

**A THESIS PRESENTED TO DEPARTMENT OF NUCLEAR ENGINEERING,  
SCHOOL OF NUCLEAR AND ALLIED SCIENCES  
COLLEGE OF BASIC AND APPLIED SCIENCES,  
UNIVERSITY OF GHANA**

**BY**

**COLLINS NANA ANDOH (ID: 10443957)**

**B.Sc. (CAPE COAST), 2010**

**IN PARTIAL FULFILMENT OF THE REQUIREMENT FOR THE DEGREE OF**

**MASTER OF PHILOSOPHY**

**IN**

**COMPUTATIONAL NUCLEAR SCIENCES AND ENGINEERING**

**JULY, 2015**

## DECLARATION

I hereby declare that with the exception of references to other people's work which has been duly acknowledged, this thesis is the result of my own research work and no part of it has been presented for another degree in this University or elsewhere.

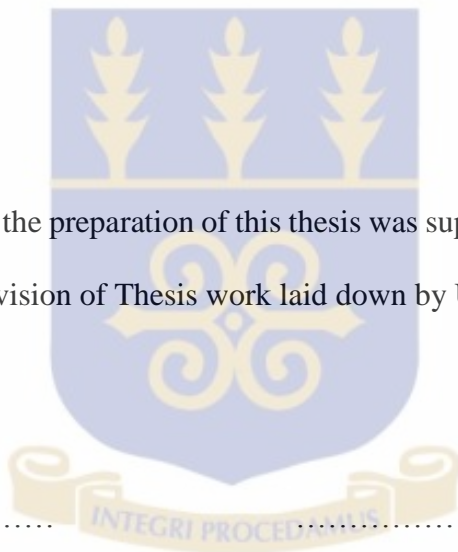
.....

**Date**.....

**COLLINS NANA ANDOH**

**(Student)**

We hereby declare that the preparation of this thesis was supervised in accordance with the guidelines of the supervision of Thesis work laid down by University of Ghana.



.....

**Dr. G.K. BANINI**

**(PRINCIPAL SUPERVISOR)**

**NANA (Prof.) A. AYENSU GYEABOUR I**

**(Co-SUPERVISOR)**

Date.....

Date.....

## ABSTARCT

Fe-Ni-Cr alloys are commonly used as pressure vessel (in-core) materials for nuclear reactors and have been classified as candidate materials for Supercritical Water-Cooled Reactors (SCWR). In service, the in-core materials are exposed to harsh environments: intense neutron irradiation, mechanical and thermal stresses, and aggressive corrosion prone environment which all contribute to the components' deterioration. For better understanding of the mechanisms responsible for degradation of the Fe-Ni-Cr alloys (SS304, SS308, SS309 and SS316) under high neutron irradiation dose, pressure and temperature conditions as pertains in SCWR conditions, these alloys were examined using Binary collision and molecular dynamics simulations using (SRIM-TRIM code and LAMMPS, VMD codes) respectively. The neutron irradiation damage assessments were conducted under irradiation doses of 30 dpa (thermal neutron spectrum) and 150 dpa (fast neutron spectrum). The results indicated that more defects were generated in the fast neutron spectrum SCWR than in the thermal neutron spectrum, and the depth of penetration of neutron in the fast spectrum was (32.3  $\mu\text{m}$ ) about three times that of the thermal spectrum ( $\sim 11.3 \mu\text{m}$ ). The work revealed that there was a marginal difference of 97.18 % of the neutron energy loss in SS308 compared to 97.14 % in SS316 and SS309.

The evaluation of mechanical deterioration revealed that Young's Modulus, Ultimate Tensile Strength and the Breaking/Fracture Strength decreased with increasing temperature. The SS308 and SS304 two materials had very high ultimate tensile strengths and breaking strengths even at the temperature of 500 °C. By linking the neutron damage assessment and the mechanical evaluation, SS304 and SS308 could be considered in the design of the SCWR pressure vessel and couplings since the SS308 was found to be least

damaged by the neutron irradiation whiles SS304 had high breaking strength. However, further research is recommended on the two Fe-Ni-Cr alloys SS308 and SS304 on hydrogen embrittlement, swelling, creep, as well as corrosion studies upon interactions with supercritical water environment; an extensive testing and evaluation program is required to assess the corrosion effects on the material properties of these two materials.



## DEDICATION

I dedicate this thesis work to my father, Mr. Paul Nana Andoh, who after all his health problems stood firm to help me finish this Master's Degree, his brother Peter Adansi Andoh, and my step mother Victoria Okyere whose encouragement has brought me this far. Finally, to my son Allswel Nana Andoh and my two grandmothers Asi Kumiwaa and Esi Asiedua (Esi Kakraba) who have been on their knees praying for my success throughout my education.



## **ACKNOWLEDGEMENTS**

I am very thankful to God Almighty for giving me the strength to undertake this study. My sincere gratitude goes to my supervisors, Nana (Prof) A. Ayensu Gyeabour I and Dr. G. K. Banini for their tolerance, encouragement, priceless advice, constructive criticisms and kind supervision.

I am also thankful to all my siblings, colleagues (especially my roommates Maruf Abubakar and Ernest Kwame Ampomah) and friends for their guidance, fruitful discussions and outstanding assistance offered me in completing this thesis.

I am also grateful to Mr. Raymond Oteng-Appiagyei for his advice and to Mr. Isaac Benkyi, University of Helsinki, Finland for guidance in the applications of the LAMMPS code which is being used the first time at Graduate School of Nuclear and Allied Sciences, University of Ghana.

<b>TABLE OF CONTENTS</b>	<b>Page No.</b>
DECLARATION .....	ii
ABSTRACT .....	iii
DEDICATION .....	v
ACKNOWLEDGEMENTS .....	vi
TABLE OF CONTENTS .....	vii
LIST OF FIGURES .....	xiii
LIST OF TABLES .....	xviii
ABBREVIATIONS .....	xix
LIST OF SYMBOLS .....	xx
<b>CHAPTER ONE: INTRODUCTION</b> .....	<b>1</b>
1.1 RESEARCH BACKGROUND .....	1
1.2 RESEARCH PROBLEM STATEMENT .....	2
1.3 RESEARCH JUSTIFICATION .....	2
1.4 RESEARCH GOAL .....	3
1.5 RESEARCH OBJECTIVES .....	3
1.6 SCOPE OF RESEARCH .....	4
<b>CHAPTER TWO: LITERATURE REVIEW</b> .....	<b>5</b>
2.1 SUPERCRITICAL WATER CONDITION .....	5
2.2 DESIGN PARAMETERS FOR PRESSURE VESSEL OF SCWR .....	6
2.3 MATERIALS CHALLENGES WITH SCWR .....	8
2.3.1 Material Needs of SCWR Design .....	8

2.3.2	Candidate In-core Structural Materials of SCWR .....	9
2.3.3	Structural Integrity of Irradiated Materials .....	10
2.4	IRRADIATION DAMAGE ASESMENT .....	10
2.4.1	Irradiation Damage Events and Mechanisms.....	10
2.4.2	Rate of Production of Displacement.....	13
2.4.3	Kinchin – Pease Model of Radiation Damage.....	16
2.4.3.1	Displacement Probabilty.....	16
2.4.3.2	Displacement Energy .....	18
2.4.3.3	Radiation Damage.....	18
2.4.4	Norgett-Robinson-Torrens Model of Radiation Damage.....	24
2.4.5	Radiation Damage Defects .....	25
2.5	MECHANICAL PROPERTIES OF PRESSURE VESSEL MATERIALS....	27
2.5.1	Stainless Steels Alloys for Pressure Vessel and In-core Structure.....	28
2.5.2	Austenitic Stainless Steel .....	28
2.5.3	Effects of Irradiation on Physical Properties of Steels .....	29
2.5.4	Mechanical Strength Parameters.....	30
2.5.4.1	Youngs Modulus.....	31
2.5.4.2	Tensile Strength .....	31
2.5.4.3	Fracture or BreakingStrength.....	32
2.5.4.4	Yield Strength.....	32
2.6	COMPUTER SIMULATION CODES FOR IRRADIATION DAMAGE AND INDUCED MECHANICAL DEGRADATION.....	33
2.6.1	Binary Collision Approximation (BCA) Method.....	33



2.6.2.	Molecular Dynamics (MD) Method .....	36
2.6.3.	Kinetic Monte Carlo (KMC).....	39
2.6.4	Computer Simulation codes .....	39
2.6.4.1	SRIM-TRIM .....	39
2.6.4.2.	Large –Scale Atomic/Molecular Massively Parallel Simulator (LAMMPS) .....	41
2.6.4.3	Visual Molecular Dynamics (VMD) .....	42
<b>CHAPTER THREE:</b>	<b>RESEARCH METHODOLOGY .....</b>	<b>43</b>
3.1	SELECTION OF Fe-Ni-Cr ALLOYS .....	43
3.1.1	Structural and In-core Materials .....	43
3.1.2	Characterization and Properties of Selected Alloys.....	45
3.2	NEUTRON IRRADIATION DAMAGE ASSESSMENT BY BCA .....	46
3.2.1	Estimation of Energy Level at 30 dpa of Thermal Neutrons Spectrum .....	46
3.2.2	Estimation of Energy Level at 150 dpa of fast Neutrons Spectrum .....	47
3.2.3	SRIM-TRIM Setup and Input Requirements .....	47
3.2.4	SRIM-TRIM code Simulation Algorithm and Flowchart.....	53
3.2.5	SRIM – TRIM Simulation Implementation.....	55
3.2.6	SRIM-TRIM Output files .....	56
3.3	EVALUATION OF MECHANICAL DEGRADATION OF ALLOYS...57	
3.3.1	LAMMPS Setup and Input Requirements .....	57
3.3.2	Interatomic Potential Developed for MD Simulation.....	59

3.3.3	LAMMPS Simulation Algorithm .....	63
3.3.4	Implementation of LAMMPS Simulation .....	65
3.3.5	Output of LAMMPS Simulation.....	66
3.3.6	Visualization of Output of Simulation by VMD and MATLAB ...	67
<b>CHAPTER FOUR: RESULTS AND DISCUSSIONS.....</b>		<b>68</b>
4.1.	THERMAL AND FAST NEUTRON IRRADIATION DAMAGE IN 304 Fe-Ni-Cr ALLOY .....	68
4.1.1	Collision Cascade.....	68
4.1.2	Projected Neutron Range Distribution.....	69
4.1.3	Lateral Neutron Range Distribution.....	70
4.1.4	Ionization Energy Distribution .....	71
4.1.5	Phonons.....	73
4.1.6	Neutron Energy to Recoil Distribution .....	74
4.1.7	Collision Events .....	75
4.1.8	Sputtering Yield .....	77
4.2.	EVALUATION OF MECHANICAL DETORIORATION OF Fe-Ni- Cr ALLOYS .....	78
4.2.1	Cohesive Energy of the Fe-Ni-Cr Potential File.....	78
4.2.2	VMD Output for the Tensile Deformation .....	79
4.2.3	Stress-Strain Plots at Ambient and Supercritical Conditions .....	80
4.2.4	Mechanical Properties of Fe-Ni-Cr Alloy.....	83
4.3.	DISCUSSION .....	85
4.3.1	General Discussion .....	85

4.3.2	Discussion on Neutron Irradiation Damage.....	87
4.3.2.1	Projected Neutron Range .....	87
4.3.2.2	Energy Loss to Ionization .....	87
4.3.2.3	Fe-Ni-Cr alloy's Energy Loss to Phonon.....	88
4.3.2.4	Energy Loss to Vacancy creations in Fe-Ni-Cr alloys .....	89
4.3.2.5	Energy to Recoil Cascade .....	89
4.3.2.6	Sputtering Yield .....	90
4.3.3	Discussion on Mechanical Detorioration .....	91
4.3.3.1	Cohesive Energy .....	91
4.3.3.2	Young's Modulus.....	91
4.3.3.3	Yield Strength .....	92
4.3.3.4	Ultimate Tensile Strength .....	92
4.3.3.5	Breaking or Fracture Strength.....	93
4.3.4	Discussion on Linking of the Neutron Irradiation Damage and Mechanical Detorioration .....	94
<b>CHAPTER FIVE: CONCLUSIONS AND RECOMENDATIONS .....</b>		<b>95</b>
5.1	CONCLUSIONS .....	95
5.2	RECOMENDATIONS .....	97
<b>REFERENCES.....</b>		<b>98</b>
<b>APPENDICES .....</b>		<b>106</b>
<b>APPENDIX I: SRIM–TRIM simulation: input and output spectra from neutron Irradiation Damage Assessment of Fe-Ni-Cr Alloys.....</b>		<b>106</b>

<b>APPENDIX II:</b>	Input files for Molecular Dynamics Simulation of Mechanical Damage Assessment .....	107
<b>APPENDIX III:</b>	Algorithm for Animation of Tensile Deformation Using VMD .....	110
<b>APPENDIX IV:</b>	SRIM–TRIM Simulation Output Spectra for Neutron Irradiation Damage Assessment of Fe-Ni-Cr Alloys.....	111
<b>APPENDIX V:</b>	Comparison of the Neutron Irradiation Damage Assessment of Fe-Ni-Cr Alloys under Thermal and Fast Neutron Spectrum of the SCWR.....	131
<b>APPENDIX VI:</b>	Output files of Molecular Dynamics Simulation of Mechanical Damage Assessment of Fe-Ni-Cr Alloys.....	132
<b>APPENDIX VII:</b>	Mechanical Properties of the Fe-Ni-Cr Alloys under Ambient Temperature and Supercritical Water Conditions.....	139

**LIST OF FIGURES**

<b>Title</b>	<b>Page No.</b>
Figure 2.1: Phase Diagram of SCW condition	5
Figure 2.2: Conceptual Design of SCWR	6
Figure 2.3: Mechanism of irradiation damage in the nuclear reactor system	12
Figure 2.4: The displacement probability $P_d(T)$ as function of the transferred kinetic energy, assuming (a) a sharp or (b) a smoothly varying displacement threshold	17
Figure 2.5: Average number of displacements $v(T)$ produced by a PKA, as a function of the recoil energy $T$ according to the model of Kinchin -Pease	23
Figure 2.6: Radiation damage defects processes	26
Figure 2.7: Defects in the lattice structure of materials that can change their material properties	27
Figure 2.8: A typical Stress-Strain Curve for Fe-Ni-Cr Alloys	30
Figure 2.9: The trajectory of two particles interacting according to a conservative central repulsive force in the laboratory system	34
Figure 2.10: Molecular Dynamics Simulation flow chart	37
Figure 2.11: Molecular Dynamics Simulation of a unit cell of the material	38
Figure 3.1: Phase diagram of Stainless Steel Alloys	44
Figure 3.2: TRIM Input Parameter Window showing all inputs for Stainless Steel grade 316 assessment	48

Figure 3.3: SRIM – TRIM Code flowchart for simulation	55
Figure 3.4: Steps followed in designing LAMMPS input file	58
Figure 3.5: Graphical representation of the periodic boundary conditions. The arrows indicate the velocities of atoms. The atoms could interact with atoms in the neighboring boxes without having any boundary effects.	62
Figure 3.6: Command prompt loop for LAMMPS Simulation	63
Figure 3.7: On screen view of Output values from Simulation	64
Figure 3.8: (a) The crystal structure of an FCC lattice and (b) the (100) orientation in the x, y and z direction where the uniaxial deformation was applied.	65
Figure 4.1: Collision Cascade window for (a) thermal and (b) fast neutron irradiation damage in Fe-Ni-Cr alloy SS304	68
Figure 4.2: Projected Range of (a) thermal and (b) fast neutrons in Fe-Ni-Cr Alloy SS304	70
Figure 4.3: The lateral Range distribution of the (a) thermal and (b) fast neutrons in Fe-Ni-Cr Alloy SS304	71
Figure 4.4: 2D view of the Ionization energy distribution of (a) thermal neutrons as compared with the (b) fast neutrons (c) and (d) 3D view of the Ionization energy distribution in the Fe-Ni-Cr alloy SS304	72
Figure 4.5: Distribution of (a) thermal and (b) fast neutrons energy loss to	74

## Fe-Ni-Cr Alloy SS304 phonons

Figure 4.6: Distribution of Energy absorbed by the SS304 Fe-Ni-Cr Alloys elements in the two different spectra.	75
Figure 4.7: 2D view of the collision events of (a) thermal and (b) fast neutron spectrum, (c) and (d) gives 3D view of the collision events	77
Figure 4.8: Distribution of integral sputtering yield of Fe-Ni-Cr Alloy SS304 in (a) thermal and (b) fast neutron spectrum	78
Figure 4.9: VMD Snapshot showing Fe-Ni-Cr alloy model of size 10 Å x 10 Å x 10 Å (No. of atoms 4000)	79
Figure 4.10: Stress- Strain curve showing all the Mechanical Properties of the Fe-Ni-Cr Alloy, SS 304 under Ambient Conditions	80
Figure 4.11: Stress-Strain plot for Fe-Ni-Cr Alloys at Ambient Condition and Supercritical Water Condition at strain rate of $5 \times 10^{10} \text{ s}^{-1}$ for (a) SS304 (b) SS308 (c) SS309 and (b) SS316	81
Figure 4.12: Variation of (a) Young's Modulus (b) Yield Strength (c) Ultimate Tensile Strength and (d) Breaking or Fracture Strength of the alloys with respect to ambient and SCW condition	83
Figure 4.13: Diagram on the Collision Cascade for (a) thermal and (b) fast neutron damage in Fe-Ni-Cr alloy SS308	111
Figure 4.14: Projected Range Distribution of (a) thermal and (b) fast neutrons in Fe-Ni-Cr Alloy SS308	112

Figure 4.15: Lateral Range Distribution of (a) thermal and (b) fast neutron in the Fe-Ni-Cr Alloy SS308	112
Figure 4.16: 2D and 3D view of Ionization energy distribution of the Fe-Ni Cr alloy SS308 in both thermal and fast neutron spectrum	113
Figure 4.17: Distribution of Energy Loss as Phonons by Fe-Ni-Cr Alloy SS308 in the (a) thermal and (b) fast neutron spectrum	114
Figure 4.18: Distribution of Energy Absorbed by each elements in the SS308 in the (a) thermal and (b) fast neutron spectrum	115
Figure 4.19: Collision events of SS308 in 2D and 3D view respectively in the (a) thermal and (b) fast neutron spectrum	116
Figure 4.20: Integral sputtering yield of SS308 for (a) thermal and (b) fast neutron spectrum	117
Figure 4.21: Diagram on the Collision Cascade for (a) thermal and (b) fast neutron damage in Fe-Ni-Cr alloy SS309	117
Figure 4.22: Projected Range Distribution of (a) thermal and (b) fast neutron in the Fe-Ni-Cr Alloy SS309	118
Figure 4.23: Lateral Range Distribution of (a) thermal and (b) fast neutron in the Fe-Ni-Cr Alloy SS309	119
Figure 4.24: 2D and 3D view of Ionization energy distribution of the Fe-Ni-Cr alloy SS309 in the(a) thermal and (b)fast neutron spectrum	119
Figure 4.25: Distribution of Energy Loss as Phonons by the Fe-Ni-Cr Alloy	121



SS309 in the (a) thermal and (b) fast neutron spectrum

Figure 4.26: Distribution of Energy Absorbed by each elements in the SS309 in the (a) thermal and (b) fast neutron spectrum.	121
Figure 4.27: Collision events of SS309 in (a) 2D and 3D view respectively in the thermal and fast neutron spectrum	122
Figure 4.28: Plot of SS309 for the both the thermal and fast neutron spectrum	123
Figure 4.29: Diagram on the Collision Cascade for (a) thermal and (b) fast neutron damage in Fe-Ni-Cr alloy SS316	124
Figure 4.30: Projected Range Distribution of (a) thermal and (b) fast neutrons in the Fe-Ni-Cr alloy SS316	125
Figure 4.31: Lateral Range Distribution of (a) thermal and (b) fast neutron in the Fe-Ni-Cr alloy SS316	125
Figure 4.32: 2D and 3D view of Ionization energy distribution of the Fe-Ni-Cr alloy SS316 in the both thermal and fast neutron spectrum	126
Figure 4.33: Distribution of Energy Loss as Phonons by the Fe-Ni-Cr Alloy SS316 in the (a) thermal and (b) fast neutron spectrum	127
Figure 4.34: Distribution of Energy Absorbed by each elements in the SS316 Fe-Ni-Cr alloys in (a) thermal and (b) fast neutron spectrum.	128
Figure 4.35: Collision events of SS316 in 2D and 3D view respectively in the thermal and fast neutron spectrum	128
Figure 4.36: Integral sputtering yield of SS316 for the both the thermal and fast neutron spectrum	130

<b>LIST OF TABLES</b>		<b>Page No.</b>
Table 2.1:	SCWR reference design power and coolant conditions	7
Table 2.2:	Reference reactor pressure vessel design for SCWR	8
Table 2.3:	Material property and their Damage effects on Microstructure	29
Table 3.1:	Composition and Fe-Ni-Cr alloys selected for Damage assessment at SCW condition	45
Table 3.2:	Ion Data and Input parameters used in the SRIM-TRIM code	49
Table 3.3:	Target Data and Input parameters in SRIM-TRIM code	49
Table 3.4:	TRIM.IN setup parameters for TRIM simulation of SS304	50
Table 3.5:	Lattice Parameters used for the LAMMPS simulation	59
Table 4.1:	Summary of Equilibrium Lattice Constant and Cohesive energy from the simulation compared with theoretical value	79

## ABBREVIATIONS

LWR	Light Water Reactor
SCWR	Supercritical Water-Cooled Reactor
SRIM	Stopping and Range of Ion in Matter
TRIM	Transport of Ion in Matter
LAMMPS	Large-scale Atomic/Molecular Massively Parallel Simulator
VMD	Visual Molecular Dynamics
SCC	Stress Corrosion Cracking
IASCC	Irradiation Assisted Stress Corrosion Cracking
UTS	Ultimate Tensile Stress
PKA	Primary Knock-on-Atom
BCA	Binary Collision Approximation
MD	Molecular Dynamics
KMC	Kinetic Monte Carlo
DPA	Displacement per atom
TRIM.DAT	Transport of Ion in Matter Data
SCW	Supercritical Water Condition
.txt	Text File
NRT	Norgett Robinson Torrens
KP	Kinchin – Pease
SBE	Surface Binding Energy
SS	Stainless Steel

**LIST OF SYMBOLS**

<b>NOMENCLATURE</b>	<b>MEANING</b>
eV	Electron Volt
keV	kilo-electron volt
MeV	Mega-Electron Volt
GeV	Giga-Electron Volt
$\text{g/cm}^3$	Gram per meters cube
dpa/s	Displacement per Second
MPa	Mega-Pascal
GPa	Giga-Pascal
T	Kinetic Energy of a PKA
E	Energy
$T_{\text{dam}}$	Damage Energy
$T_{\text{max}}$	Maximum damage energy
$E_{\text{max}}, E_{\text{min}}$	Minimum and Maximum displacement energy
dEe	Differential of electron Energy
$f(T)$	Probability function
$E_D$ or $E_d$	Displacement Energy
$V_D(T)$	Average number of displaced atoms created in a cascade
$\sigma_D(E_e)$	Displacement of cross section
$\Phi(E_e)$	Electron energy flux
$E_e$	Electron Energy
$R_d$	Damage rate
$\hat{T}, \check{T}$	Maximum and Minimum transferred energy
$\hat{E}, \check{E}$	Maximum and Minimum threshold energy
$E_{\text{latt}}, E_{\text{surf}}$	Lattice Binding Energy , Surface Binding Energy
$\epsilon, \sigma$	Strain , Stress

## CHAPTER ONE: INTRODUCTION

### 1.1. BACKGROUND

Supercritical Water-Cooled Reactor (SCWR) is a Light Water Reactor (LWR) operating at higher pressure and temperatures with a direct, once-through cycle [1-3]. The coolant of the reactor remains single-phase throughout the system since it operates above the critical pressure and temperature (374 °C, 22.5 MPa) and hence eliminates coolant boiling [4, 5]. The neutron radiation is anticipated to be 10–30 dpa (displacement per atom) and 100 – 150 dpa for the thermal and fast spectrum at energy of 365 MeV and 1.5 GeV respectively [1, 6].

Research is keenly needed in the design of the SCWR since no nuclear reactors that uses supercritical water as its coolant have so far been built, though it is promising, but however demonstration or experimental reactors of very closely related concepts have already been built for the other Generation IV concepts [7, 8].

Development of fission reactor critically depends on advances made in nuclear fuels and also in their systems and structural materials which may have to withstand the severe environmental conditions (such as high temperatures, neutron irradiation and strong corrosive environments) in combination with complex loading and operational cycles and longer design life requirements [9].

Searching for new materials and tailoring them to the desired system properties and operational requirements is therefore central to the reactor developments to establish the optimal materials operational parameters range for SCWR for the selection of structural

and cladding materials that will maintain reliable operation of a SCWR power plant for its design life of 60 years [10, 11].

Some candidate materials such as ferritic-martensitic steels and low-swelling austenitic steels have been identified [12]. These materials are not proven [7, 13] and hence global on-going research to characterize their physical, nuclear and mechanical properties [14].

## **1.2. RESEARCH PROBLEM STATEMENT**

To examine the irradiation resistance and mechanical integrity of Fe-Ni-Cr based alloys as candidate materials for Supercritical Water (SCW) condition pressure vessel and in-core structural components through Binary Collision Approximation and Molecular Dynamics simulations respectively on stainless steels (SS) categories 304, 308, 309 and 316.

## **1.3. RESEARCH JUSTIFICATION**

Neutron irradiation of in-core materials creates point defects [15] which results in significant modifications in physical dimensions, strength and hardness, thermal and electrical conductivity, resistance to corrosion, etc. A nuclear reactor operates within very stringent requirement throughout the working life of the reactor and so structural materials must maintain their mechanical properties and dimensional stability.

Hence incremental changes in materials properties during steady state reactor operations must stay within specifications and all materials must be able to perform throughout the reactor's life as required under all postulated accident conditions.

Reactor safety, material degradation and failure are areas of critical importance as high neutron flux could lead to high irradiation dose [6, 16, 17]. There is the need for research to investigate the Fe-Cr-Ni alloy as possible candidate for SCWR in-core structural materials, especially the austenitic steel which are durable and have good mechanical strength.

#### **1.4. RESEARCH GOAL**

The goal is to examine neutron irradiation damage and mechanical degradation of the Fe-Cr-Ni alloys (SS304, SS308, SS309 and SS316) by high neutron dose loading of 10 – 30 dpa and 100 – 150 dpa respectively. Both thermal and fast neutron bombardment in high pressure and temperature conditions as would pertain in SCW conditions are of interest and hence the above materials were is to be examined using Binary Collision Approximation and Molecular Dynamics simulations SRIM-TRIM, LAMMPS code respectively along with VMD and MATLAB.

#### **1.5. RESEARCH OBJECTIVES**

The main objectives of the research were to:

- Simulate thermal and fast neutron irradiation damage of Fe-Cr-Ni alloys at 30 dpa and 150 dpa to determine the Depth of penetration, Ionization energy, Energy to Phonons, Energy to recoils, and Vacancy production for current SCWR design.
- Evaluate the mechanical behavior and dimensional stability of the Fe-Ni-Cr as a function of high pressure and temperature using LAMMPS and VMD codes

- Compare suitability of the four Fe-Ni-Cr alloys as in-core structural materials and for pressure vessel design and make selection by TRIM code and mechanical integrity assessment by the LAMMPS and VMD code.

## **1.6. SCOPE OF THE RESEARCH**

The thesis is divided into five Chapters.

Chapter One provide the background to the research work, research problem statement, relevance and justification of the research, the research goal, objectives and the scope of the research work.

Chapter Two deals with the review of relevant Literature on materials challenges for SCWR, irradiation damage mechanisms and induced mechanical deterioration, current materials selection for SCWR vessel, mechanical integrity evaluation and Computer Simulation code of radiation damage and mechanical degradation.

Chapter Three presents the Research Methodologies employed relating to the irradiation damage assessment of the materials using the SRIM-TRIM code and the mechanical damage evaluation using LAMMPS and VMD codes

In Chapter Four, the Results obtained, interpretation of the data and discussion of the research findings are presented.

Chapter Five provides the Conclusions, Recommendations and Suggestions for future research work. Also the references cited are listed and Appendices are also presented.



## CHAPTER TWO: LITERATURE REVIEW

### 2.1 SUPERCRITICAL WATER CONDITION

Supercritical Water-Cooled Reactors are high temperature, high-pressure, light water reactors that operate above the thermodynamic critical point of water (374 °C, 22.1 MPa).

The reactor core may have a thermal or a fast-neutron spectrum, depending on the core design [15]. Figure 2.1 shows two different SWC regimes, the US and CANDU design.

The US design which operates at temperature range of 280°C to 500°C and at a constant pressure of 25 MPa was chosen for the research work [6].

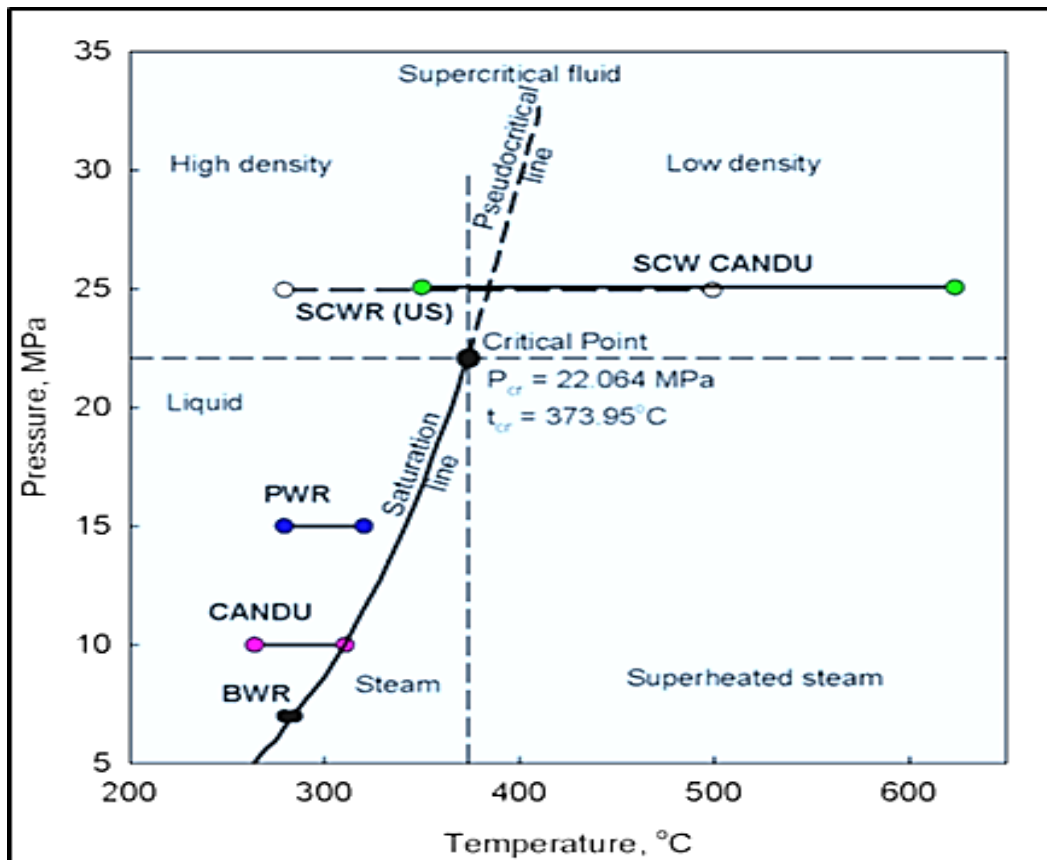


Fig 2.1: Phase Diagram of SCW condition [18]

## 2.2 DESIGN PARAMETERS FOR STRUCTURAL AND PRESSURE VESSEL OF SCWR

The concept of SCWR as shown in Fig. 2.2, would either be based on current pressure-vessel or on pressure-tube reactors, and hence may use light water or heavy water as a moderator. SCWR is being researched into in countries like Canada, China, EU, Japan, Korea, Russia and US and out of all these countries, its only Canada that has a reactor based on pressure-tube concept [3, 8]. The SCWR coolant will experience a higher enthalpy rise in the core which will then reduce the core mass flow for a given thermal power compared to the current LWR reactors. For both pressure-vessel and pressure-tube designs, a once-through steam cycle has been envisaged, omitting any coolant recirculation inside the reactor [18].

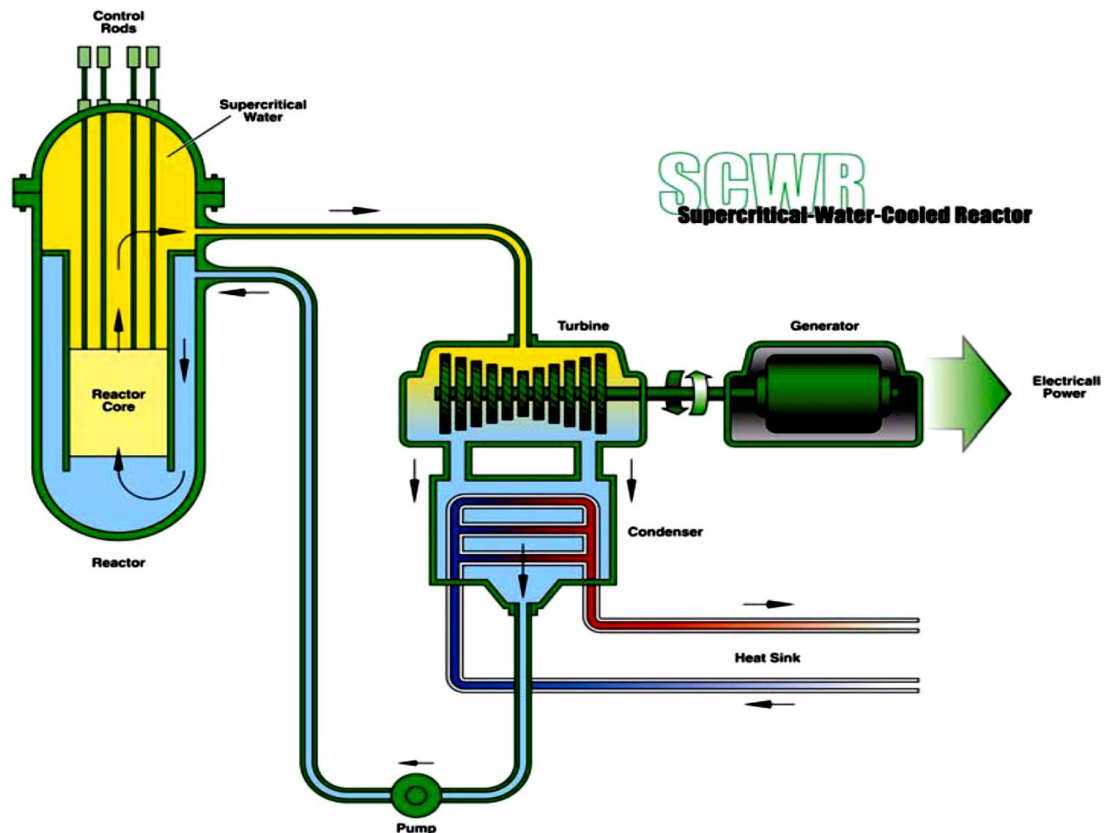


Fig 2.2: Conceptual Design of SCWR [19]

The superheated steam will be supplied directly to the high pressure steam turbine and the feed water from the steam cycle will be supplied back to the core. SCWR concepts combine the design and operation experience gained from hundreds of water-cooled reactors and the experience from hundreds of fossil-fired power plants operated with supercritical water. In contrast to some of the other Generation IV nuclear systems, the SCWR can be developed step-by-step from current water-cooled reactors [20, 21].

The design parameters of the SCWR considered for the research are given in Table 2.1 and 2.2

Table 2.1: SCWR reference design power and coolant conditions [6, 22-25].

<b>Parameters</b>	<b>Value</b>
<b>Thermal power</b>	3,575 MW <sub>t</sub>
<b>Net electric power</b>	1,600 MW <sub>e</sub>
<b>Net thermal efficiency</b>	44.8 %
<b>Operating pressure</b>	25 MPa
<b>Reactor inlet coolant temperature</b>	280 °C
<b>Reactor outlet temperature</b>	500 °C
<b>Plant lifetime</b>	60 years

Table 2.2: Reference reactor pressure vessel design for SCWR [6, 22-25].

Parameters	Value
Type	PWR with CRD
Height	12.40 m
Operating/design pressure	22.0/27.5 MPa
Operating/design temperature	280/371 °C
Number of cold/hot nozzles	2/2
Inside diameter of shell	5.322 m
Thickness of shell	0.46 m
Inside diameter of head	5.352 m
Thickness of head	0.305 m
Peak fluence (> 1 MeV)	$< 5 \times 10^{19} \text{ n/cm}^2$
Core Structural materials considered	SS304, SS308, SS309, SS316

\*PWR-Pressurized Water Reactor, CRD-Control Rod Driven

## 2.3 MATERIAL CHALLENGES WITH SCWR

### 2.3.1. Material Needs of SCWR

Some of the material challenges associated with the SCWR are

- Higher pressure combined with higher temperature and also a temperature rise across the core result in increased mechanical and thermal stresses on the vessel materials [5, 14].
- Extensive material development (i.e. high irradiation and mechanical resistant ones) and research on supercritical water chemistry under radiation are needed [8, 24, 26].

The identification of appropriate materials for the pressure vessel and core structure, and understanding of supercritical water (SCW) chemistry are two of the main challenges for the development of SCWR [27, 28]. Zirconium-based alloys, may not be a viable material without some sort of thermal and/or corrosion-resistant barrier [29]. Although there is considerable experience with fast reactors and supercritical-water-cooled fossil fueled plants (FFPs), little or no data on the in-flux behavior of these materials at the temperature of 500 °C and pressure of 25 MPa exists [25]. The understanding of the primary radiation damage in Fe-based alloys is of interest for the use of advanced steels in future fusion and fission reactors [30].

### **2.3.2. Candidate In-core Structural Materials of SCWR**

Based on experiences from LWRs, fast reactors, and SWC Fossil Fire Plants (FFPs), Fe-Ni-Cr austenitic stainless steels (e.g., 304, 316) with higher Cr contents, corrosion-resistant ferritics (e.g., HT-9), and advanced ferritic/martensitic (e.g., 9 to 14% Cr), are being considered as materials for core internal components [8]. Precipitation-hardened Ni-based alloys (e.g., 718, 625) have also received attention for applications where dose rates are on the lower end of the projected range.

In structures where temperatures will be significantly above 300 °C, or irradiation doses above 30 dpa, candidate structural materials will be primary ferritic or martensitic steels and low swelling austenitic stainless steels. Fe-Ni-Cr alloys with acceptable mechanical behavior and dimensional stability are also possible candidates, though, there is currently insufficient technical knowledge and data for predicting Fe-Ni-Cr alloy behavior under supercritical water condition [9].

### **2.3.3. Structural Integrity of Irradiated materials**

Irradiation-induced changes to the cladding and structural materials especially the pressure vessel due to swelling, helium-bubble formation and growth, and microstructure precipitation are being investigated to overcome any compromise to the irradiation resistant and mechanical properties of the components for the design life of the reactor [31-34]. Also He segregation will be an important consideration because of the greater relative production of He/dpa (displacement per atom) at thermal neutron energies. For temperatures between 280 °C and 350 °C, the irradiation damage behavior for 304, 308, 309 and 316 Fe-Ni-Cr Alloys has been studied [35] since such materials have been used in the existing Light Water Reactors (LWR). The viability of a SCWR will also depend on mechanical behavior of both in-core and out-core materials.

## **2.4. IRRADIATION DAMAGE ASSESSMENT**

### **2.4.1. Irradiation Damage Events and Mechanisms**

Effects of radiation on solids have been studied extensively. Of much more interest to the present research, however, are the high energy radiation fields in reactors. That the success of reactor technology would depend critically on the choice of high-temperature material with satisfactory neutronic properties was pointed out by Fermi in 1946 [37].

The radiation damage event occurs by transfer of energy from a high energy incident particle to the solid and the resulting distribution of target atoms in the lattice after completion of the event. The displacement of the host lattice atom in the Coulomb collision

and the consequent production of point defects marks the final stage of the damage sequence. The radiation damage event processes that occur are [38],

- Transfer of kinetic energy to the lattice atom leading to a Primary-Knocked-on-Atom (PKA);
- Displacement of a primary-knocked-on atom (PKA) from its lattice site;
- The passage of the displaced atom through the lattice and the accompanying creation of additional knock-on atoms;
- Production of a displacement cascade; and
- Termination of the PKA as creating interstitials, vacancies, and Frankel pairs.

When energy transferred to a lattice atom is larger than the energy binding the atom in the lattice site, the lattice atom is displaced from its original position. The displaced atom might carry high enough kinetic energy to create a series of lattice displacements before finally coming to rest. The displaced atom eventually appears in the lattice as an interstitial atom leading to vacancies generations. Collection of point defects created by a single primary knock-on atom is known as a displacement cascade [41-43].

Neutron irradiation mechanism begins with the unstable radionuclide atom given off gamma ( $\gamma$ ) rays and fissile particles such as alpha ( $\alpha$ ), beta ( $\beta$ ), neutrons, ions, electrons, and other fission products to materials [24]. Figure 2.3 shows that exposure of matter to highly energetic radiations or particles results in changes in the physical, chemical, biological or mechanical properties, which start from the microscopic state to the macroscopic or observable state. In a nuclear reactor, thermal and fast neutrons are released depending on the energy spectrum generated, in addition to alpha particles, beta particles, gamma rays and other fission products.

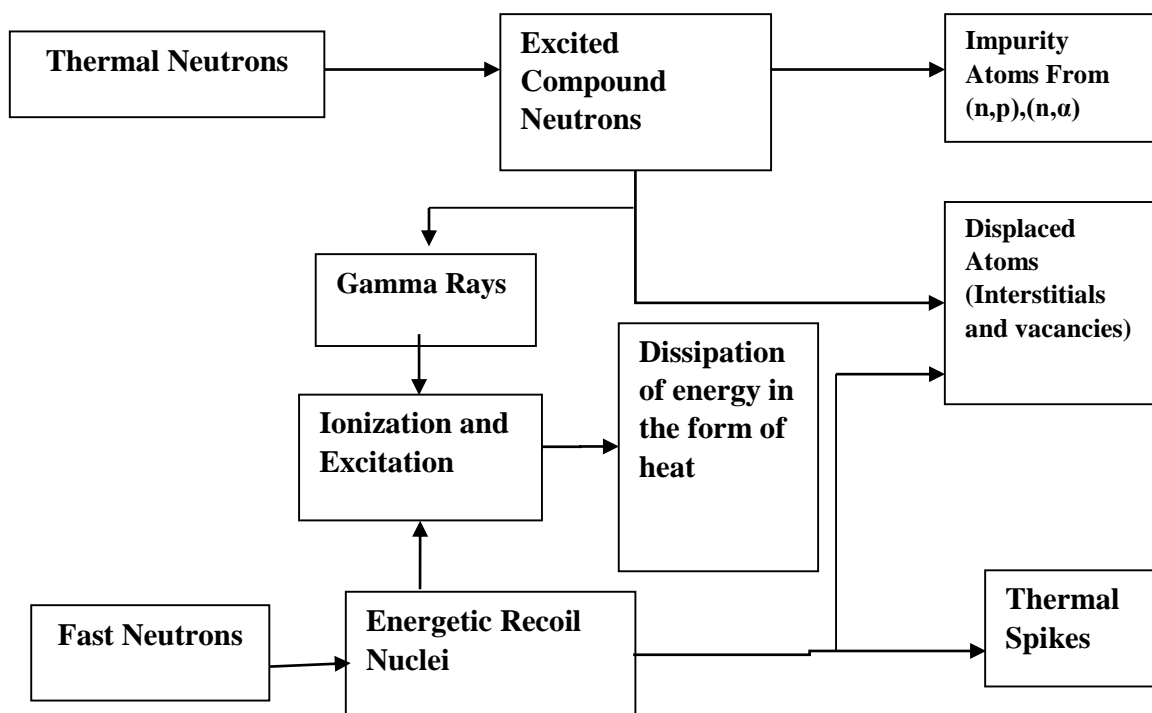


Fig. 2.3: Mechanisms of irradiation damage in the nuclear reactor system by thermal and fast neutrons[12]

Gamma, beta, and alpha are classified as ionizing radiation because they interact only with the electrons surrounding the nuclei of the material which normally destroys the atomic bonding of the material and thereby causing damage [28]. But the damage in metals is sometimes not significant since metals have a relative immunity to ionization radiation unlike nonmetallic substances, such as water and other organic compounds [44].

Thermal neutrons are absorbed or captured as upon interaction with the nuclei of non-fuel material, thereby leaving these nuclei in excitation or high energy state. The excess energy (being the gamma radiation and the kinetic energy of the recoiled nuclei) is released by emitting high energy gamma rays with the result that these emitting nuclei recoil [29]. If the kinetic energy exceeds a certain minimum value called the displacement energy, which is ranges from about 25 to 30 eV for most metals, then the recoiling (“knock-on”) atom is displaced from its equilibrium position in the crystal lattice. The released high energy



gamma radiation however undergoes ionization and excitation and is converted into kinetic energy of electrons or positrons which dissipates heat over a short distance. The excited compound nuclei could also be transmuted to other nuclei which may be radioactive hence leads to impurities deposition in a form of alpha particles (helium) and protons (hydrogen) which are neutralized in the material of passage [45, 46].

Fast neutrons, due to their high energy undergo elastic collisions with the atomic nucleus of the material resulting in production of alpha and beta particles and also transfer of their kinetic energy to the recoil nucleus. The highly energetic recoil nucleus undergoing ionization and excitation dissipates electron energy in a form of heat. Also due to the high kinetic energy of the recoil nucleus, the recoiling atom (also known as primary knock-on atom) could be displaced from its equilibrium position in the crystal lattice [46, 47]. Since the PKA now possesses substantial kinetic energy, it becomes energetic particle in its own right and it's capable of creating additional lattice displacement which continues until the displaced atom has insufficient energy to eject another atom. These subsequent generations of displaced lattice atoms are known as secondary or higher order knock-ons. Finally when the fast neutron is slowed down to the point where it can no longer cause atomic displacement, much of its remaining energy will be dissipated within a short distance as vibrational (heat) energy of the target atom. A thermal spike, in which high local temperatures are attained, may then be formed [12, 48].

#### **2.4.2. Rate of Production of Displacements ( $\dot{N}_d(E)$ )**

The rate of production of displacement,  $\dot{N}_d(E)$  is the number of vacancy and interstitial pairs (Frankel pairs) produced per second by an incident particle of energy  $E$  per second

of neutron radiation and is given as the product of effective/macroscopic displacement cross section ( $N\sigma_d(E)$ ) and neutron flux  $\Phi(E)$  [12, 15, 45, and 49]:

$$\dot{N}_d(E) = N\sigma_d(E)\Phi(E) \quad (2.1)$$

where  $\sigma_d(E)$  is the microscopic displacement cross section for neutron radiation (i.e. an incident particle) of energy  $E$  per second,  $\Phi(E)$  is the neutron flux of energy  $E$  and  $N$  is the atom density of the target material in which the displacements occur.

The microscopic displacement cross section for neutron with energy  $E$  per second is defined by [12, 46, 47- 48]:

$$\sigma_d(E) = \int_{2E_d}^{T_m(E)} v(T) \sigma(E, T) dT \quad (2.2)$$

where  $v(T)$ ,  $\sigma(E, T)$  and  $T_m(E)$  are related by the equations:

$$v(T) \approx CT \approx \frac{T}{2E_d} \quad (2.3)$$

$$\sigma(E, T) = \frac{\sigma_s(E)}{T_m(E)} \quad (2.4)$$

$$T_m(E) = (1 - \alpha)E = \frac{4A}{(A+1)^2} E \approx \frac{4}{A} E \quad (2.5)$$

where,  $\alpha$  is a property of the scattering nucleus related to its mass and is defined by  $\alpha = \left(\frac{A-1}{A+1}\right)^2$ , and equation (2.5) is the maximum energy loss in a collision that can be transferred to a knock-on atom by a neutron,  $v(T)$  is the mean number of displacements in a cascade originating from the primary knock-on,  $T$  is the amount of energy transferred to the atom

ejected from the lattice,  $C$  is the knock-on energy at which atom displacement is terminated,  $\sigma(E, T)$  is the differential cross section (per unit energy) for the transfer of kinetic energy  $T$  to a knock-on atomic in an elastic collision with energy of  $E$ ,  $\sigma_s(E)$  is the elastic scattering cross section for the target material of neutron of energy  $E$ ,  $T_m(E)$  is the maximum energy that can be transferred to a knock-on atom by a radiation particle of energy  $E$  and  $A$  is the mass number of the target nucleus of the reactor core material. Substituting equations (2.3), (2.4) and (2.5) into (2.2) resulted in

$$\sigma_d(E) = \int_{2E_d}^{T_m(E)} \frac{T}{2E_d} \cdot \frac{\sigma_s(E)}{T_m(E)} dT \quad (2.6)$$

$$\sigma_d(E) = \frac{\sigma_s(E)}{2E_d \cdot T_m(E)} \int_{2E_d}^{T_m(E)} T dT \quad (2.7)$$

Integrating equation (2.7) from  $2E_d$  to  $T_m(E)$  leads to

$$\sigma_d(E) \approx \sigma_s(E) \cdot \frac{E}{AE_d} \quad (2.8)$$

Hence, substituting equation (2.8) into equation (2.1) became

$$\dot{N}_d(E) \approx N \Phi(E) \cdot \sigma_s(E) \cdot \frac{E}{AE_d} \quad (2.9)$$

Equation (2.9) indicates that rate of production of atomic displacement defects produced in a nuclear material exposed to a constant neutron flux with time which has a relation with atomic density of the target material, constant neutron flux, and total elastic scattering cross section of the target material, neutron energy ( $E$ ), atomic number of the target material and threshold displacement energy [50].

The fluence is the product of the constant neutron flux and the exposure time  $\Phi(E) \cdot t$ .

Multiplying equation (2.9) by time resulted in the total number of displaced atom as:

$$[\dot{N}_d(E) \cdot t] \approx N [\Phi(E) \cdot t] \cdot \frac{\sigma_s(E)}{AE_d} E \quad (2.10)$$

The number of displacements per atom (dpa) is given by [49,51]

$$\therefore \text{dpa} = \left[ \frac{\dot{N}_d(E) \cdot t}{N} \right] \approx [\Phi(E) \cdot t] \cdot \frac{\sigma_s(E)}{AE_d} E \quad (2.11)$$

where  $[\Phi(E) \cdot t]$  is the fluence of neutron radiation measured in neutrons/cm<sup>2</sup>.

### 2.4.3. Kinchin-Pease Model of Radiation Damage

The Kinchin – Pease Model assumes that between a specified threshold energy and an upper energy cut-off, there is a linear relationship between the number of Frenkel pair produced and the PKA energy. Below the threshold, no new displacements would be produced. Above the high energy cut-off, it was assumed that the additional energy was dissipated in electronic excitation and Ionization [15, 31, and 52].

#### 2.4.3.1 Displacement probability:

The Displacement probability is defined as the probability that a struck atom is displaced upon receipt of energy  $T$ . This is due to exchange in energy during a Coulomb collision between an electron and a lattice nucleus of the target material. The simplest model for the displacement probability is a step function, with a sharp displacement energy value  $E_d$ , shown in Figure 2.4 (a) below and expressed by [15, 46, and 48]:

$$P_d(T) = \begin{cases} 0 & \text{for } T < E_d \\ 1 & \text{for } T \geq E_d \end{cases} \quad (2.12)$$

This model is constant for all collisions because it neglects the thermal atomic vibration of the lattice, which introduces a width of the order of  $kT$  in the displacement probability. A more accurate model is shown by a function in which the energy threshold is not sharp, but it goes from 0 to 1 with a smooth curve, as it is shown in Figure 2.2b. The corresponding mathematical formulation [15, 48] and where  $f(T)$  a function varying smoothly between [0, 1]:

$$P_d(T) = \begin{cases} 0 & \text{for } T < E_{\min} \\ f(T) & \text{for } E_{\min} < T < E_{\max} \\ 1 & \text{for } T \geq E_{\max} \end{cases} \quad (2.13)$$

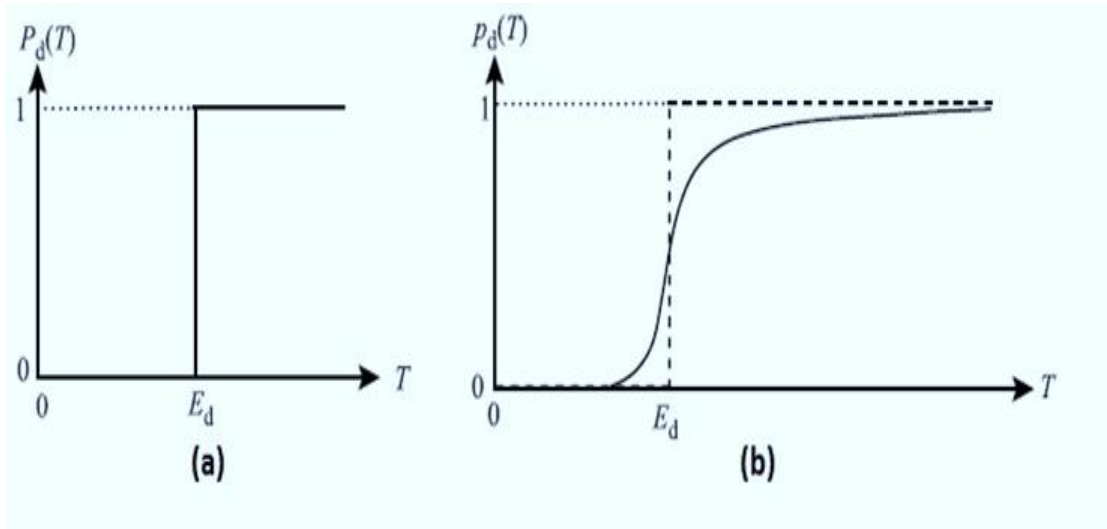


Fig. 2.4: The displacement probability  $P_d(T)$  as function of the transferred kinetic energy, assuming (a) a sharp or (b) a smoothly varying displacement threshold [31, 48]

### 2.4.3.2 Displacement Energy

A lattice atom must receive a minimum amount of energy in the collision in order to be displaced. The struck lattice atom of energy  $T$ , is referred to as a primary knock-on atom (PKA), displacement energy  $E_d$ , threshold displacement energy or displacement threshold energy [53]. The magnitude of  $E_d$  is dependent upon the crystallographic structure of the lattice, the direction of the incident PKA, the thermal energy of the lattice atom, etc. If the energy transferred,  $T$  is less than  $E_d$ , the struck atom will vibrate about its equilibrium position but will not be displaced. These vibrations diffuse through the lattice and transform the absorbed kinetic energy into heat. On the contrary, if  $T > E_d$  the PKA starts travelling into the solid structure with kinetic energy  $T - E_d$  [32]. Maximum kinetic energy transferred in an elastic collision of particle is given by:

$$T_{\text{Max}} = E \frac{4Mm}{(m + M)^2} \quad (2.14)$$

Where  $E$  is kinetic energy,  $M$  is mass of the incident particle and  $m$  is mass of the material atom (target atom)

### 2.4.3.3 Radiation Damage

The theoretical basis of calculating the total number of displaced atoms resulting from a single PKA of energy  $E$  is now considered. The number of displaced atoms is denoted by  $v(E)$ . Simplest theory of displacement cascade is that of Kinchin-Pease [31, 32, and 52] based on the assumptions that:

1. The cascade is created by a sequence of two-body elastic collisions between atoms

2. The displacement probability is 1 for  $T > E_d$  as given by equation (2.12)
3. When an atom with initial energy  $T$  emerges from a collision with energy  $T'$  and generates a new recoil with energy  $\epsilon$ , it is assumed that no energy passes to the lattice and  $T = T' + \epsilon$
4. Energy loss by electron stopping is treated by the cut-off energy  $E_c \sim 10^3 \text{ eV}$ . If the PKA energy is greater than  $E_c$  no additional displacements occur until electronic energy losses reduce the PKA energy to  $E_c$ . For all energies less than  $E_c$  electronic stopping is ignored and only atomic collisions take place
5. The energy transfer cross section is given by the hard sphere model
6. The arrangement of the atoms in the solid is random effects due to the crystal structure are neglected

The cascade is initiated by a single PKA of energy  $T$ , which eventually produces  $v(T)$  displaced atoms. If PKA of energy  $E$  transfer energy  $T$  to the struck atom and leaves the collision with energy  $(\epsilon - E_d)$ , the PKA has residual energy  $T - \epsilon$ , so that:

$$v(T) = v(T - \epsilon) + v(\epsilon - E_d) \quad (2.15)$$

where  $E_d$  is the energy consumed in the reaction. If  $\epsilon \gg E_d$  according to assumption 3, then equation (2.15) simplifies to:

$$v(T) = v(T - \epsilon) + v(\epsilon) \quad (2.16)$$

Equation (2.16) is not sufficient to determine  $v(T)$  because the energy transfer  $\epsilon$  may lie anywhere between 0 and  $T$ . However, if we know the probability of transferring energy in the range  $(\epsilon, d\epsilon)$  in a collision then multiplying equation (2.16) by this probability and

integrate over all allowable values of  $\epsilon$  will yield the average number of displacements,  $\hat{v}(T)$ .

By Kinchin and Pease model of the displacement, the energy transfer cross section  $\sigma$ , by hard-sphere assumption 5 is [48],

$$\sigma(T, \epsilon) = \frac{\sigma(T)}{\gamma T} = \frac{\sigma(T)}{T} \quad (\text{for like atoms, } \gamma = 1) \quad (2.17)$$

The probability of a PKA energy  $T$  transfers energy in range  $(\epsilon, d\epsilon)$  to the struck atom is [15, 48]:

$$\hat{p} = \frac{\sigma(T, \epsilon)d\epsilon}{\sigma(T)} = \frac{d\epsilon}{T} \quad (2.18)$$

Hence, the average number of displacement, given by

$$\hat{v}(T) = \int_0^T v(T) \times \hat{p} = \int_0^T \frac{v(T)}{T} d\epsilon \quad (2.19)$$

$$\hat{v}(T) = \frac{1}{T} \int_0^T [v(T - \epsilon) + v(\epsilon)] d\epsilon \quad (2.20)$$

$$\hat{v}(T) = \frac{1}{T} \left[ \int_0^T v(T - \epsilon) d\epsilon + \int_0^T v(\epsilon) d\epsilon \right] \quad (2.21)$$

Setting  $\epsilon \rightarrow \epsilon' = T - \epsilon$ , then  $dT - d\epsilon = d\epsilon'$  in the first integral and equation (2.21) became

$$\hat{v}(T) = \frac{1}{T} \int_0^T v(\epsilon') d\epsilon' + \frac{1}{T} \int_0^T v(\epsilon) d\epsilon \quad (2.22)$$

$$\hat{v}(T) = \frac{2}{T} \int_0^T v(\epsilon) d\epsilon \quad \text{since } \epsilon \rightarrow \epsilon' \quad (2.23)$$

By examining the following relations

$$\hat{v}(T) = 0 \quad \text{for } 0 < T < E_d \quad (2.24)$$

$$\hat{v}(T) = 1 \quad \text{for } 0 < T < 2E_d \quad (2.25)$$

For if  $T < E_d$  there will be no displacements; if  $T > E_d$  and  $T < 2E_d$ , two outcomes are possible. The first is that, the struck atom is displaced from its lattice site and the PKA now



leaves with energy less than  $E_d$ , falls into its place. However, if the original PKA does not transfer  $E_d$ , the struck atom remains in place and no displacement occurs. In either case, only one displacement in total is possible from a PKA with energy between  $E_d$  and  $2E_d$ . By splitting and integrating equation (2.23) with equations (2.24) and (2.25) as limits and evaluate:

$$\hat{v}(T) = \frac{2}{T} \left[ \int_0^{E_d} (0) d\varepsilon + \int_{E_d}^{2E_d} (1) d\varepsilon + \int_{2E_d}^T v(\varepsilon) d\varepsilon \right] \quad (2.26)$$

then

$$\hat{v}(T) = \frac{2E_d}{T} + \frac{2}{T} \int_{2E_d}^T v(\varepsilon) d\varepsilon \quad (2.27)$$

$$\hat{v}(T) = \frac{2}{T} \left[ 0 + E_d + \int_{2E_d}^T v(\varepsilon) d\varepsilon \right] \quad (2.28)$$

Multipling Equation (2.28) by T and then differentiating with respect to T

$$\hat{v}(T) \times T = 2E_d + 2 \int_{2E_d}^T v(\varepsilon) d\varepsilon \quad (2.29)$$

and

$$\frac{d}{dT} (\hat{v}(T) \times T) = 2 \frac{d}{dT} \int_{2E_d}^T v(\varepsilon) d\varepsilon \quad (2.30)$$

Since  $T = \varepsilon + \varepsilon' \Rightarrow T \approx \varepsilon$  and  $dT = d\varepsilon$  for  $\varepsilon' \ll \varepsilon$

$$\frac{d}{dT} (\hat{v}(T) \times T) = 2 \frac{d}{dT} \int_{2E_d}^T v(T) dT \quad (2.31)$$

and

$$\hat{v}(T) + T \frac{d\hat{v}(T)}{dT} = 2 v(T) \quad (2.32)$$

implying:

$$T \frac{dv(T)}{dT(T)} = v(T) \quad (2.33)$$

or:

$$\frac{dv(T)}{v(T)} = \frac{dT}{T} \quad (2.34)$$

with solution:

$$\ln v(T) = \ln T + \ln C = \ln(CT) \quad (2.35)$$

$$\hat{v}(T) = CT \quad (2.36)$$

where value of C, obtained by putting equation (2.36) into (2.27)

$$CT = \frac{2E_d}{T} + \frac{2}{T} \int_{2E_d}^T (CT) dT = \frac{2E_d}{T} + \frac{2C}{T} \left[ \frac{T^2}{2} \right]_{2E_d}^T \quad (2.37)$$

and:

$$CT = \frac{2E_d}{T} + \frac{2C}{T} \left[ \frac{T^2}{2} - \frac{4E_d^2}{2} \right] = \frac{2E_d}{T} + CT - \frac{4CE_d^2}{T} \quad (2.38)$$

or:

$$\frac{4CE_d^2}{T} = \frac{2E_d}{T} \quad (2.39)$$

Therefore:

$$C = \frac{1}{2E_d} \quad (2.40)$$

and therefore substituting (2.40) into (2.36) gives:

$$\hat{v}(T) = \frac{T}{2E_d} \quad \text{for} \quad 2E_d < T < E_c \quad (2.41)$$

By assumption 4, the upper limit is set by  $E_c$ . When a PKA is born with  $T > E_c$ , the number of displacements is  $\hat{v}(T) = E_c/2E_d$  for  $T > E_c$ . Hence the full Kinchin – Pease (K – P) model equations are

$$\hat{v}(T) = \begin{cases} 0; & \text{for } T < E_d \\ 1; & \text{for } E_d < T < 2E_d \\ \frac{T}{2E_d}; & \text{for } 2E_d < T < E_c \\ \frac{E_c}{2E_d}; & \text{for } T > E_c \end{cases} \quad (2.42)$$

The graphical description of the average number of displacements,  $v_1(T)$  of equation (2.30) is shown in Fig. 2.5.

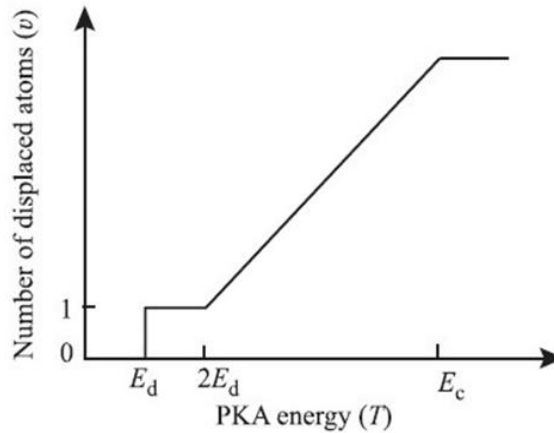


Fig. 2.5: Average number of displacements  $\hat{v}(T)$  produced by a PKA, as a function of the recoil energy  $T$  according to the model of Kinchin – Pease [15, 48 ].

The energy ranges are explainable as follows. First of all, there can be no displacement if the recoil energy  $T$  is lower than  $E_d$ , because of the sharp displacement threshold assumption 5. Secondly, when  $E_d < T < 2E_d$ , displacement occurs and a PKA starts travelling through the lattice of the vessel, but with kinetic energy  $(T - E_d)$ , since  $E_d$  was necessary to overwhelm the lattice potential. Therefore, in this energy range the PKA does not have enough energy to produce further displacements. Above  $2E_d$  the behavior is linear, until the electron energy loss limit  $E_c$  is reached.

#### 2.4.4. Norgett-Robinson-Torrens Radiation Damage Model

The Norgett-Robinson-Torrens (NRT) model, was developed as secondary displacement model, (also known as modified K-PM) for computing the number of displacements per atom (dpa) for a PKA with a given energy. The NRT model was broadly adopted by the International Radiation Effects Community and continues to be the internationally-recognized standard method for computing atomic displacement rate [31, 32, and 48].

The NRT displacement model gives the total number of stable Frenkel pair produced by a PKA with kinetic energy  $E$  as [34, 41]:

$$V_{\text{NRT}} = \begin{cases} \frac{k(T - E_e)}{2E_d} = \frac{kT_{\text{dam}}}{2E_d}, & T_{\text{dam}} > 2E_d \\ 1, & E_d < T_{\text{dam}} < 2E_d \\ 0, & 0 < T_{\text{dam}} < E_d \end{cases} \quad (2.43)$$

where  $V_{\text{NRT}}$ ,  $k$ ,  $T$ ,  $E_e$ ,  $E_d$ , and  $T_{\text{dam}}$  are the number of displaced atoms produced by PKA, damage efficiency, recoil energy of a PKA, total energy lost by electron excitation, threshold displacement energy and damage energy available for elastic collisions respectively. The damage efficiency  $k$  holds a value of 0.8 and accounts for the fact that not all collisions are for ideal hard spheres [48, 49, and 54].

If  $T_{\text{dam}} < E_d$  there will be no damage energy to cause displacements and also if  $T_{\text{dam}} > E_d$  and  $T_{\text{dam}} < 2E_d$ , two effects are possible as shown in equation (2.43).

#### 2.4.5. Radiation Damage Defects

The radiation damage event takes a very short time of the order of  $10^{-11}$  s, and produces a collection of point defects (i.e. vacancies and interstitials) and the formation of defect clusters. Figure 2.6 shows defects in the lattice structure of materials that can change the material properties and can affect the performance [55, 56].

The Radiation Damage Event may be followed by a cluster of phenomena which can be classified as radiation damage effects:

1. migration of point defects and clusters, according to their mobility inside the crystal structure, with possible growth of the cluster or recombination of a vacancy-interstitial couple
2. modification of the material composition due to a varied mobility of impurities contained in alloys

3. possible degradation of structural properties and hindering of the component purposes.

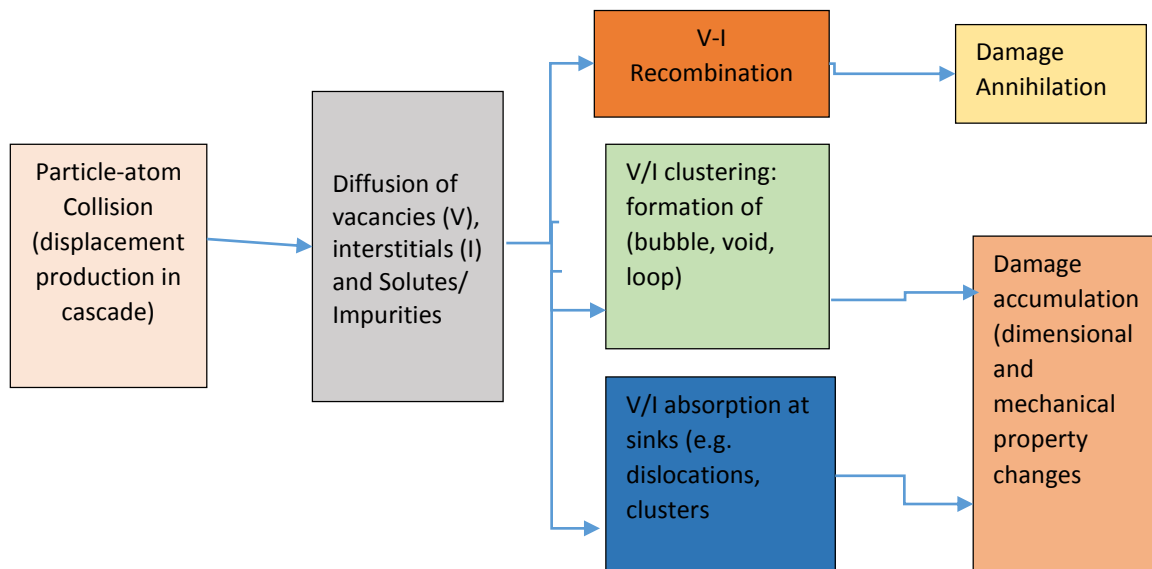


Fig 2.6: Radiation damage defects creation processes [55]

Irradiation as shown in Fig. 2.6 produces interstitial and vacancy point defects in the lattice shown in Fig. 2.7 which often leads to changes in properties of the material. Interstitial and vacancy are point defects which often have high mobility and readily diffuse through the crystal lattice, and the freely-migrating point defects combine to form higher-order point defect complexes. This point defect condensation process progresses continuously into a nucleation and growth process of extended defect clusters. Interstitial clusters become interstitial loops. Vacancy clusters become either vacancy loops or voids. This microstructural evolution leads to property changes such as embrittlement and macroscopic swelling and hence effects on the performance of the nuclear materials. Also, changes in properties are proportional to radiation flux, particle energy, irradiation time and temperature.

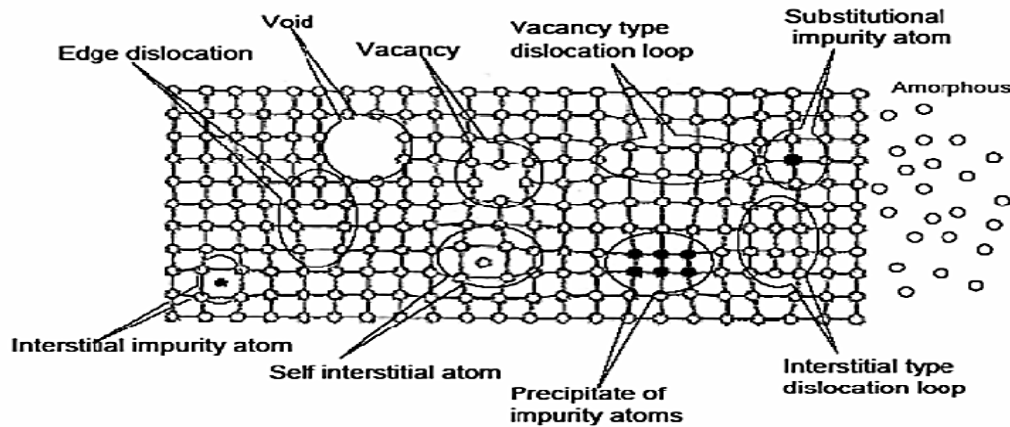


Fig. 2.7: Defects in the lattice structure of materials [57]

## 2.5. MECHANICAL PROPERTIES OF STRUCTURAL MATERIALS

A nuclear reactor system must include a containing pressure vessel for the core infrastructure, mechanical support for the core components, piping for the coolant, and cladding for the fuel elements. The requirements for these materials to serve the different purposes will vary with the reactor type, but some general characteristics may be noted. Mechanical properties, such as tensile strength, yield strength, ductility, impact strength, fatigue and creep, must be adequate for the operating conditions [48].

The choice of material for fast reactors is less dependent on neutron absorption cross sections than for thermal reactors. However, the four elements with low thermal-neutron absorption cross sections (less than 0.24 b) and reasonably high, melting points; are aluminum, beryllium, magnesium, and zirconium. Of these, aluminum, magnesium, and zirconium have been utilized in fuel-element cladding, while beryllium has been used for reflectors. Although the major constituents of stainless steels, namely, iron, chromium, and nickel, have relatively high thermal-neutron absorption cross section of 2.6, 3.1 and 4.4 b, respectively, these steels also have good mechanical properties and are resistant to corrosion by water at temperatures more than 300 °C. Consequently, stainless steels are commonly used for structural components in

water-cooled power reactors. They are also utilized in fuel element cladding as well as structural material in fast reactors. Pressure vessels are made of low-alloy, carbon steels lined with corrosion resistant alloy. There are several potential uses for nickel-base alloys. The properties of these stainless steel materials are described below [12].

### **2.5.1. Stainless Steels alloys for pressure vessels and in-core structural materials**

Stainless steel contains chromium which ensures resistant to corrosion, tarnishing and rust. Stainless steels vary widely in composition and are classified according to the metallurgical phase produced on solidification of the metal and there are more than 250 different stainless steels [58]. The main grades of stainless are divided into four major groups/classes namely austenitic, ferritic, martensitic and duplex (austenite and ferrite). The high corrosion resistance of these steels is derived from the ability of the alloy to form a protective, self-repairing oxide film, subject to the availability of oxygen in the environments surrounding the alloy [59].

Stainless steels possess strength and toughness at both extremes of the temperature scale, yet can be fabricated into intricate shapes for many uses [60]. The corrosion resistance of stainless steel is the result of the addition of minimum 11% Cr. In addition, steels with the minimum Cr content and too high carbon content ( $\geq 0.03\%$ ) are susceptible to precipitation when the metal is welded or heat treated in the temperature range 500–800 °C [58].

### **2.5.2. Austenitic Stainless Steel**

Austenitic stainless steels have excellent formability, corrosion resistance and also offer rather easy processing as well as good forming ability and corrosion with a great structure stability, which allows their use in a large temperature range. They are not tempered but cold-work strengthened and has a good long term mechanical behaviour. Austenitic steels contain 15 %



to 30 % chromium, 2 % to 20 % nickel and the rest is Iron (for enhanced surface quality, formability and increased corrosion and wear resistance) [60, 61].

### 2.5.3. Effect of Radiation Damage on Mechanical Properties of Stainless Steel

Stainless steels are selected for corrosion resistance, high-temperature strength, ductility and toughness as illustrated in Table 2.3.

Table 2.3: Material property and their Damage effects on Microstructure [12, 62]

STRUCTURAL AND MECHANICAL	RADIATION DAMAGE EFFECTS
<b>Hardness and strength</b>	Increases in radiation hardening due to increase in formation and growth of defects cluster and mainly dislocation loops
<b>Ductility</b>	Decreases on radiation embrittlement
<b>Creep</b>	Enhances on radiation-induced and radiation-enhanced due to increases defects and diffusion-rates
<b>Fatigue</b>	Low cycle fatigue life decreases due to embrittlement; High cycle fatigue life increases due to hardening
<b>Density</b>	Decreases in swelling on irradiation due to formation and growth of voids and gas bubbles, cavities, depleted zones
<b>Electrical resistivity</b>	Increases on irradiation due to increased defect concentration
<b>Conductivity</b>	Decreases on irradiation due to increased defects concentration
<b>Thermal conductivity</b>	Decreases on irradiation due to increased defects concentrations

#### 2.5.4. Mechanical Strength Parameters

Mechanical testing plays an important role in evaluating fundamental properties of engineering materials as well as in developing new materials and in controlling the quality of materials for use in design and construction. If a material is to be used as part of an engineering structure such as the nuclear reactor that will be subjected to a load (i.e thermal loading), it is important to know the material's strength to aid in deciding on the part of the reactor that such material could function very well, since different parts of the reactor are subjected to different loads.

The most common type of test used to measure the mechanical properties of a material is the Tension Test. Tension test is widely used to provide a basic design information on the strength of materials and is an acceptance test for the specification of materials. The major parameters that describe the stress-strain curve obtained during tension test are the tensile strength (UTS), yield strength or yield point (YS), Young's or Elastic modulus (E), percent elongation ( $\Delta L$  %) and the Breaking or fracture Strength. Bulk Modulus can also be found by the use of this testing technique.[63] The parameters are illustrated in  $\sigma - \epsilon$  plot of Figure 2.8.

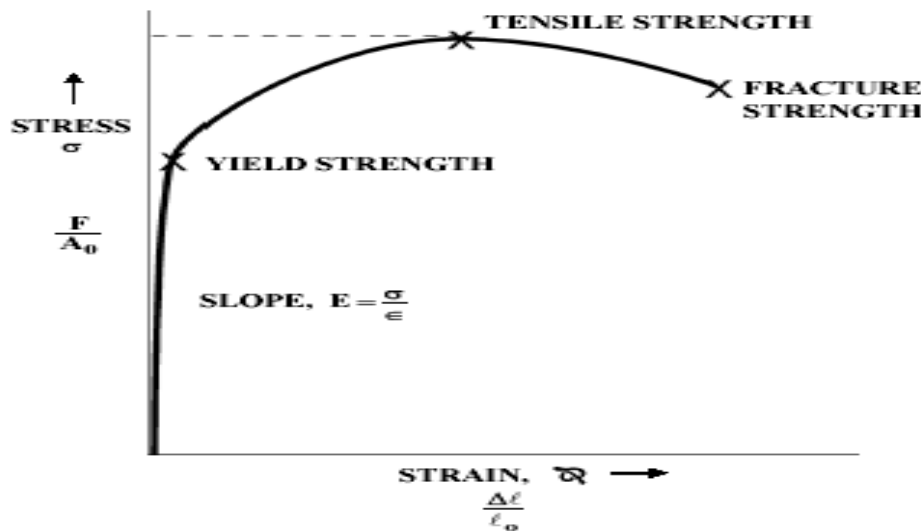


Figure 2.8: A typical Stress-Strain Curve for Fe-Ni-Cr Alloys [63]

#### 2.5.4.1 Young's Modulus

Young's Modulus also known as elastic Modulus or modulus of elasticity is the measure of the stiffness of an elastic material and is a quantity used to characterize materials. It is defined as a ratio of the stress (force per unit area) along an axis to strain (ratio of the deformation over initial length) along that axis in the range of stress in which Hooke's law holds. It is therefore the slope of the part of the strain- stress curve that obeys the Hooke's Law [64].

Young's Modulus is mathematically expressed as:

$$E \equiv \frac{\text{Tensile Stress}}{\text{Extensional Strain}} = \frac{\sigma}{\epsilon} = \frac{F/A_0}{\Delta L/L_0} = \frac{FL_0}{A_0\Delta L} \quad (2.44)$$

where  $E$  is the Young's modulus (modulus of elasticity),  $F$  the force exerted on the metal under tension,  $A_0$  the original cross-sectional area through which the force is applied,  $\Delta L$  the amount by which the length of the object changes, and  $L_0$  the original length of the material.

#### 2.5.4.2 Tensile Strength

The tensile strength which normally called ultimate tensile strength is the stress obtained at the highest applied force and it is the maximum stress on the engineering stress – strain curve. In many ductile materials such as the Face Centered Cubic (FCC) material under consideration, deformation does not remain uniform. At some point, one region deforms more than other areas and a large local decrease in the cross-sectional area occurs. It is also the point at which necking begins. It is useful in comparing materials and it permit the estimation of other properties, which are more difficult to measure. [64]

#### **2.5.4.2 Fracture or Breaking Strength**

Fracture strength, also known as breaking strength, is the engineering stress at which a material fails through fracture. This is usually determined for a given specimen by a tensile test, which charts the stress-strain curve (see Fig. 2.8). The final recorded point is the fracture strength.

Ductile materials have a fracture strength lower than the ultimate tensile strength (UTS), whereas in brittle materials the fracture strength is equivalent to the UTS. If a ductile material reaches its ultimate tensile strength in a load-controlled situation, it will continue to deform, with no additional load application, until it ruptures. However, if the loading is displacement-controlled, the deformation of the material may relieve the load, preventing rupture. [64]

#### **2.5.4.4 Yield Strength**

Yield strength is an indication of maximum stress a material can take without a plastic deformation. Beyond the yield point of the material, it exhibits a specified permanent deformation and is practically expressed as an elastic limit approximation [63].

Yield is very important in engineering structural design such as component that must support loads in operation so that the component will not deform plastically. Therefore, materials with sufficient yield strength are normally selected for design purposes [8].

In reactor design or any design applications, the yield strength is often used as an upper limit for allowable stress that can be applied so that that material will work with a precise dimensional tolerance. Hence, materials without clear distinct yield point, yield strength is usually stated as stress at which permanent deformation of 0.2 % of the original dimension will result (usually termed as 0.2 % offset).

## 2.5 COMPUTER SIMULATIONS OF IRRADIATION DAMAGE AND INDUCED MECHANICAL DEGRADATION

Three principal methods are used to simulate the behavior of atoms in a displacement material. These are Binary Collision Approximation (BCA) Method, Molecular Dynamics (MD) Method and the Kinetic Monte Carlo (KMC) Method [48].

### 2.6.1.1 Binary Collision Approximation (BCA) Method

The binary collision approximation is a method used in ion irradiation physics to enable efficient computer simulation of the penetration depth and defect production by energetic ions (>keV) ions in solids. [65].

A binary collision between a projectile and a target atom is calculated in the BCA simulation and the final position and velocity of the projectile and the target atom at each collision are obtained analytically in a two-body interatomic potential  $V(r)$ , expressed as:

$$V(r) = \frac{Z_1 Z_2 e^2}{r} \Phi\left(\frac{r}{a}\right) \quad (2.45)$$

where  $Z_1$  and  $Z_2$  are the atomic numbers of the energetic ion and the target atoms,  $e$  is the electric charge,  $r$  the distance and  $a$  is an empirical screening length which depends on the atomic numbers of the two atoms by the semi-empirical formula[49]:

$$a = \frac{0.8854 a_{Bohr}}{Z_1^{0.23} + Z_2^{0.23}} \quad (2.46)$$

where  $a_{Bohr}$  is the Bohr radius (the radius of the hydrogen atom  $0.53\text{\AA}$ ).  $\Phi$  is the “universal” screening function determined by exact fitting formula of the calculated interatomic potentials of 521 randomly selected element combinations given by:

$$\Phi \left[ \frac{r}{a} \right] = \sum_{i=1}^4 A_i \exp \left[ -B_i \left( \frac{r}{a} \right) \right] \quad (2.47)$$

In this research, BCA simulation was implemented using SRIM-TRIM code and the Moliere approximation to the Thomas-Fermi potential [66] was employed. Figure 2.9 shows the trajectory of two particles interacting according to a conservative central repulsive force.

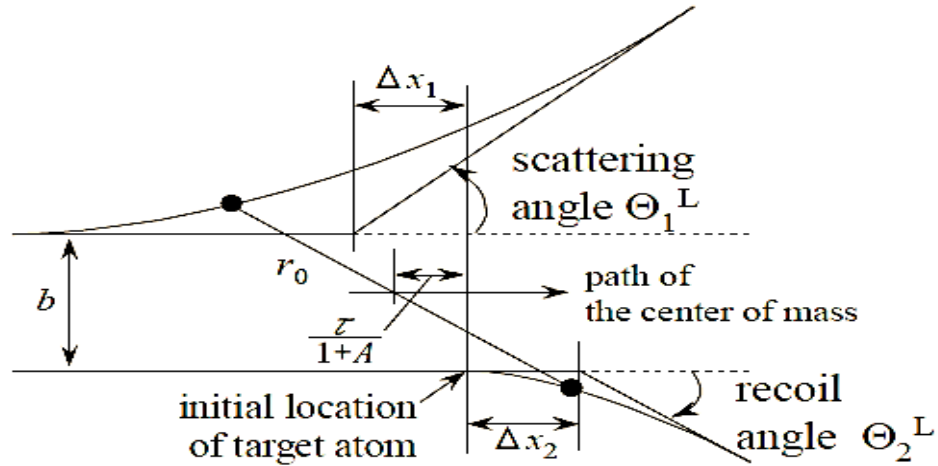


Fig 2.9: The trajectory of two particles interacting according to a conservative central repulsive force in the laboratory system showing the positions of the projectile and the target atom correspond to the apsis of the collision [67].

The scattering angle in the center-of-mass system (CM-system) is

$$\theta^{CM} = \pi - 2b \int_{r_0}^{\infty} \frac{1}{r^2 g(r)} dr, \quad (2.48)$$

$$g(r) = \sqrt{\left( 1 - \frac{b^2}{r^2} - \frac{V(r)}{E_r} \right)} \quad (2.49)$$

$b$  is the impact parameter,  $E_r = E_0 m_1 / (m_1 + m_2)$  is the relative kinetic energy,  $E_0$  is the incident kinetic energy of the projectile,  $r_0$  is the solution of  $g(r) = 0$ ,  $m_1$  and  $m_2$  are the mass of the projectile and the target atom, respectively. The trajectories of particles are approximated as the asymptotes of them in the laboratory system (L-system). So they consist of linkage of straight-line segments. The starting point of the projectile and the

recoil atom after a collision is given by  $\Delta x_1$  and  $\Delta x_2$ , which are the shifts from the initial position of the target atom shown in Fig. 2.9:

$$\Delta x_1 = \frac{2\tau + (A-1)b \tan(\theta/2)}{1+A} \quad (2.50)$$

$$\Delta x_2 = b \tan(\theta/2) - \Delta x_1 \quad (2.51)$$

where

$$\tau = \sqrt{r_0^2 - b^2} - \int_{r_0}^{\infty} \left\{ \frac{1}{g(r)} - \frac{r}{\sqrt{r^2 - b^2}} \right\} dr \quad (2.52)$$

and the mass ratio  $A = m_2 / m_1$ ;  $r$  is the atomic distance

The SRIM-TRIM code evaluates the energy loss by electron excitation for each collision. The four-parameter fitting formula (eqn 2.50) for hydrogen of the electronic stopping cross section which was originally proposed by Varelas and Biersack [68, 69] was employed.

$$S_e^H(E)^{-1} = (S_{LOW}^H)^{-1} + (S_{HIGH}^H)^{-1} \quad (2.53)$$

where

$$S_{LOW}^H = A_1 E^{0.45} \quad (2.54)$$

$$S_{HIGH}^H = \frac{A_2}{E} \ln \left[ 1 + \frac{A_3}{E} + A_4 \right] \quad (2.55)$$

and four parameters  $A_1, A_2, A_3$ , and  $A_4$  are derived from fitting experimental data [68]. The symbol  $S$  in Equation (2.53-2.55) is the Bethe's stopping-power formula [33, 70].

The BCA approach provides a good approximation to the collision stage, since the neglected many-body interactions make little contribution to the atom trajectories at collision energies well above the atom displacement energy. At energies near or even less than the displacement energy, ballistic features of cascades such as replacement-collision sequences and focused-collision sequences can be reasonably captured by BCA calculations. At primary recoil energies above approximately 20 keV, cascades may have more than one damage region. Because the mean free path between high-energy collisions of a recoil atom increases with energy, higher energy cascades will consist of multiple damage regions or sub-cascades that are well separated in space due to high-energy

collisions. Channeling of primary or high-energy secondary recoils also contributes to sub-cascade formation when the channeled recoils lose energy and de-channel.

### 2.6.2. Molecular Dynamics (MD) Method

MD simulation is based on Newton's second law of motion with total force on an N-atom system as

$$F(r_1, r_2, \dots, r_N) = \sum_i m_i a_i = \sum_i m_i \frac{d^2 r}{dt^2} \quad (2.56)$$

where  $F_i$  is the force exerted on the particle  $i$ ,  $m_i$  is the mass of particle  $i$ ,  $a_i$  is the acceleration of particle  $i$ ,  $r_i$  is position and  $t$  is time-step.[71]

MD simulation generally proceeds as

- Given the initial positions and velocities of every atom, and using the provided interatomic potential, the forces on each atom were calculated.
- Using the information gathered from above, the initial positions are advanced toward lower energy states through a small time interval (called a time-step,  $\Delta t$ ), resulting in new positions, velocities, etc.
- With these new data as inputs, the above steps are repeated, for more than thousands of such time-steps until an equilibrium was reached, and the system properties do not change with time.

During and after equilibration, various raw data are stored for each or some time-steps that include atomic properties, energies, forces, etc. Properties that are calculated directly or via statistical analysis from these data are

- Basic Energetics, structural and mechanical properties (Note that some of these data are used to fit the potentials empirically,)



- Thermal expansion coefficient, melting point, and phase diagram in terms of pressure and volume [71].

The simulation flow diagram of the MD run is as shown in Fig. 2.10;

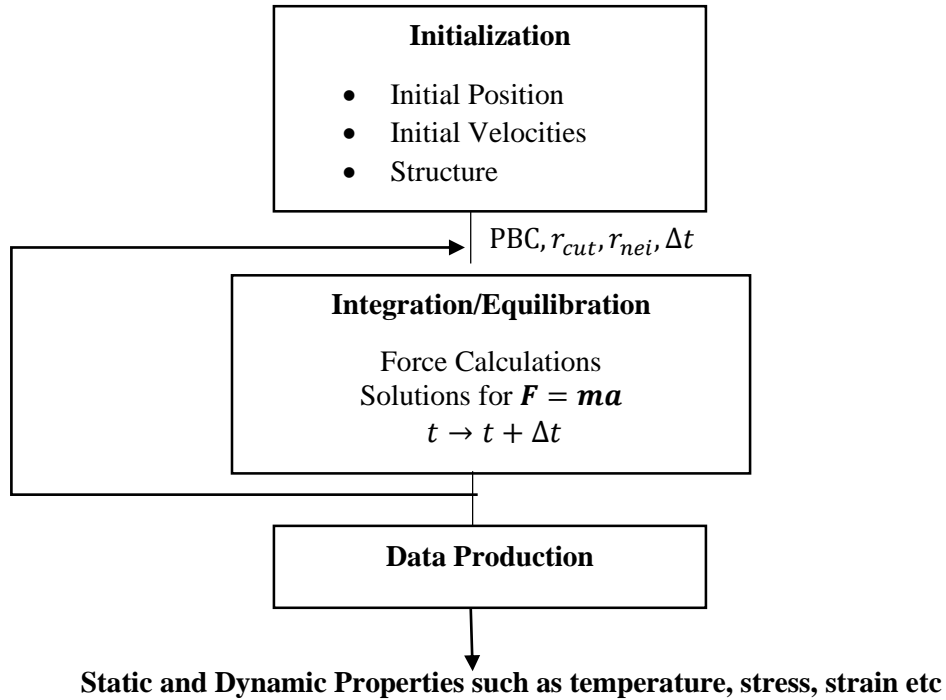


Fig. 2.10: Molecular Dynamics Simulation flow chart [71]

MD is a computationally intensive method for modelling atomic systems on the appropriate scale for the simulation of displacement cascades and provides a realistic description of atomic interactions in cascades [72]. Molecular Modeling is concerned with the description of the atomic and molecular interactions that govern microscopic and macroscopic behaviors of physical systems [73]. Using realistic interatomic potentials and appropriate boundary conditions, the fate of all atoms in a volume containing the cascade can be described through the various stages of cascade development. The analytical interatomic potential functions describe the force on an atom as a function of the distance between it and the other atoms in the system. It account for both attractive and repulsive forces in order to obtain stable lattice configurations.

In MD simulations as shown in Figure 2.11, the total energy of the system of atoms being simulated is calculated by summing over all the atoms. The forces on the atoms are used to calculate acceleration according to  $F = ma$ , yielding the equations of motions for the atoms. The computer code solves these equations numerically over very small time steps, and then recalculates the forces at the end of the time step, to be applied in the calculations in the next time step. The process is repeated until the desired state is achieved

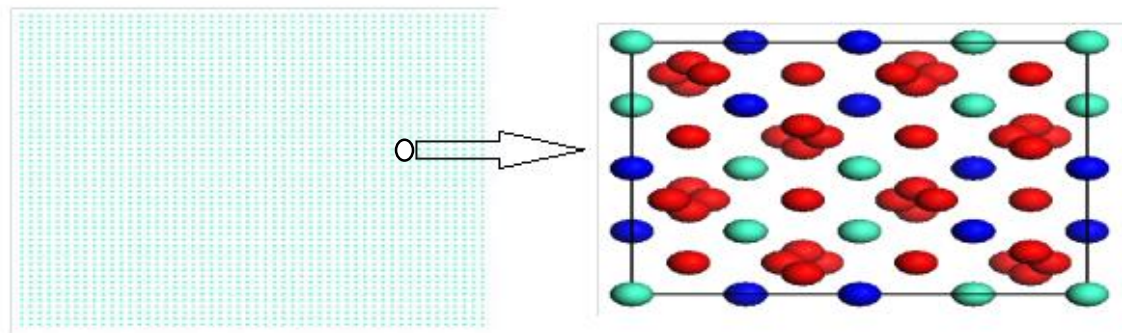


Fig 2.11: Molecular Dynamics Simulation of a unit cell of the material [74]

Time steps in MD simulation must be very small ( $5.0 - 10.0 \times 10^{-15}$  s), so MD simulations are generally run for not more than 100 ps. As the initial primary kinetic energy  $E$  increases, larger and larger numerical crystallites are required to contain the event. The size of the crystallite is roughly proportional to  $E$ , and  $E^2$  is the required computing time-scales. The demand on computing time limits the statistical capabilities of MD simulation, which provides a detailed view of the spatial extent of the damage process on an atomic level that is not afforded by other simulation method. A cascade simulation begins by thermally equilibrating a block of atoms that constitutes the system being studied, and the process allows the determination of the lattice vibrations for the simulated temperature. Next, the cascade simulation is initiated by giving one of the atoms a specified amount of kinetic energy and an initial direction. Several cascades must be run in order to obtain results that can be used to represent the average behaviour of the system at any energy and temperature [72].

### **2.6.3. Kinetic Monte Carlo (KMC) Method**

Kinetic Monte Carlo attempts to overcome the limitation of time-scale problem associated with MD by exploiting the fact that the long-time dynamics of this kind of system typically consists of diffusive jumps from state to state. Rather than following the trajectory through every vibrational period, these state-to-state transitions are treated directly. Given a set of rate constants connecting states of a system, KMC offers a way to propagate dynamically correct trajectories through the state space. If the rate catalog is constructed properly, the easily implemented KMC dynamics can give exact state-to-state evolution of the system, in the sense that it will be statistically indistinguishable from a long term molecular dynamics simulation. KMC is the most powerful approach available for making dynamical predictions at the mesoscale timestep without resorting to model assumptions. It can also be used to provide input to and/or verification for higher-level treatments such as rate theory models [34, 75].

### **2.6.4. Computer Simulation Codes**

#### **2.6.4.1 SRIM – TRIM Code**

TRIM is the acronym of Transport of Ions in Matter, while SRIM is stopping and range of ions in matter [45]. TRIM is a BCA code that uses Monte Carlo techniques to describe the trajectory of the incident particle and the damage created by that particle in amorphous solids and has all the properties or theoretical background of the BCA method. TRIM uses a maximum impact parameter set by the density of the medium and a constant mean free path between collisions which is related to this. Stochastic methods are used to select the impact parameter for each collision and to determine the scattering plane. ALICE, PHITS, MARS etc. are other BCA codes which are used for damage assessments.

TRIM is a Monte Carlo simulation code embedded in SRIM code and widely used to compute a number of parameters relevant to radiation damage exposure calculation to

nuclear structural material and has the capability to compute a common radiation damage exposure unit known as the atomic displacements per atom (dpa) and other defects, interstitials and vacancies.. TRIM code can calculate the stopping and range of ions from 10 eV to 2 GeV into any kind of matter using a quantum mechanical treatment of ion-atom collision [75].

The moving atom is referred to as an "ion", and all target atoms as "atoms". The calculation is made very efficient by the use of statistical algorithms which allow the ion to make jumps between calculated collisions, and then averaging the collision results over the intervening gap. During the collisions, the ion and atom have a screened Coulomb collision, including exchange and correlation interactions between the overlapping electron shells. The ion has long range interactions creating electron excitations and Plasmon within the target. These are described by including a description of the target's collective electronic structure and interatomic bond structure when the calculation is setup [76].

SRIM is a group of computer programs which calculate interaction of ions with matter and it consists of two main program modules and several programs for specialized tasks. The core modules are the Tables of Stopping and Ranges and Monte Carlo Transport Calculation. The code also contains tables and plots concerning experimentally determined ranges for the most common materials [77].

The TRIM window is used to input data on the ion, target layers and the type of TRIM calculation that is needed. The output lists or plots the following:

- Three-dimensional distribution of the ions in the solid and its parameters, such as penetration depth, spread along the ion beam (called straggle) and perpendicular to it, all target atom cascades in the target are followed in detail concentration of vacancies, sputtering rate, ionization and phonon production in the target material.
- Energy partitioning between the nuclear and electron losses, energy deposition rate.

The programs can be interrupted at any time, and then resumed later, have a very

easy-to-use user interface and built-in default parameters for all ions and materials. These features have made SRIM immensely popular. However, it doesn't take account of the crystal structure nor dynamic composition changes in the material that severely limits its usefulness in some cases.

Other approximation of the program include:

- The electronic stopping power:- an averaging fit to the large number of experiments.
- The interatomic potential:- a universal form which is an averaging fit to the quantum mechanical calculations.
- The target atom:- which reaches the surface and then causes surface sputtering if it has momentum and energy to pass the surface barrier. The system is layered, i.e. simulation of materials with composition differences in 2D or 3D is not possible [77, 78].

#### **2.6.4.2 Large-Scale Atomic/Molecular Massively Parallel Simulator (LAMMPS)**

LAMMPS is a parallel general purpose particle simulation code developed at Sandia National Laboratories, USA, with contributions from many labs throughout the world [74]. LAMMPS integrates Newton's equations of motion for collections of atoms, molecules, or macroscopic particles that interact via short or long range forces with a variety of boundary conditions. LAMMPS performs structural optimization of the atomic positions and cell parameters as well as molecular dynamics calculations. Applications are manifold, and researchers use LAMMPS to predict a variety of phenomena and properties, such as diffusion of molecules in polymer matrices, solubility parameters and miscibility, surface adhesion, viscosity, friction, density etc. for both inorganic and organic systems. LAMMPS runs efficiently on single-processor desktop or laptop machines, but is also designed for

parallel computers, hence it can model systems with only a few particles up to millions or billions [79, 80]. Other codes aside LAMMPS for evaluation of mechanical damage are AMBER and CHARMM.

#### **2.6.4.3 Visual Molecular Dynamics (VMD)**

Visual Molecular Dynamics is a code designed to visualize dump or output files from LAMMPS and is useful in visualizing the stresses surrounding each atom. VMD can also be used to animate and analyze the trajectory of a molecular dynamics (MD) simulation. In particular, VMD can act as a graphical front end for an external MD program by displaying and animating a molecule undergoing simulation on a remote computer. This molecular graphics program is designed for interactive visualization and analysis and runs on all major Unix workstations, Apple MacOS X, and Microsoft Windows [81].

VMD provides a wide variety of methods for rendering and coloring a molecule and can act as a graphical front end for an external MD program by displaying and animating a molecule undergoing simulation on a remote computer [82]. The Ovito code is also a visualization code for MD simulations.

## **CHAPTER THREE: RESEARCH METHODOLOGY**

In this chapter, the research methodologies adopted in assessing the effects of neutron irradiation on microstructural damage and mechanical degradation of grades of Fe-Ni-Cr stainless steels which might be candidate alloys for SCWR Pressure Vessel design. Simulations of irradiation damage in the steels were implemented by SRIM-TRIM Code, whereas the mechanical degradation was simulated using LAMMPS along with the VMD and MATLAB.

### **3.1. SELECTION OF Fe-Ni-Cr ALLOYS**

#### **3.1.1 Structural and In-Core Reactor Materials**

The qualification of materials for the SCWR design has been one of the key challenges associated with the design and development of the nuclear power plant.

In deciding on the optimum materials for the design of SCWR structures where the temperatures will be significantly above 300 °C, or irradiation doses 10 – 150 dpa, candidate structural materials might be primarily ferritic or martensitic steels and low swelling austenitic stainless steels [17]. For Fe-Cr-Ni alloys acceptable mechanical behaviour and dimensional stability is also possible though there is currently an insufficient knowledge base for predicting Stress Corrosion Cracking (SCC) or Irradiation Assisted Stress Corrosion Cracking (IASCC) behaviour under supercritical water conditions. Some austenitic stainless steel alloys have demonstrated low swelling in doses of up to 10-30 dpa in thermal neutron spectrum in the temperature regime of 200-500 °C [12, 47].

Ferritic/ Martensitic (F/M) as well as austenitic stainless steels have been used throughout the first through to third generation as in-core materials as well as pressure vessels; and as such has led to them being classified as Generation IV fission reactors candidate materials [9].

But due to the harsh environmental conditions of high stress cracking corrosion and high temperature the Generation IV in-core materials are to be exposed to, low swelling austenitic stainless steels with high Ni and Cr components as shown in the phase diagram shown in Figure. 3.1 , which are basically alloying elements excellent for corrosion resistance and high mechanical strength [9].

Hence in assessing materials for the pressure vessel design, austenitic stainless steels grades SS304, SS316, SS308 and SS309 were considered in the research work based on the above evidence and also because of their excellent corrosion and high temperature strength although their void swelling is inferior to that of Ferritic/Martensitic stainless steels.

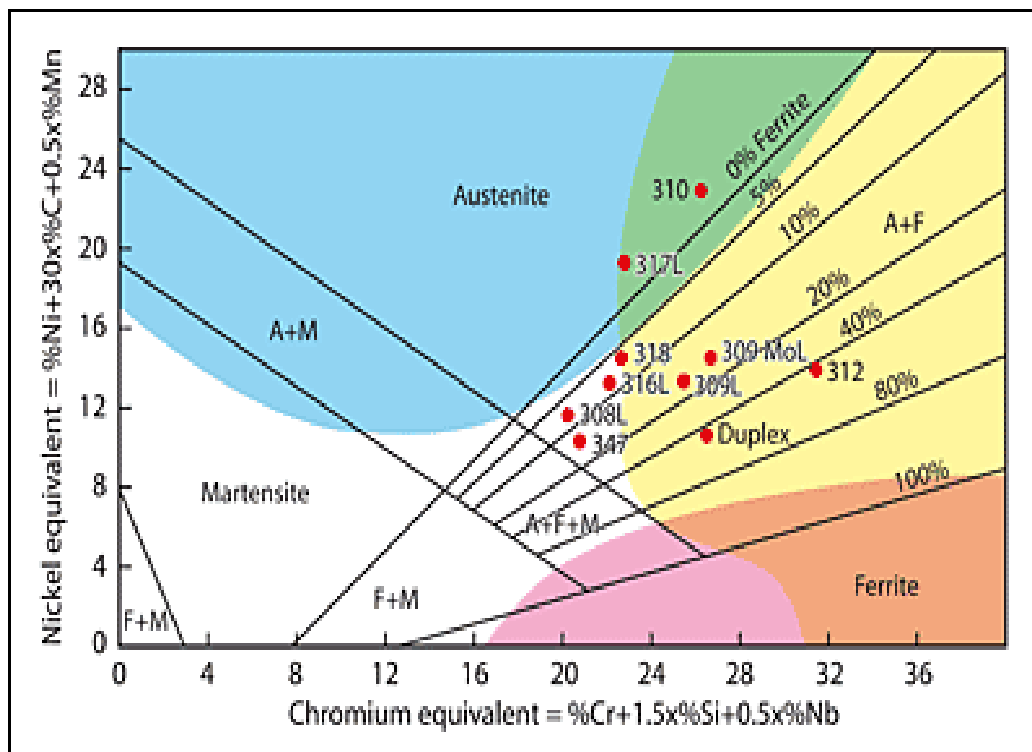


Figure 3.1: Phase diagram of Stainless Steel Alloys [33]



### 3.1.2 Characterization and Properties of Selected Alloys

The austenitic stainless steels have oxidation limit of 900-1100 °C, Specific heat capacity of 510 J/Kg/ °C, Thermal conductivity, of 16 W/M/ °C and thermal expansion  $16 \times 10^{-6}$  °C [61]. Table 3.1 shows the grades which after thorough literature review were considered in the research. Austenitic (fcc) has good corrosion resistance and ductility over wide temperature range, depending on precise composition. No ductile-brittle transition so used for cryogenic applications such as food production tools [84].

Table 3.1: Composition for Austenitic grades of Fe-Ni-Cr alloys selected for Damage Assessment at SCW conditions [84 -88], designated by AISI and BS codes

Coding System		% Fe	%Ni	%Cr	%C	% Mn	Other Element	Tensile Strength (MPa)	Youngs Modulus (GPa)
AISI	BS								
304	304S15	69.42	9.50	19.00	0.08	2.0	-	580	193
308	-	68.92	10.00	19.00	0.08	2.0	-	515	193
309	-	61.30	13.50	23.00	0.20	2.0	-	620	200
316	316S16	66.92	12.00	17.00	0.08	2.0	Mo(2%)	627	193

\* American Iron and Steel Institute (AISI) and British Standard (BS) System

### 3.2. NEUTRON IRRADIATION DAMAGE ASSESSMENT BY BCA

Neutron Irradiation damages in the Fe-Ni-Cr alloys SS304, SS308, SS309 and SS316 were assessed using SRIM-TRIM code which relied on the universal potential of Zeigler et al. and Robinson were used [78, 89]. The 2013 version of SRIM-TRIM code was employed in the radiation damage assessment along with the required input file. The setup window and input parameters used for the simulation exercise and output files are presented in Sections 3.2.1, 3.2.2 and 3.2.3.

#### 3.2.1 Estimation of Energy Level at 30 dpa of Thermal Neutrons

##### Spectrum

Thermal neutron spectrum for Supercritical Water- Cooled Reactor was assumed to produce a dose of 10-30 dpa [6, 9] Hence, for a stainless steel (with iron as major component) exposed to neutron fluence of  $5 \times 10^{19}$  neutrons/cm<sup>2</sup>, the neutron energy was calculated from the rate equation (2.11)

$$dpa = \left[ \frac{\dot{N}_d(E).t}{N} \right] \approx [\Phi(E).t]. \frac{\sigma_s(E)}{AE_d} . E \quad (3.1)$$

making E the subject of the equation (3.1) gives

$$E = \frac{dpa \times AE_d}{[\Phi(E).t] \times \sigma_s(E)} \quad (3.2)$$

where  $\Phi(E) \cdot t$  is the fluence =  $5 \times 10^{19}$  neutrons/cm<sup>2</sup>, dpa = 30, A = 56 for iron (main alloy component) and  $E_d = 25$  eV. The scattering cross section,  $\sigma_s(E)$  for neutrons was roughly  $3\pi R^2$ , where  $R = 1.3 \times 10^{-15} A^{1/3}$  m is the radius of the nucleus; hence,  $\sigma_s(E) \approx 2.3 \times 10^{-24}$  cm<sup>2</sup>. Consequently,

$$E = \frac{30 \times 56 \times 25}{5 \times 10^{19} \times 2.3 \times 10^{-24}} = 365 \text{ MeV}$$

### 3.2.2 Estimation of Energy Level at 150 dpa of Fast Neutrons Spectrum

Fast neutron spectrum for Supercritical Water- Cooled Reactor was also assumed to produce a dose of 150 dpa [6, 9]. Hence, for a stainless steel (iron exposed to neutron fluence of  $5 \times 10^{19}$  neutrons/cm<sup>2</sup>, using equation (3.52) above

$$E = \frac{150 \times 56 \times 25}{5 \times 10^{19} \times 2.3 \times 10^{-24}} = 1.82 \text{ GeV}$$

### 3.2.3 SRIM-TRIM Setup and Input Requirements

TRIM was accessed from the main menu of SRIM. The TRIM Setup Window was used to input the data on the ion, target, and the type of TRIM calculation desired.

**TRIM (Setup Window)**

**Read Me** **TRIM Demo** **Restore Last TRIM Data**

**ION DATA** **Symbol** **Name of Element** **Atomic Number** **Mass (amu)** **Energy (keV)** **Angle of Incidence**

PT U Uranium 92 238 365000 0

**TARGET DATA** **Target Layers**

**Add New Layer** **Layer Name** **Width** **Density (g/cm3)** **Compound** **Corr** **Gas**

X Stainless Steel(316) 46 cm 7.909 1

**Input Elements to Layer** **Add New Element to Layer** **Compound Dictionary**

Symbol	Name	Atomic Number	Weight (amu)	Atom Stoich or %	Damage (eV)	Disp	Latt	Surf
PT Fe	Iron	26	55.84	0.66	66.9	25	3	4.3
PT Ni	Nickel	28	58.69	0.12	12.0	25	3	4.4
PT Cr	Chromium	24	51.99	0.17	17.0	25	3	4.1
PT C	Carbon	6	12.01	0.00	00.0	28	3	7.4
PT Mn	Manganese	25	54.93	0.02	02.0	25	3	2.9
PT Mo	Molybdenum	42	95.94	0.02	02.0	25	3	6.8

**Special Parameters** **Name of Calculation** **Stopping Power Version** **Output Disk Files** **Resume saved TRIM calc.** **Save Input & Run TRIM**

U (365000) into Stainless Steel(316) SRIM-2008

**AutoSave at Ion #** 10 **Plotting Window Depths** **Min** 0 **Max** 200000

**Total Number of Ions** 100 **Collision Details** 100000 **Special "XYZ File" Increment (eV)**

**Problem Solving** **Quit**

Figure 3.2: TRIM Input Parameter Window showing all inputs for Stainless Steel grade 316 assessment

The ion data and input parameters used to calculate the radiation damage by the SRIM – TRIM Code is shown in Table 3.2, while Table 3.3 show the target data and the input parameters.

As shown in Table 3.1 only 4 alloys (SS304, SS308, SS309 and SS316) were bombarded with 100 Uranium neutron Ions (incident projectiles are considered by TRIM code as Ions and also neutrons cannot be entered straight into the setup but elements that its neutrons are being considered) of energy 365 MeV for the thermal neutron spectrum and 1.82GeV for the fast neutron spectrum. The “Ions with specific energy/angle/depth (full cascade) using TRIM.DAT” damage type [78], in the 2013 version of SRIM-TRIM code menu, was employed. (See Appendix I)

Table 3.2: Ion Data and input parameters used in the SRIM – TRIM Code

<b>Ion Data</b>	<b>Name/Value</b>
<b>Incident Ion type</b>	Thermal and Fast Neutrons from Uranium
<b>Symbol for the incident ion</b>	U
<b>Atomic number</b>	92
<b>Atomic mass</b>	238.051 amu
<b>Incident Ion Energy</b>	365 MeV (thermal neutrons) and 1.82 GeV (fast neutrons)
<b>Damage Type</b>	Ions with specific energy/angle/depth (full cascade) using TRIM.DAT (Appendix I)
<b>Angle of incident</b>	0

Table 3.3: Target Data and input parameters in the SRIM – TRIM Code

<b>Target data</b>	<b>Name/Value</b>
<b>Layer name</b>	Stainless Steel (304, 308, 309 and 316)
<b>Compound Correction</b>	1
<b>Width</b>	0.46 m (equivalent RPV thickness)
<b>Density</b>	7.83977236 g/cm <sup>3</sup>
<b>Atomic density</b>	6.031x10 <sup>22</sup> atom/cm <sup>3</sup>
<b>Depth</b>	2.0 x10 <sup>-5</sup> m and 4.0 x10 <sup>-5</sup> m (Set up)
<b>Calculated Ions</b>	100

Table 3.4: TRIM.IN contains setup parameters for TRIM Simulation of type 304

<b>1. SRIM - 2013.00version:-</b> This file however controls TRIM Calculations.									
<b>2. Ion:</b> Z1 , M1, Energy (keV), Angle, Number, Bragg Corr, AutoSave Number.									
92	238	365000	0	100	1	10			
<b>3. Cascades</b> (1=No;2=Full;3=Sputt;4-5=Ions;6-7=Neutrons), Random Number Seed, Remin.									
5						0	0		
<b>4. Diskfiles</b> (0=no,1=yes): Ranges, Backscatt, Transmit, Sputtered, Collisions (1=Ion;2=Ion + Recoils), Special EXYZ.txt file									
	1	1	1	1	2	100000			
<b>5.</b>	Target material :				Number of Elements & Layers				
	"U (365000) into Fe-Ni-Cr Alloy (SS304) "				5	1			
<b>6. PlotType</b> (0-5); <b>Plot Depths:</b> Xmin, Xmax(Ang.) [=0 0 for Viewing Full Target]									
0	0				200000				
<b>7. Target Elements:</b> Z Mass(amu)									
Atom 1 = Fe =		26	55.847						
Atom 2 = Ni =		28	58.69						
Atom 3 = Cr =		24	51.996						
Atom 4 = C =		6	12.011						
Atom 5 = Mn =		25	54.938						
<b>8. Layer</b>	Layer Name /	Width	Density	Fe(26)	Ni(28)	Cr(24)	C(6)	Mn(25)	
Numb.	Description(Ang)	(g/cm3)		Stoich	Stoich	Stoich	Stoich	Stoich	Stoich
1	"Stainless Steel(304)"	46000000000	7.82399572	.6942	.095	.19	.0008	.02	.02
<b>9. Target layer phases</b> (0=Solid, 1=Gas)									
0									
<b>10. Target Compound Corrections</b> (Bragg)									
1									
<b>11. Individual target atom displacement energies</b> (eV)									
25	25	25	28	25					
Individual target atom lattice binding energies (eV)									
3	3	3	3	3					
Individual target atom surface binding energies (eV)									
4.34	4.46	4.12	7.41	2.98					
<b>12. Stopping Power Version</b> (1=2011, 0=2011)									
0									

**Note: the numbering of lines was done for easy description of the input parameters**

The TRIM.IN file in Table 3.4 contained information, which are in two-line increments, with explanation in the first line which does not contain data, and data values in the next line.

The first line (labelled 1) of TRIM.IN contained the version number of the SRIM code being used.

The 2nd and 3rd lines (labelled 2) contained information about the ion (atomic number, mass, energy and incident angle to the target), the total ions to calculate (20,000), a term called “Bragg Corr” (not used), and the AutoSave number (the TRIM calculation was automatically saved after this number of ions).

The next two lines (labelled 3) contained parameters for calculating: (a) the *Cascades* number declares the type of Damage Calculation (upper right menu of the TRIM Setup window), and (b) a random number seed (zero for the default value) and (c) Reminder

The next two lines (labelled 4) contained instructions about any datafiles that should be created when TRIM starts (these datafiles are described in the menu at the bottom of the TRIM Setup window). Note that the explanation line is quite long and is duplicated here as two lines of text. In the data line, a “0” means no file, and a “1” asks that this file be created. The EXYZ parameter was a number such as 10000 which gives results at every 10000 eV of energy increment.

The data line labelled 5 contained (a) a description of the calculation that would be included in every datafile produced by TRIM (in quotes), and (b) the number of elements in the target and the number of layers in the target. This latter information is necessary because the TRIM.IN file may have several lines of data depending on the number of elements and layers in the target.

The data line labelled 6 gave the type of initial plot that TRIM should display (use “0” for no plot), and the depths of the Viewing Window. This window could cover the entire target depth, or could blow up a small segment of the target so interactions may be seen with greater detail. To default the Viewing Window to the total target depth, you can use “0 0” as the depths.

The data lines labelled 7 defined the elements in the target. First is the chemical symbol, then the atomic number and finally the mass of each target atom. The number of lines must agree with the number of target elements declared above. The first 15 characters in each line were ignored (e.g. “Atom 1 = Fe = ”) and were only included to make the file readable. Only the Z and Mass are used by TRIM.

The section labelled 8 described each layer of the target. Note that the explanations takes up two lines of the TRIM.IN datafile. The “Layer Name” was a description (in quotes) that would appear in all the plots. Next to the layer name was the layer width ( $\text{\AA}$ ), the layer density ( $\text{g/cm}^3$ ), and the relative concentration of each of the elements in that layer of the target.

The next two lines (labelled 9) gave the phase state of the layers, i.e. either a solid or a gas layer.

The next two lines (labelled 10) gave the bonding corrections needed to be applied to the electronic stopping powers of the ion. A “1” meant no special bonding correction.

The next section (labelled 11) gave the damage parameters for the target layers. Each atom had a Displacement Energy, Binding Energy and Surface Binding Energy for each layer. All energies were in units of eV. You can input “0” for the absence of a layer. The final input (labelled 12) was a declaration of which version of SRIM’s Stopping Powers



to use. About every 5 years, the complete stopping theory of SRIM was revisited and all the experimental data of that period is added to the database. Any new ideas on stopping theory were also included. This results in new stopping power concepts, and variations in stopping powers from earlier versions of SRIM.

### 3.2.4 SRIM – TRIM code Simulation Algorithm and Flowchart

The time taken for the completion of the simulation depended on the following; type of calculation and the number of Ions being dealt with. The procedure for the simulation in SRIM-TRIM version 2013 with input file were:

1. ***Choosing the type of TRIM Damage Calculation:*** At the damage calculation corner of the TRIM window, the “Ions with specific energy/angle/depth were selected (full cascade) using TRIM.DAT” type, since only neutrons were considered.
2. ***Selection of Ion type:*** Uranium was selected as the Ion (Only elements were allowed to be selected by the program instead of neutrons particles required for the research hence the need for the type of damage selected).
3. ***Insertion of Ion Parameters:*** The energy of 365 MeV (365000 i.e. converted to keV before entering since the setup only takes values in keV) was inserted into the energy column
4. ***Selection of Target Material:*** Stainless Steel (a default compound) was selected from the Compound Dictionary and was then changed to 304, 308, 309 and 316 based on their elemental composition /Atomic Stoichiometry, respectively.

5. ***Insertion of Atomic Stoichiometry:*** The elemental compositions of those four alloys were entered into their respective columns (e.g. Stainless Steel (304) composed of Fe-0.6942, Cr-0.19, Ni-0.095, C-0.0008, Mn-0.02)
6. ***Insertion of Target Name:*** The name of the target was inserted at its column in the windows setup (e.g. Stainless Steel (304))
7. ***Insertion of Target Thickness:*** The thickness of the material was entered. (i.e. 0.46 m representing PV thickness)
8. ***Setting Special Parameters:*** The total number of ions for the simulation was entered as 100 (since the output files of the collision history of ions greater than 100 from the TRIM.DAT file was above 2GB). Also the plotting window depth was set to 200000Å since that only works with the default unit (angstrom).
9. ***Selection of Output files:*** The output files required for the damage assessment such as vacancies, sputtering etc. were selected.
10. ***Saving of input & Running the TRIM:*** The Save Input & Run TRIM button was clicked to start the simulation.

The flowchart of the simulation for the assessment of irradiation damage of Fe-Ni-Cr to alloy for designing the reactor internals and pressure vessel using the SRIM-TRIM code is shown in Figure 3.3

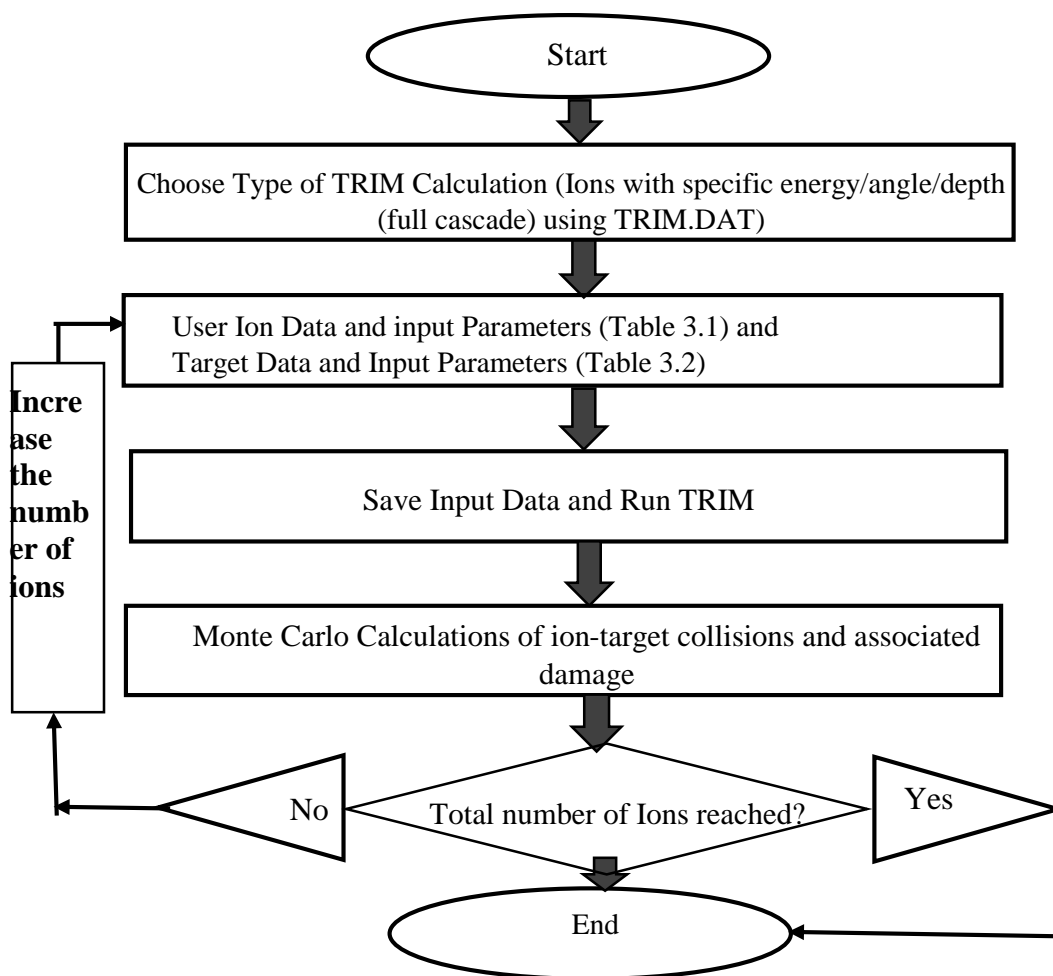


Figure 3.3: SRIM – TRIM Code flowchart for simulation

### 3.2.5 Implementation of SRIM – TRIM Simulation

In simulating the neutron irradiation damage, the selected Fe-Ni-Cr alloys SS304, SS308, SS309, and SS316 were each subjected to 100 neutrons exposure from Uranium (proposed fuel of the SCWR) at neutron particle energy of 365 MeV. Following procedures outlined under the structural algorithm stage, the simulation was performed, each simulation lasting about 7 hours to complete. The output files were then saved with their corresponding data files.

### 3.2.6 SRIM – TRIM Output files

After a successful simulation of the TRIM program for each alloy, the output plots and data files obtained were [77, 78, and 90]:

- **Ion Range**– Determined the final distribution of ions directed into the Fe-Ni-Cr alloys
- **Lateral Ion Range Distribution** – For ion beams incident perpendicular on target, the ion distribution spread out with azimuthal symmetry, and the Lateral Range was merely the average final y-z displacement of the ions assuming a perpendicular incidence of the ion beam.
- **Ionization Energy Losses** – The energy loss of ions to the target electrons. Upon penetrating into the stainless steel the ions interacted immediately with the electrons, both single electrons and collectively; which led to energy loss by the ion to the electrons, represented by Ionization Energy Loss.
- **Phonons** – Described the ion's energy loss to the Target Phonons. Thus when ion collides with a nucleus and the energy of the incident ion was less than the displacement energy (energy required to eject an atom from the lattice site) the atom returned to the lattice site and the recoil energy was transferred into target phonons.
- **Energy to Recoil** – Represented by the plot of Ion energy transferred to the stainless steel and the percentage of energy absorbed by each element.
- **Damage Events** – A collision event (comprising of Displacement, Replacement and Vacancies) and its 3D plot are required. The plot gave the total number of atoms displaced by both the ion and the PKA and all the recoiling target atoms.

- **Sputtering** – An integral sputtering plot which was useful to estimate how many atoms reach the surface and did not possess enough energy to escape.

### 3.3 EVALUATION OF MECHANICAL INTEGRITY OF MATERIALS

The mechanical properties of Fe-Ni-Cr alloys SS304, SS308, SS309 and SS316 were evaluated at SCW conditions by Molecular Dynamics Simulation method employing LAMMPS and VMD. The 30 Sep 2014 edition of LAMMPS, VMD version 1.9.2 and version R2013a of MATLAB were employed. The setup window, input parameters and the output files used for the simulation exercise are presented in the subsequent sections.

#### 3.3.1 LAMMPS Setup and Input Requirements

In running the LAMMPS program, three (3) program files required were

- In.file (input script to create models and for calculation involved in the simulation, (See Appendix II)
- Potential file (contains data about the interatomic bond between atoms, (See Appendix II)
- .exe file (required to run the commands in the in.file)

The LAMMPS input consisted of Initiation, Atom definition, Settings, and Running simulation [80], where the

- **Initiation** – Setting parameters to be defined before atoms were created, such as units, dimension, boundary condition, and atom type.

- **Atom definition** – i.e. atom or molecular topology information required for the simulation.
- **Settings** –specified as force field, various simulation parameters, and output options, etc.
- **Run** – The time step and the number of runs for the simulation were stated at the final stage.

The flowchart for designing the LAMMPS input file is indicated in Fig. 3.4 and a copy of the files used for this simulation in appendix II.

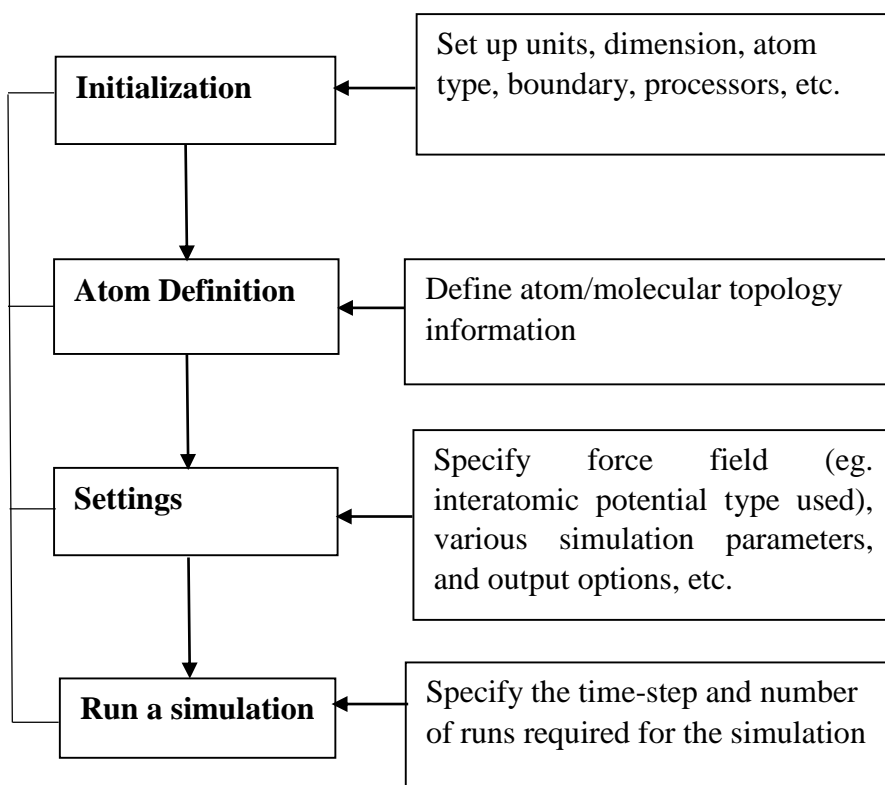


Figure 3.4: Steps followed in designing LAMMPS input file

The Lattice Parameters which were used for the simulation were tabulated in Table 3.5.

Table 3.5: Lattice Parameters used for the LAMMPS Simulations [91].

TREATMENT	LATTICE PARAMETERS			
	SS304	SS308	SS309	SS316
Ambient Temperature	3.5918	3.5907	3.5930	3.5935
300 °C	3.5919	3.5914	3.5942	3.5975
400 °C	3.5613	3.5663	3.5781	3.5864
500 °C	3.5628	3.5642	3.5613	3.5664

### 3.3.2 Interatomic Potential Adapted for the MD Simulation

The critical part of MD simulation was the force calculation, which depended on interatomic potentials. The net force acting on each atom in the system was the result of the interactions with all other atoms, which amounted to a set of rules known as a **force field** or **interaction potential**. Accurate, robust, and transferable force fields were critical to perform physically realistic molecular simulations.

The sum of all forces acting on an atom,  $F$ ,

$$F = \sum m a = \sum m \frac{dv}{dt} = \sum m \frac{d^2 r}{dt^2} = \frac{dp}{dt} \quad (3.3)$$

where  $\mathbf{a}$  is acceleration,  $\mathbf{v}$  is velocity,  $\mathbf{t}$  is time,  $\mathbf{r}$  is position, and  $\mathbf{p}$  is momentum. Since position  $\mathbf{r}$  is a vector, the first and second derivatives,  $\mathbf{v}$  and  $\mathbf{a}$ , and corresponding  $\mathbf{p}$  and  $\mathbf{F}$ , are also vectors. For a constant total Energy  $E$  in time ( $dE/dt = 0$ ), which was the case of isolated system for MD simulations,  $F$  was related to the negative gradient of potential with respect to position, i.e.

$$F = -\nabla U \quad (3.4)$$

$$F_i = m_i \frac{d^2 r_i}{dt^2} = -\frac{dU(r_i)}{dr_i} \quad (3.5)$$

where  $U$  is potential. Knowing the potential of a system as a function of interatomic distance, the force on atoms could be obtained for time evolution of the system [71].

The four common types of potentials mostly used in MD simulations are Pair Potentials, potentials by Embedded Atom Method, Tersoff Potentials, and Potentials for Ionic Solids. The Pair Potential, Tersoff and Potential for Ionic Solids are generally meant for noble gas (i.e. Ar, Ne, Kr, etc.), covalent solids and ionic solids respectively, whereas the embedded atom method (EAM) potential is appropriate for metals and transition metals, such as FCC metals. Hence for the Austenitic Stainless Steel, the EAM was adopted for the simulation.

The EAM potential,  $U_{EAM}$ , consisted of a term for pair interaction and another for embedding energy as a function of electron density  $\rho_i$  at atom  $i$ : [71]

$$U_{EAM} = \sum_{i \neq j} U_{ij}(r_{ij}) + \sum_i F_i(\rho_i) \quad (3.6)$$

where  $F_i(\rho_i)$  is the embedding energy function,  $r_{ij}$  is the scalar distance between atom  $i$  and  $j$ , and atom-atom distances in the x-, y-, and z- axis as

$$r_{ij} = |r_i - r_j| = \sqrt{(x_i - x_j)^2 + (y_i - y_j)^2 + (z_i - z_j)^2} \quad (3.7)$$

In equation (3.6), the first summation notation represented a sum of all unique pair interactions excluding any double counting:

$$\frac{1}{2} \sum_{i \neq j}^N U_{ij}(r_{ij}) = U_{12} + U_{13} + \dots + U_{23} + \dots + U_{34} + U_{35} + \dots + U_{45} + U_{46} + \dots \quad (3.8)$$



The electron density at site  $i$  was the linear superposition of valence-electron clouds from all other atoms:

$$\rho_i = \frac{1}{2} \sum_{j(\neq i)} \rho_j(r_{ij}) \quad (3.9)$$

The net force acting on the atom at a given time was then obtained exactly from the interatomic potential, as a function only of the positions of all atoms.

In calculating the net force, common algorithms for the numerical integration of the Newton's equations of motion and calculation of atomic trajectories are Verlet algorithm, the Velocity Verlet Algorithm, the Predictor-Corrector Algorithm,  $n^{\text{th}}$  order Runge-Kutta, and the Gear Algorithm [71].

Velocity Verlet algorithm was implemented for the numerical integration despite the algorithm though has poor accuracy for large time step (hence  $\Delta t$  must be small), has proved to be fast, simple, stable, time reversible, required low memory, and symplectic (phase, space, volume and energy conserving). In the Verlet scheme, the positions, velocities, and acceleration at time  $t + \Delta t$  were obtained from the corresponding quantities at time  $t$  by advancing the velocity,  $v$ , by a half step, the position  $r$  by a full step using the half-step and then the acceleration,  $a$ , by full step from the potential relationship such that

$$v\left(t + \frac{\Delta t}{2}\right) = v(t) + \frac{1}{2!} a(t) \Delta t \quad (3.10)$$

$$r(t + \Delta t) = r(t) + v(t) \Delta t + \frac{1}{2!} a(t) \Delta t^2 = r(t) + v\left(t + \frac{\Delta t}{2}\right) \Delta t \quad (3.11)$$

$$a(t + \Delta t) = -\left(\frac{1}{m}\right) \frac{dU[r(t + \Delta t)]}{dt} = \frac{F(t + \Delta t)}{m} \quad (3.12)$$

The velocity term  $v$  was advanced by a full step from  $a$  at the previous and current timesteps and expressed it using the half-step advanced  $v$  and full-step advanced  $a$  as

$$v(t + \Delta t) = v\left(t + \frac{\Delta t}{2}\right) + \frac{1}{2}a(t + \Delta t)\Delta t \quad (3.13)$$

and gave the atomic coordinates and velocities at time  $t$  and with the force field  $F=ma$ , the entire future position of the atoms were determined by the  $F = ma$ . The Verlet algorithm was also useful in calculating some thermophysical properties, such as temperature, stress, strain, pressure, volume etc. of the materials at any point in time [71, 92].

The effects of edges in 2-D systems such as graphene and surfaces in 3-D systems such as graphite were eliminated in the MD simulations in order to obtain the bulk properties of these systems by simulating an extremely large system to ensure that the surfaces and edges have only a small influence on the properties. However, this approach is computationally expensive. The most efficient way to simulate an indefinitely large system was using periodic boundary conditions (PBC). In PBC, the cubical simulation box was replicated throughout space to form an infinite lattice as shown for a 2-D case in Fig. 3.5. During the simulation, when a molecule moved in the central box, the periodic images in every other box also move in exactly the same way. Thus, as a molecule leaves the central box, one of its images would enter through the opposite face. Therefore the system had no edges [93].

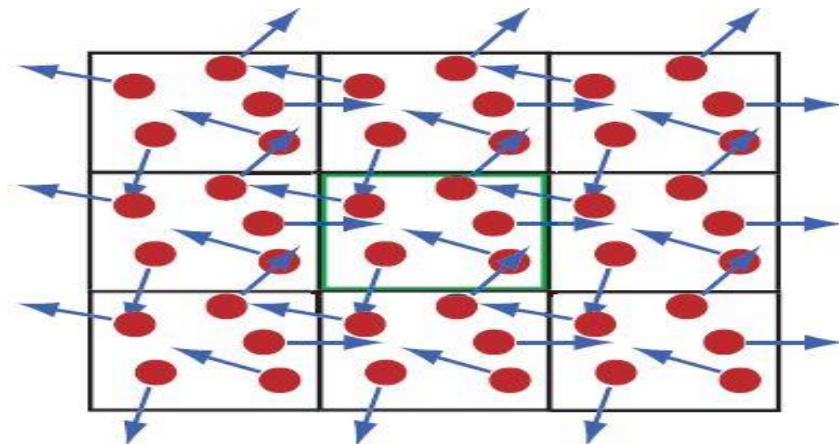
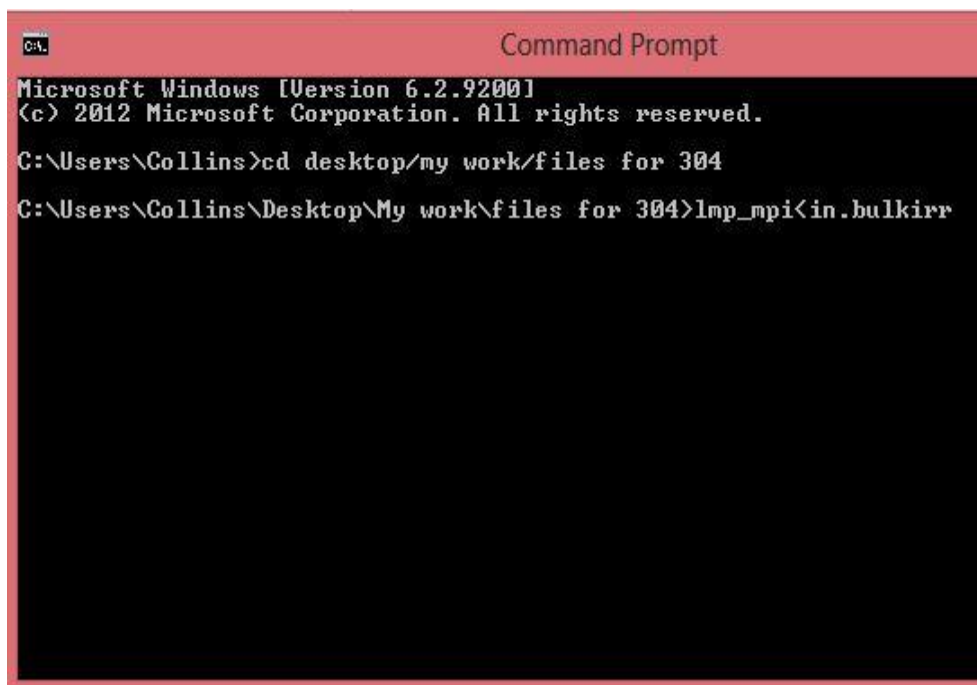


Figure 3.5 Graphical representation of the periodic boundary conditions. The arrows indicate the velocities of atoms. The atoms could interact with atoms in the neighboring boxes without having any boundary effects [93].

The potential on the Fe-Ni-Cr alloys was modified from Bonny G. *et al.* [94] for the research work that is shown in Appendix II.

### 3.3.3 LAMMPS Simulation Algorithm

- A directory was created for the two files: LAMMPS's script file, Potential file; with the executable, `lmp_mpi` (parallel executable type `lmp_mpi.exe`).
- Then the command prompt screen was opened by typing “cmd” in the start menu of the computer.
- In the displaying screen, the default directory was displayed as “C:\Users\name of computer> “. Since the above program files were not in the directly, the path was changed by typing in the screen as “C:\Users\name of the computer> cd directory name: then enter. The desired directory was gotten as “C:\Users\name of the computer\directory name>”. The screen now displayed the same path address as required as seen in Fig. 3.6.



```
Command Prompt
Microsoft Windows [Version 6.2.9200]
(c) 2012 Microsoft Corporation. All rights reserved.

C:\Users\Collins>cd desktop/my work/files for 304
C:\Users\Collins\Desktop\My work\files for 304>lmp_mpi<in.bulkirr
```

Figure 3.6: Command prompt look for LAMMPS Simulation

- The “Path address>mp\_mpi<in.file name” was typed, enter key was pressed and automatically the in.file was then executed by the .exe file and the simulation continued till the output values were displaced, indicating the end of the program as shown in the Fig 3.7.

```

MPI task timings breakdown:
Section : min time : avg time : max time : %varavg : %total
Pair : 236.39 : 236.39 : 236.39 : 0.0 : 93.75
Neigh : 0.40766 : 0.40766 : 0.40766 : 0.0 : 0.16
Comm : 1.023 : 1.023 : 1.023 : 0.0 : 0.41
Output : 7.715 : 7.715 : 7.715 : 0.0 : 3.06
Modify : 6.213 : 6.213 : 6.213 : 0.0 : 2.46
Other : : 0.3961 : : : 0.16

Nlocal: 4000 ave 4000 max 4000 min
Histogram: 1 0 0 0 0 0 0 0 0
Nghost: 7353 ave 7353 max 7353 min
Histogram: 1 0 0 0 0 0 0 0 0
Neighs: 317978 ave 317978 max 317978 min
Histogram: 1 0 0 0 0 0 0 0 0
FullNghs: 635049 ave 635049 max 635049 min
Histogram: 1 0 0 0 0 0 0 0 0

Total # of neighbors = 635049
Ave neighs/atom = 158.762
Neighbor list builds = 27
Dangerous builds = 0
Simulation by Collins Nana Andoh is about to finish
All done
c:\Users\Collins\Desktop\My work\files for 304\200 Degree>

```

Figure 3.7: On screen view of Output values from Simulation

### 3.3.4 Implementation of LAMMPS Simulation

To get a reliable results from the modified potential file, an initial simulations was performed to determine the equilibrium lattice constant and cohesive energy of the Fe-Ni-Cr alloys, and the values compared with published data in order to verify the interatomic potential adapted [80] for the main bulk properties calculations proven.

The MD simulation with LAMMPS were conducted by the procedures;

- A simulation cell with Face Centered Cubic (FCC) atoms with (100) orientations in the x, y, and z directions was generated as in Fig. 3.8 with a simulation cell size of 10 lattice units in each directions ( $10 \times 10 \times 10 \text{ \AA}$ ) to ensure the simulation converged.

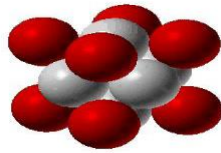


Fig 3.8 (a)

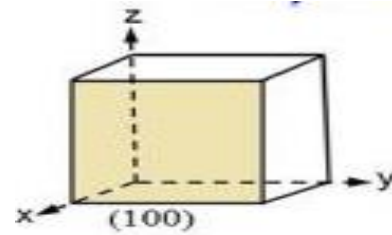


Fig 3.8 (b)

Fig 3.8: (a) Crystal structure of an FCC lattice (b)  $\langle 100 \rangle$  orientation in the x, y and z direction where the uniaxial deformation will be applied (Courtesy: P.M. Anderson, [95]).

- The equilibration step was conducted at a temperature 300 K (Ambient temperature) with a pressure of 1 atm (0.01 MPa) at each simulation cell boundary terminating after 12000 simulations at a time step of 0.002 ps.
- The simulation cell was then subjected to uniaxial tensile deformation in the x-direction under controlled temperature at a strain rate of  $5 \times 10^{10}$  1/s, while the lateral boundaries were controlled using the NPT (constant Number of Atoms, Pressure and Temperature ensembles) equation of motion at 25 MPa pressure.
- The dump file that included the x, y, and z coordinates, the centrosymmetry values, the potential energies, and forces for each atom were outputted by the program as it runs for direct visualization by VMD.
- The stress and strain values were also outputted into a separate file named Fe.Deform for the extraction of the mechanical properties of the materials.
- The Simulation was terminated after 20000 iterations at time step of 0.002 ps.
- The simulation was then repeated for temperatures of 573 K, 673 K, and 773 K (300 °C, 400 °C and 500 °C respectively) for each Fe-Ni-Cr alloy (304, 308, 309, 316) evaluated.

### 3.3.5 Output of LAMMPS Simulation

After successful running the in.file, the three out-put files obtained were:

- Dump files (contained the atomic co-ordinates of the final structure after simulation, and data on deformation for VMD visualization of deformation processes, see Appendix VI)
- Fe.deform (contained the stress component values as well as the corresponding strain values to determine the bulk modulus, see Appendix VI).
- Log.lammps file (contained thermo-physical data of temperature, pressure, volume and total energy after a particular number of simulation steps, see Appendix VI).

Copies of the last two output files are shown in the Appendix II and the structures at various time steps, the final structure after simulation and the first output file that contained the atomic co-ordinates were visualized and animated with VMD code.

### 3.3.6 Visualization of Simulation Output by VMD and MATLAB

The atomic structures in the Dump file output file from the LAMMPS simulation were viewed in VMD, following the steps;

- VMD program was opened;
- The Dump file containing the atomic coordinates of the Fe-Ni-Cr alloy was then imported through the VMD Main window;
- Adjustments and changes were made to the colour and display format (perspective) of final structure
- The final output was then saved in JPEG Picture format.

The algorithm for animation of the tensile deformation can be seen at Appendix III.

The mechanical properties - ultimate tensile strength, yield strength, breaking point strength, and Young's Modulus of Fe-Ni-Cr alloys were extracted through MATLAB import terminal. The steps were:

- MATLAB program was opened;
- At the command window the import button was then pressed;
- The output files Fe.deform were then imported into MATLAB
- The imported data was analysed and then plotted to give the required graphs
- The graphs were then saved in JPEG (Picture format) form.

## CHAPTER FOUR: RESULTS AND DISCUSSIONS

The Chapter is divided into three main Sections. Section 4.1 consists of results obtained from the irradiation assessment, Section 4.2, the evaluation of the mechanical integrity while the Section 4.3 gives the general discussions of the research findings. Typical output data for SS304 would be presented under the results section, and the other results be provided in Appendix IV while the comparison results will be in tabular form and that will be placed at Appendix V. Thermal neutron irradiation damage were compared with fast neutron damage.

### 4.1 THERMAL AND FAST NEUTRON IRRADIATION DAMAGE IN SS304

#### 4.1.1 Collision Cascade

The SRIM-TRIM output window of the collision events of the thermal spectrum compared with the fast spectrum are shown in Fig. 4.1 (a) and (b) both illustrating at the Calculation Parameters window the resulting calculations of Vacancies/ Ion, Longitudinal range or depth of penetration, Percentage Energy Loss and then Sputtering Yield of the SS304.

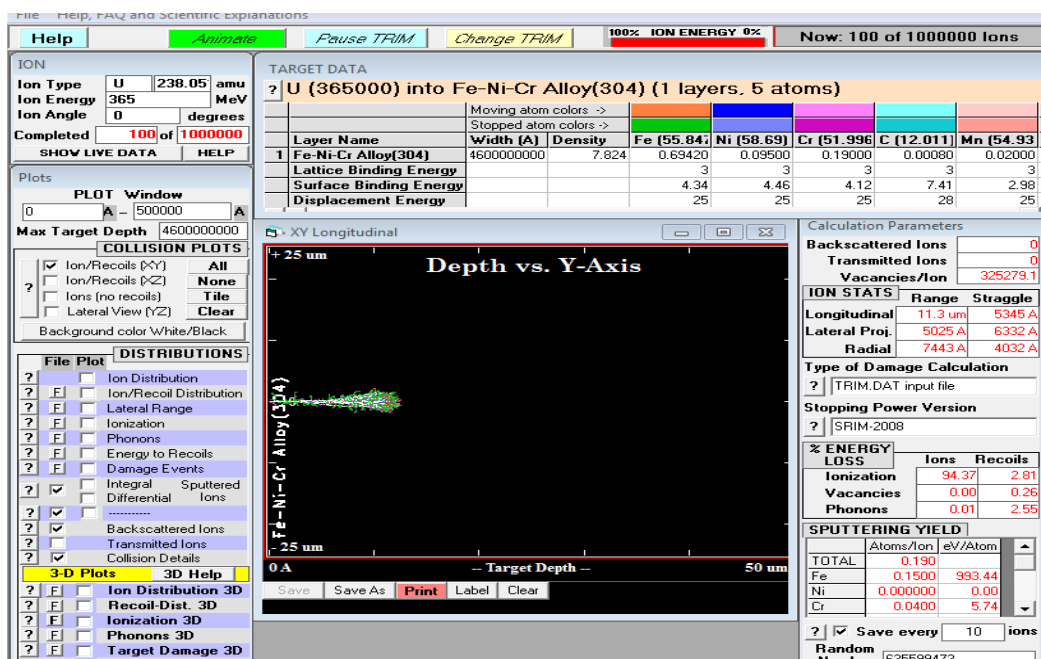


Fig 4.1 (a)



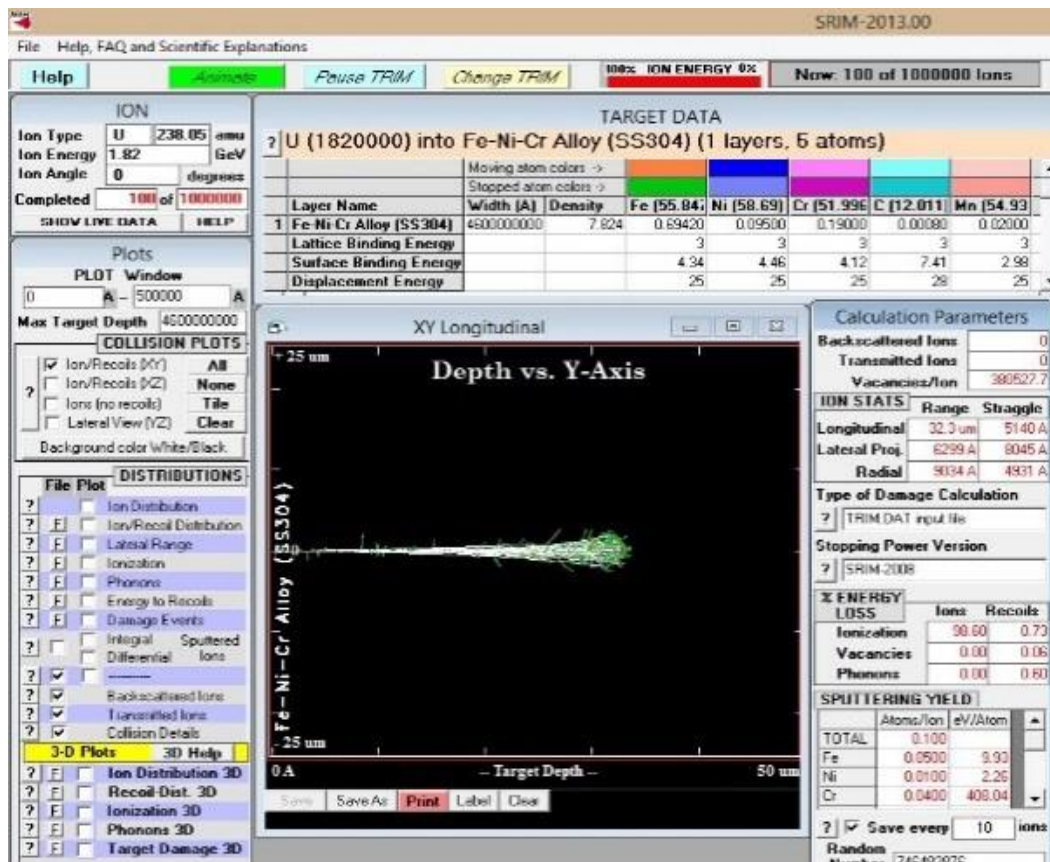


Fig 4.1(b)

Fig 4.1: Collision Cascade window for (a) thermal and (b) fast neutron irradiation damage in Fe-Ni-Cr alloy SS304

#### 4.1.2 Projected Ion Range Distribution

The output plots of the longitudinal range are shown in Fig. 4.2 illustrating the depth of penetration of both the thermal and fast neutron into the Fe-Ni-Cr alloy SS304. The thermal neutrons penetrated to 11.3  $\mu\text{m}$  as compared with 32.3  $\mu\text{m}$  in the fast spectrum. The penetrating depth in the fast neutron spectrum was about three times greater than in the thermal spectrum. Hence material for the fast spectrum design must be of larger thickness. Nonetheless, comparing their depth with the thickness of  $4.6 \times 10^5 \mu\text{m}$  indicates insignificant penetration and possible minimal damage.

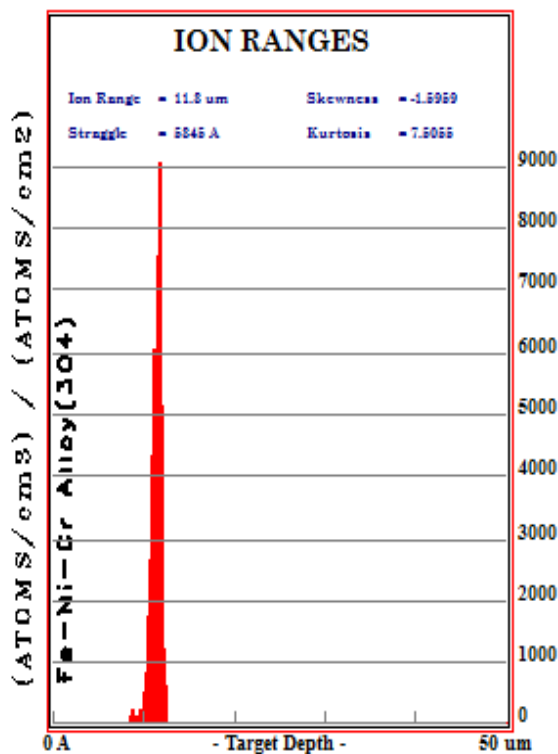


Fig 4.2 (a)

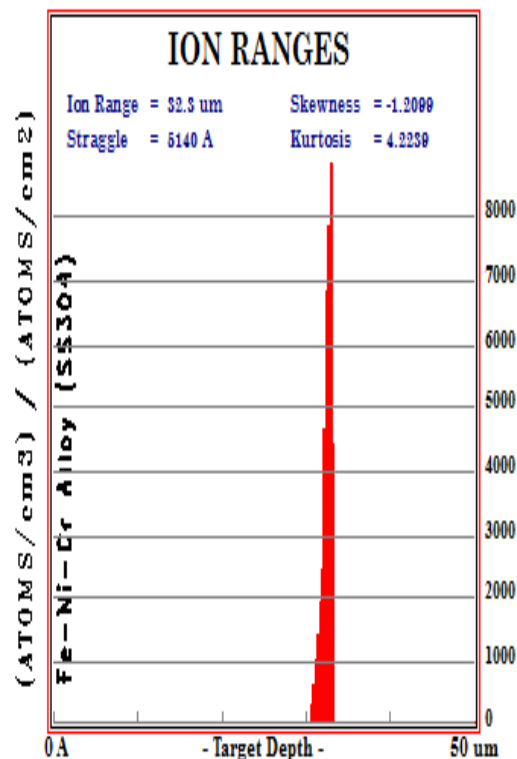


Fig 4.2 (b)

**Fig 4.2:** Projected Range of (a) thermal and (b) fast neutrons in the Fe-Ni-Cr Alloy SS304

#### 4.1.3 Lateral Ion Range Distribution

The average final y-z displacement of the ions assuming a perpendicular incidence of the ion beam for both the thermal spectrum and fast spectrum are shown in Fig. 4.3 (a) and (b) respectively. It can be seen that the ions had a wider lateral distribution (spreading) in the thermal neutron spectrum than the fast neutron spectrum implying that increase in incident ions energy decreases the lateral range and rather increase the projected range or penetration power as shown in Fig 4.2(a) and (b). Hence the materials to be used in the thermal spectrum should be wide enough to curtail any penetration in the y-z direction.

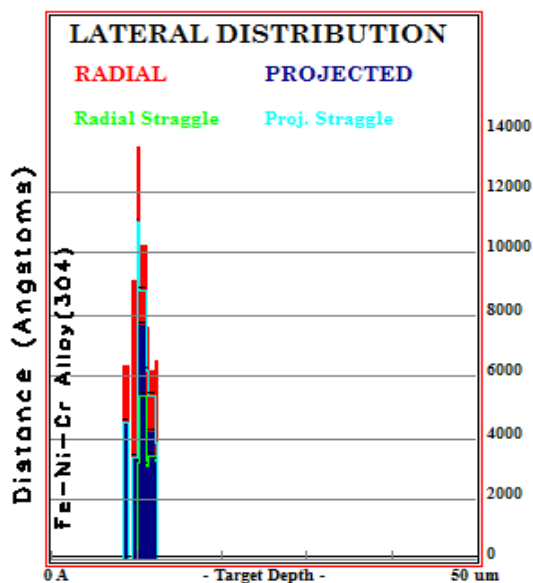


Fig 4.3 (a)

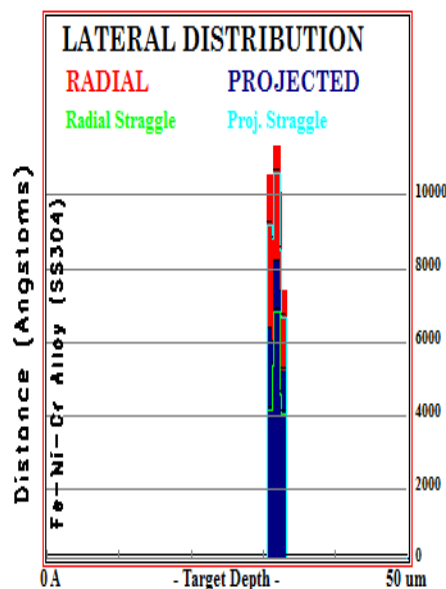


Fig 4.3(b)

Fig 4.3: The lateral Range distribution of the (a) thermal and (b) fast neutron ions in the Fe-Ni-Cr Alloy SS304

#### 4.1.4 Ionization Energy Distribution

Figures 4.4 (a), (b), (c) and (d) show the energy neutrons lost to the Fe-Ni-Cr Alloy target electrons in 2D ( Fig 4.4(a) and (b)) and 3D Fig 4.4(c) and (d)) views. At the very bottom of the two plots are the tiny ionization contributions from the recoils (that blue line), implying that the bulk of the energy dissipated to the Fe-Ni-Cr Alloy SS304 electrons was from the Ions (red). The percentage of energy loss in Ionization in the simulation as shown in Fig 4.1 (a) and (b) at “% Energy Loss” was 97.18 % (355 MeV – comprising of 94.37 % from Ions and 2.81 % from recoil atoms) in the thermal spectrum as compared with 99.33 % (1808 MeV – also comprising of 98.49 % from Ions and 0.45 % from recoil atoms) of the fast spectrum. The above result implies that more heat would be produced in the latter than the thermal spectrum. This means that should the SS304 be used for the fast neutron spectrum design, irradiation induced mechanical deterioration through diffusion of

point defects as a result of ionization would be massive and hence much attention would be needed.

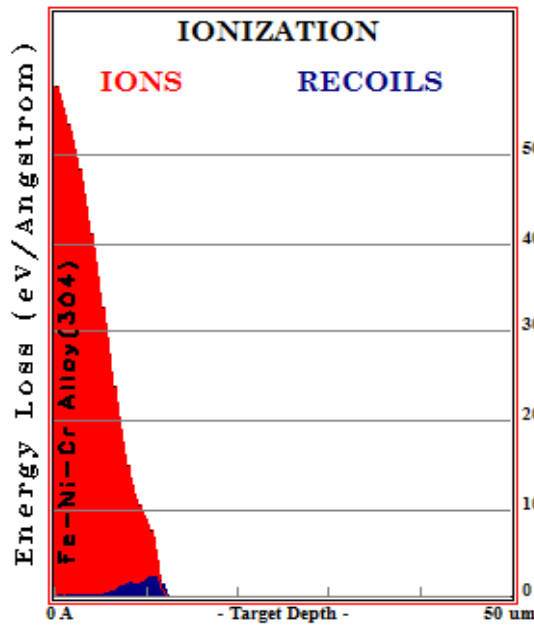


Fig 4.4 (a)

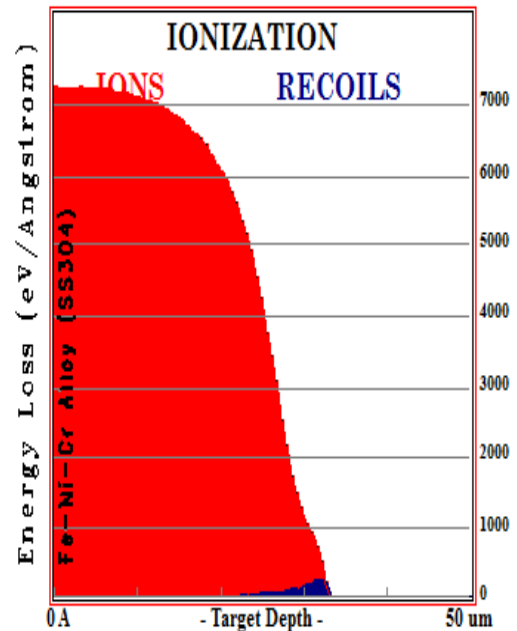


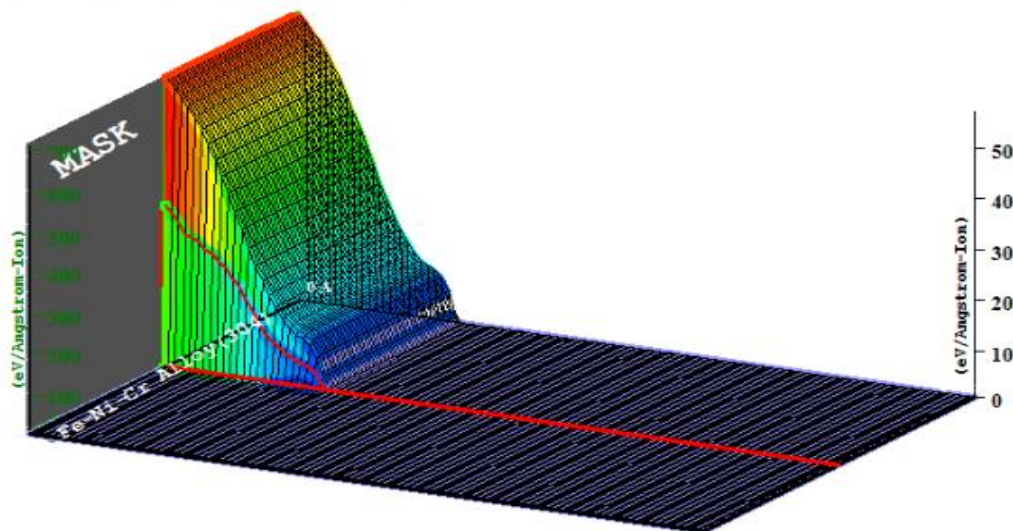
Fig 4.4(b)

### Target Ionization

Total Ionization = 354684.3 keV / Ion

Total Phonons = 9340.3 keV / Ion

Total Target Damage = 975.47 keV / Ion



Plot Window goes from 0 A to 50 um; cell width = 5000 A  
Press PAUSE TRIM to speed plots. Rotate plot with Mouse.

**Ion = U (365. MeV)**

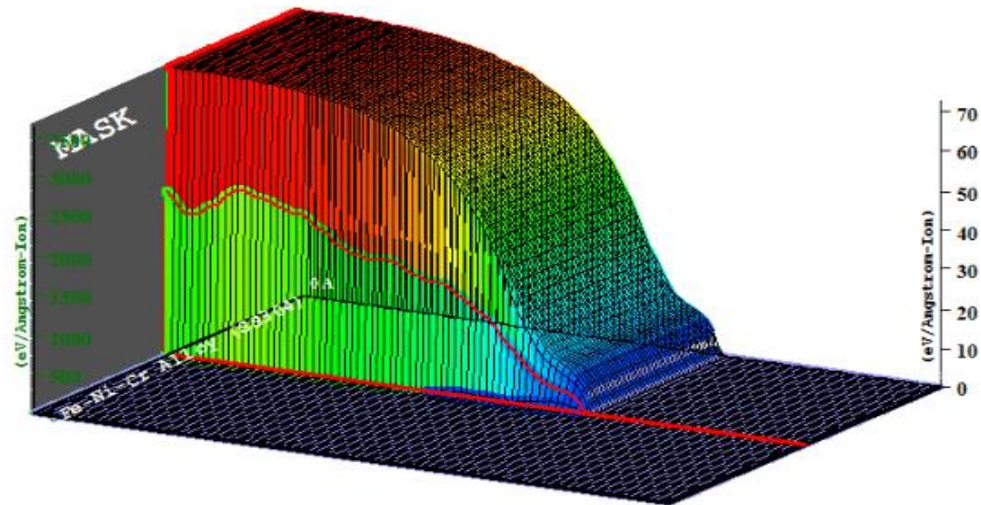
Fig 4.4 (c)

## Target Ionization

Total Ionization = 1807893.2 keV / Ion

Total Phonons = 10965.3 keV / Ion

Total Target Damage = 1141.47 keV / Ion



Plot Window goes from 0 A to 50 um; cell width = 5000 A  
Press PAUSE TRIM to speed plots. Rotate plot with Mouse.

**Ion = U (1820. MeV)**

Fig: 4.4 (d)

Fig 4.4: 2D view of the Ionization energy distribution of (a) thermal neutrons as compared with the (b) fast neutrons (c) and (d) 3D view of the Ionization energy distribution in the Fe-Ni-Cr alloy SS304

### 4.1.5 Phonons

From Fig 4.1 (a) and (b) in section 4.1.1, the “% Energy Loss” pane shows that 2.56 % (0.975 MeV – comprising 0.01 % of the Ions and 2.55 % of the recoil atoms) of the energy was loss in a form of phonons in the thermal spectrum as compared with only 0.06 % (1097 MeV) in the fast spectrum which was only from the recoil atoms. It could also be seen in Fig. 4.5 (a) that due to the low energy of the incident ions, there was a thorough interaction with the Target material and hence a higher percentage of the energy was loss as a result of the vibration unlike in the case of the Fig 4.5 (b) where the ion penetrated deeper with little interaction.

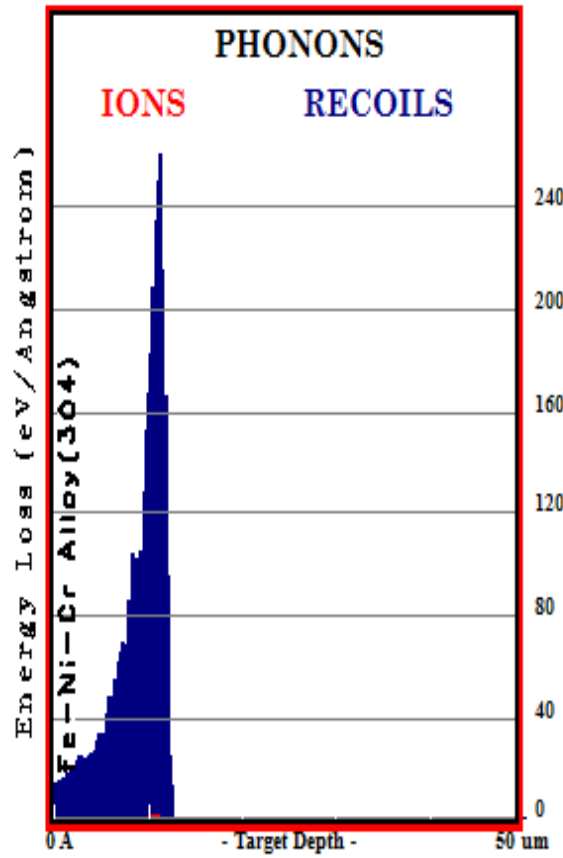


Fig 4.5 (a)

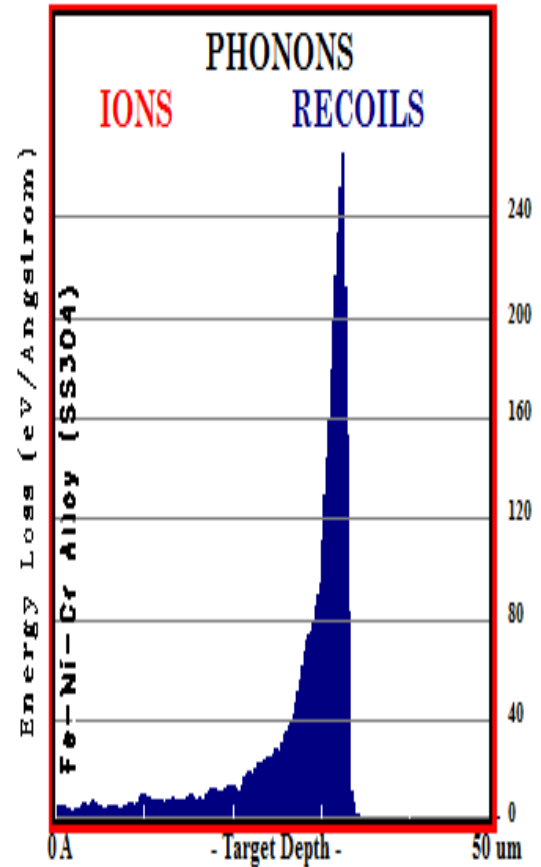


Fig 4.5(b)

Fig 4.5: Distribution of (a) thermal and (b) fast neutrons energy loss to Fe-Ni-Cr Alloy SS304 phonons

#### 4.1.6 Ion's Energy to Recoil Distributions

The energy absorbed by the component elements Fe, Ni, Cr, and C in the case of the Fe-Ni-Cr alloy SS304 is shown in Fig 4.6 (a) and (b). It could be seen that the higher the percentage of the component element, the higher the absorption.



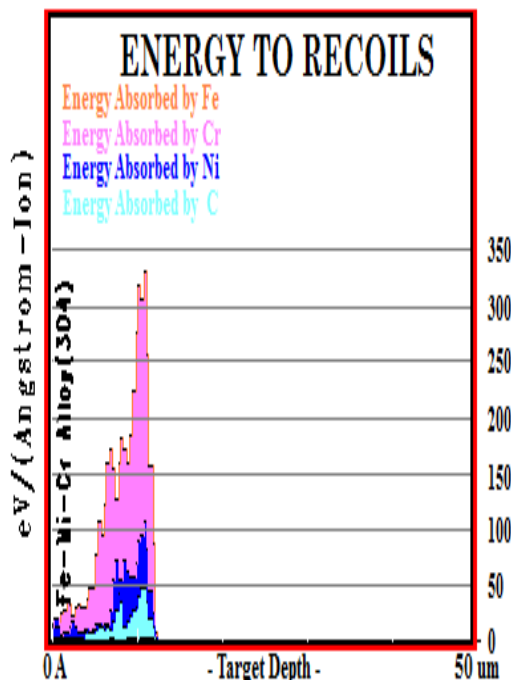


Fig 4.6 (c)

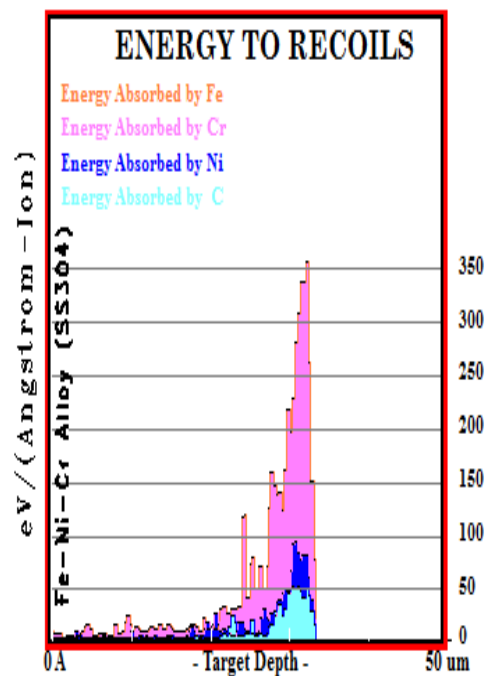


Fig. 4.6 (d)

Figure 4.6: Distribution of energy absorbed by the SS304 Fe-Ni-Cr Alloys elements from (a) the thermal and (b) fast neutrons spectrum

#### 4.1.7 Collision Events

Since the kinetic energies in the cascades were very high, the material was driven locally far outside its thermodynamic equilibrium. This led to the production of point defects such as vacancies in the materials. Though the material was subjected to different energy levels in the two proposed spectrum it was realized that the rate of vacancy production were the same. Thus in the thermal neutron spectrum (Fig 4.7 (a) and (c)), the total target displacement was averagely 337242/Ion and out of that, 325279 representing 96.5 % remained as vacancies. Similarly, out of the total target displacement of 394519/Ion in the fast neutron spectrum (Fig 4.7 (b) and (d)), 380528 (96.5 %) were left as vacancies. This therefore implies that the Collision event may not be a good tool to use in assessing the damage of a particular material used in different neutron spectrum.

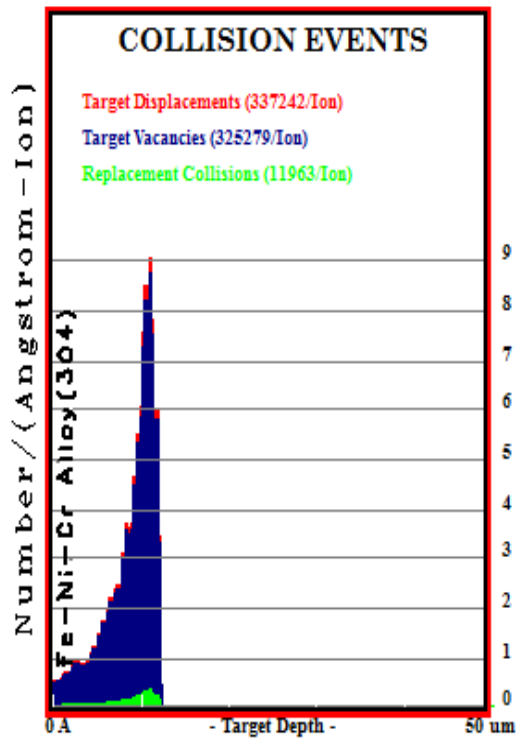


Fig 4.7 (a)

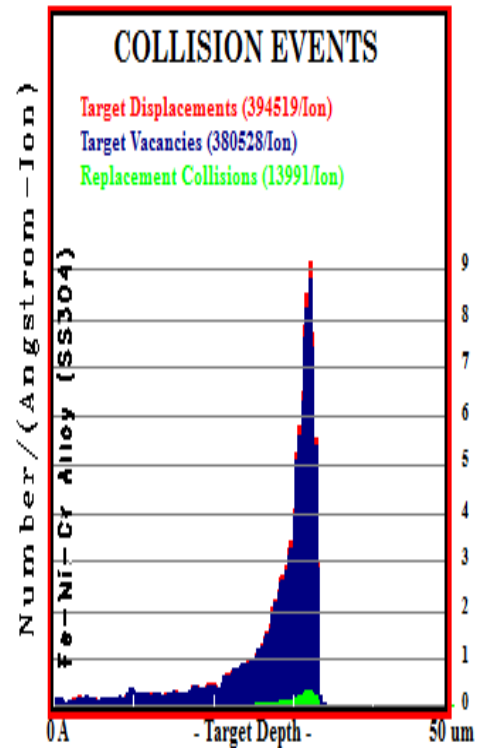


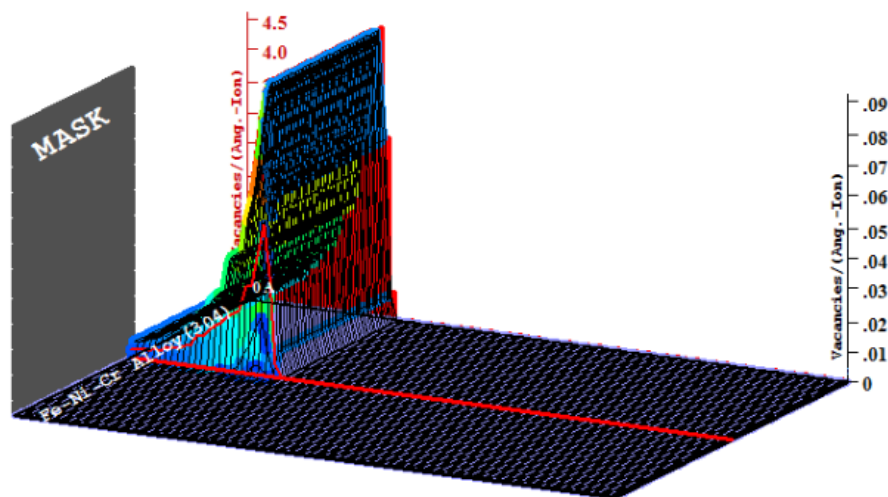
Fig 4.7 (b)

### Target Vacancies

Total Displacements = 337242 / Ion

Total Vacancies = 325279 / Ion

Replacement Collisions = 11963 / Ion



Plot Window goes from 0 A to 50 um; cell width = 5000 A  
Press PAUSE TRIM to speed plots. Rotate plot with Mouse.

**Ion = U (365. MeV)**

Fig 4.7 (c)

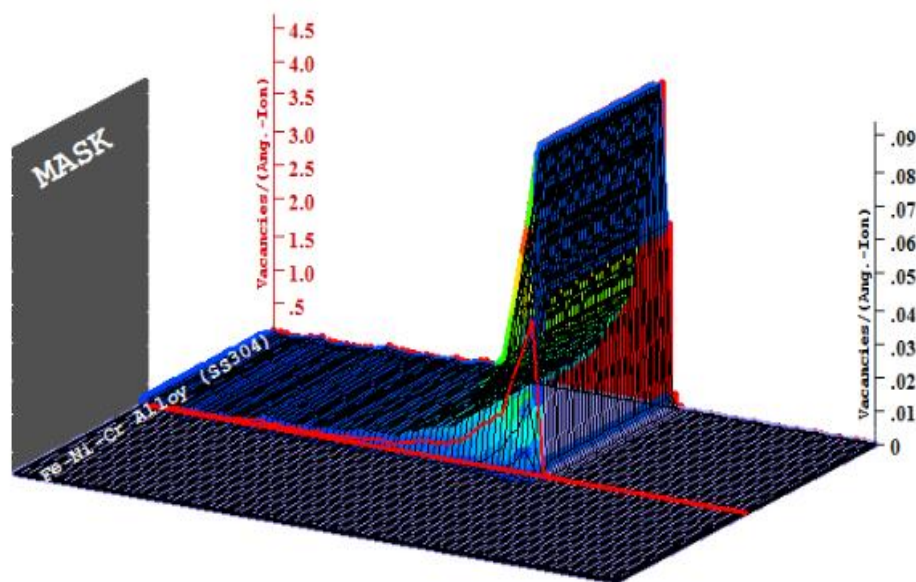


## Target Vacancies

Total Displacements = 394519 / Ion

Total Vacancies = 380528 / Ion

Replacement Collisions = 13991 / Ion



Plot Window goes from 0 Å to 50  $\mu\text{m}$ ; cell width = 5000 Å  
Press PAUSE TRIM to speed plots. Rotate plot with Mouse.

**Ion = U (1820. MeV)**

**Fig 4.7 (d)**

Figure 4.7: 2D view of the collision events of (a) thermal and (b) fast neutron spectrum, (c) and (d) gives the 3D view of the collision events

### 4.1.8 Sputtering Target Atoms

Fig. 4.8(a) and (b) shows the integral sputtering for the thermal and fast neutron spectrum respectively. This plot shows the number of elemental atoms reaching the target surface that did not have enough energy to escape. It could be seen that the Fe components sputtered much, followed by the Cr, then Mn and Ni. This therefore implies that sputtering does not depend on the percentage of the elements. Also while in the thermal spectrum about 0.1 atoms of the Fe were sputtered per Ion, only 0.05 atoms were sputtered per ion.

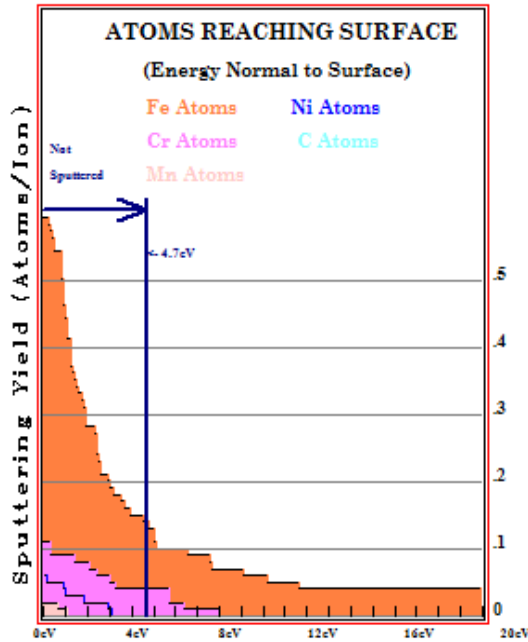


Fig 4.8 (a)

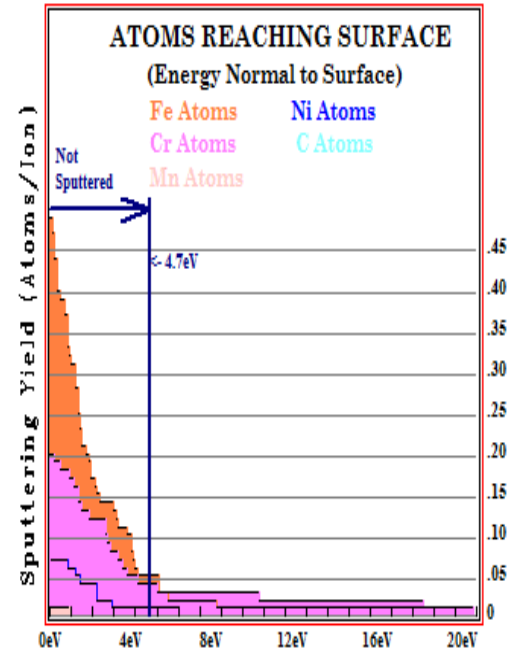


Fig 4.8 (b)

Figure 4.8: Distribution of the integral sputtering yield of Fe-Ni-Cr Alloy SS304 in (a) thermal and (b) fast neutron spectrum

The output results obtained on the irradiation damage assessment of the other three Fe-Ni-Cr alloys 308, 309 and 316 are displayed at Appendix IV and Comparison of the irradiation damage of all Fe-Ni-Cr alloys under thermal and fast neutron spectrum of the SCWR are also shown in Appendix V.

## 4.2 EVALUATION OF MECHANICAL DETERIORATION OF THE Fe-Ni-Cr ALLOYS

### 4.2.1 Cohesion Energy of the Fe-Ni-Cr Potential File

The results of LAMMPS cohesive energy  $E_{\text{cohe}}$ , and equilibrium lattice constant,  $a$  simulation for the FCC FeNiCr.eam.alloy potential are as shown in Table 4.1 compared with their experimental values.

Table 4.1: Summary of Equilibrium Lattice Constant and Cohesive Energy from the simulation compared with theoretical values.

	LAMMPS	Expt. Data	$\Delta/\%$
<b>Equilibrium Lattice Constant /Å</b>	3.489	3.499 [94]	1.0
<b>Cohesive Energy / eV/atom</b>	-4.117	-4.120 [94]	0.3

#### 4.2.2. VMD output for Tensile Deformation

The detailed VMD output files for the tensile deformation are shown in Figure 4.9, representing the snapshots of the simulation at 8 picosecond intervals.

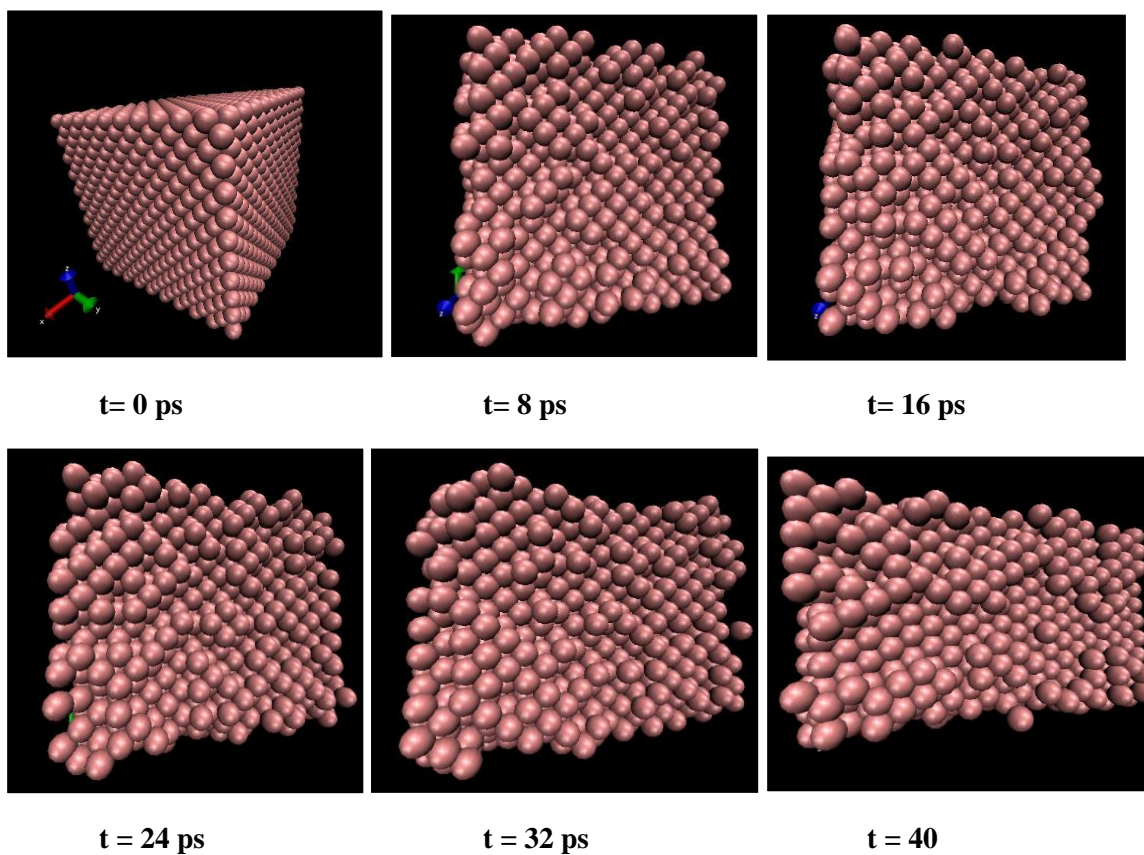


Fig: 4.9: VMD Snapshot showing Fe-Ni-Cr alloy model of size 10 Å x 10 Å x 10 Å (No. of atoms 4000)

#### 4.2.2 Stress-Strain Plots at Ambient and Supercritical Water Conditions

Figure 4.10 presents the stress- Strain curve to failure showing Young's Modulus, UTS, and Breaking Strength of SS304 alloy under ambient conditions (23 °C, 1 atm). It shows the Young's Modulus, the Ultimate Tensile Strength, the Breaking Strength (Fracture) and their corresponding strain values. The same approach was used in extracting the mechanical properties of the other alloys under investigation at Ambient and Supercritical Water Cooled Condition shown in Appendix VII and Figure 4.11 (a) through to Figure 4.11(d).

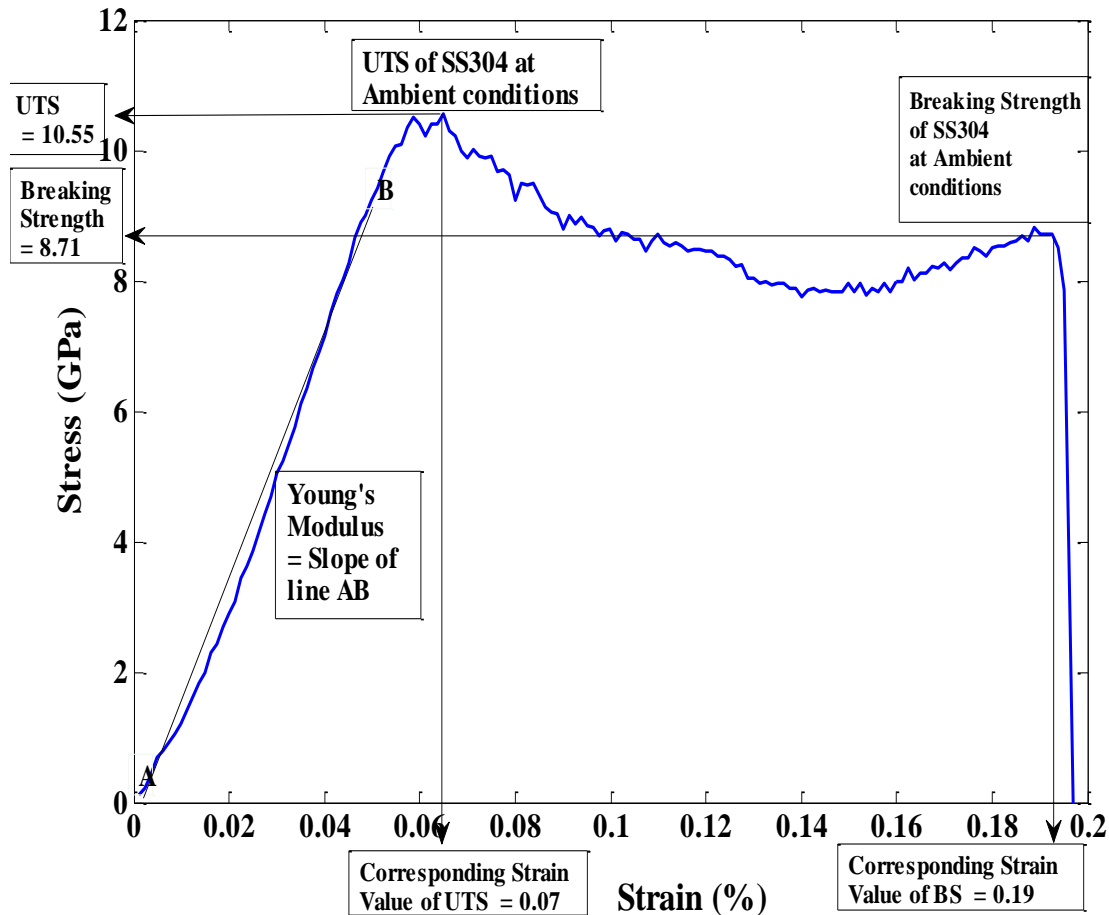


Fig 4.10: Stress- Strain curve to failure showing Young's Modulus, UTS, and Breaking Strength of SS 304 alloy under Ambient Conditions

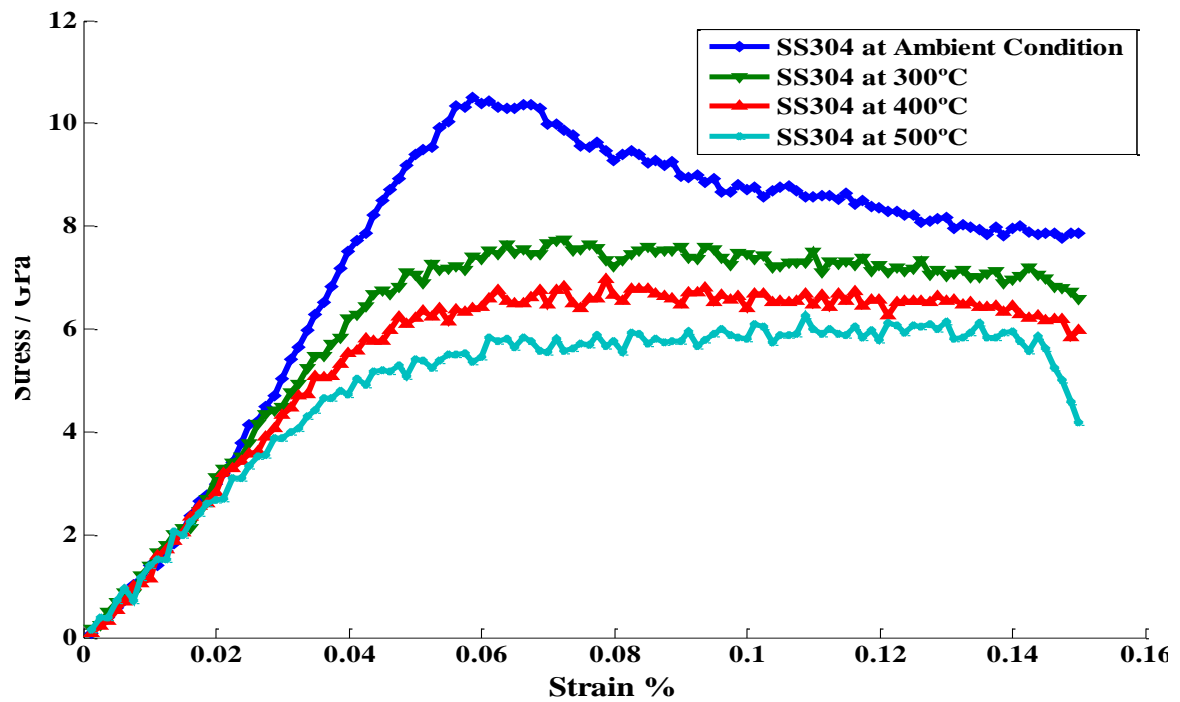


Fig 4.11 (a) (SS304)

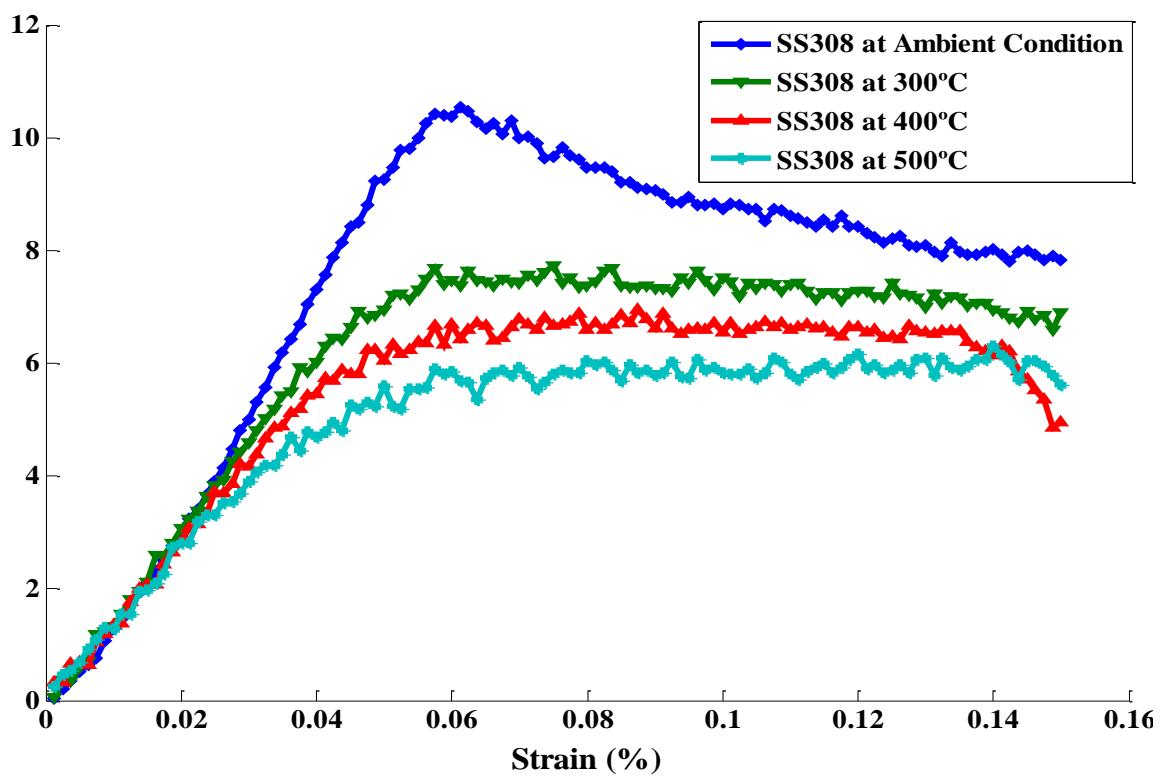


Fig 4.10 (b) (SS308)

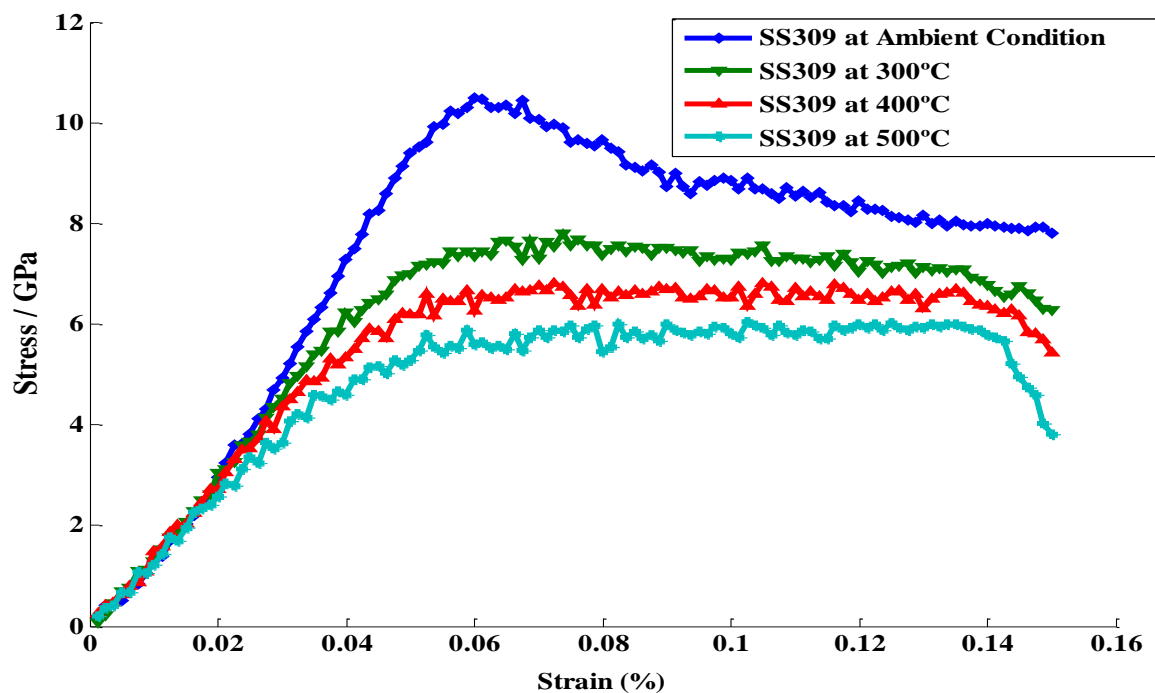


Fig 4.11 (c) (SS309)

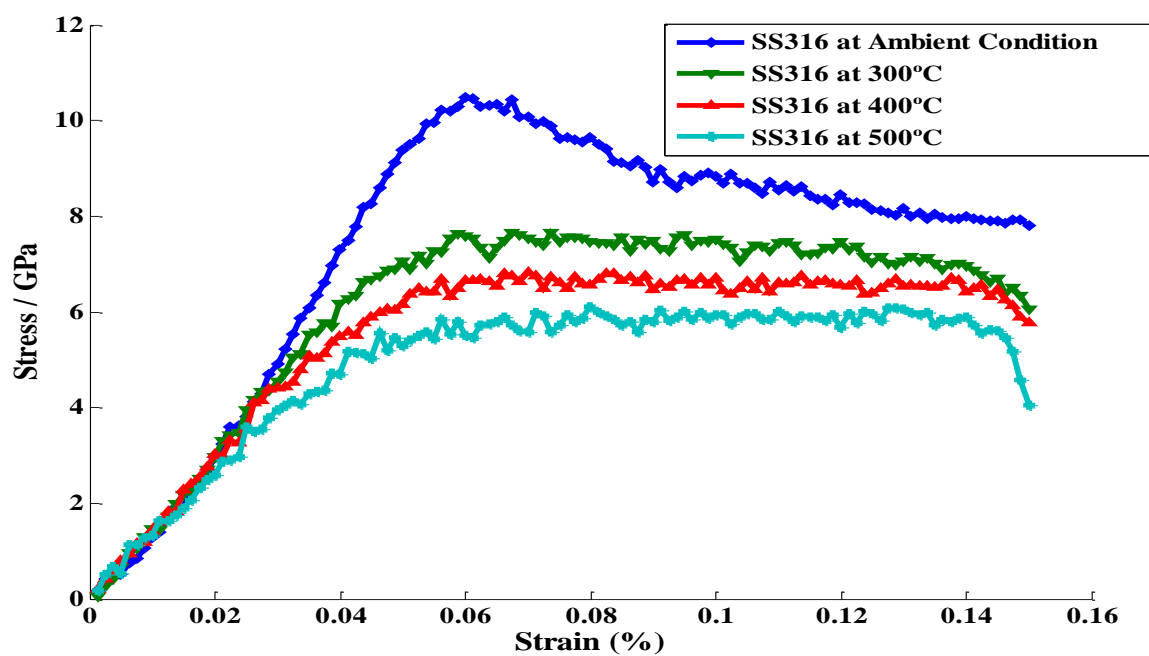


Fig 4.11 (d) (SS316)

Figure 4.11: Stress-Strain plots for (a) SS304 (b) SS308 c) SS309 and d) SS316 alloys at ambient condition and Supercritical Water Condition at strain rate of  $5 \times 10^{10} \text{ s}^{-1}$

### 4.2.3 Mechanical Properties of Fe-Ni-Cr Alloys

The mechanical properties of the Fe-Ni-Cr alloys extracted from the Stress-Strain curves of Fig. 4.11 are shown in Fig 4.12. Figures. 4.12(a), 4.12(b), 4.12(c) and 4.12(d) respectively show the variation of Young's Modulus, Yield Strength, Ultimate Tensile Strength and the Breaking Strength with different temperature and pressure(treatment conditions). It could be seen that all the four plots above show similar trend. The mechanical properties decreased with increasing temperature and pressure. Though the materials had similar mechanical strength at the Ambient condition, Fe-Ni-Cr alloy SS304 was found to be deformed least while SS309 was realized to be deformed the most.

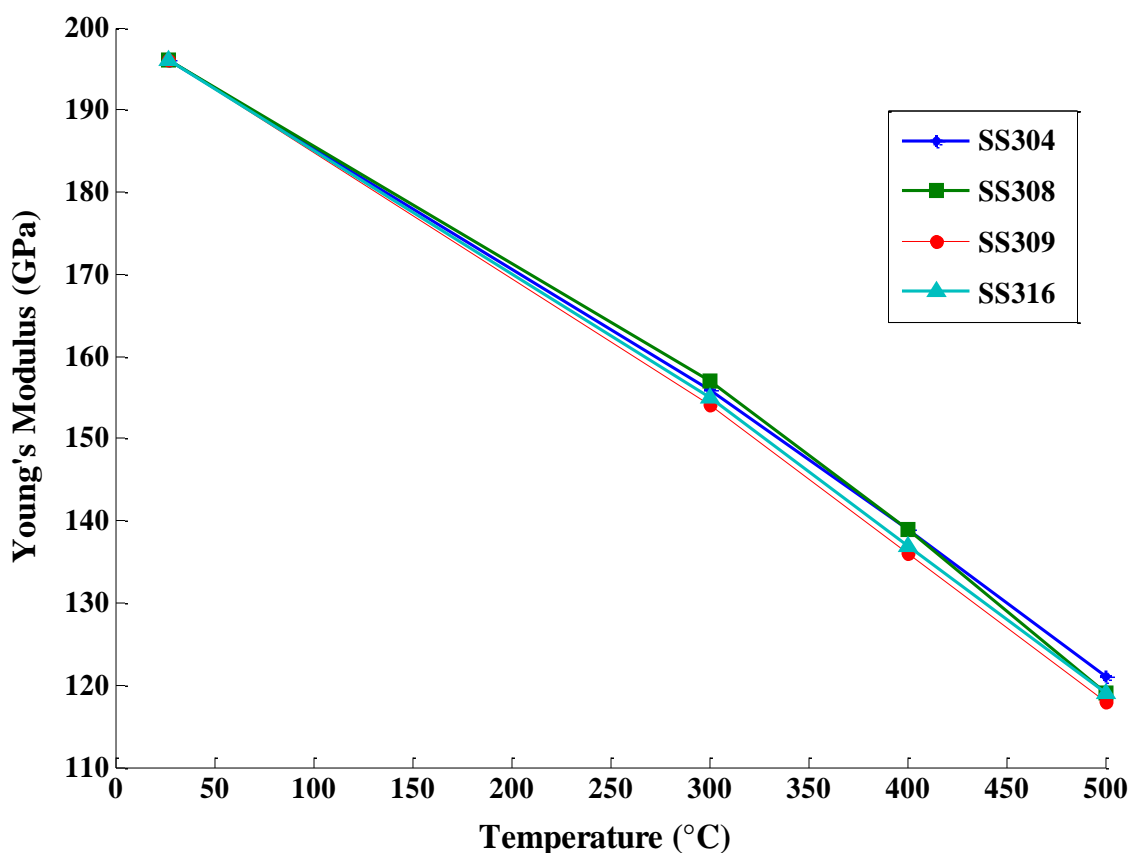


Fig 4.12(a)

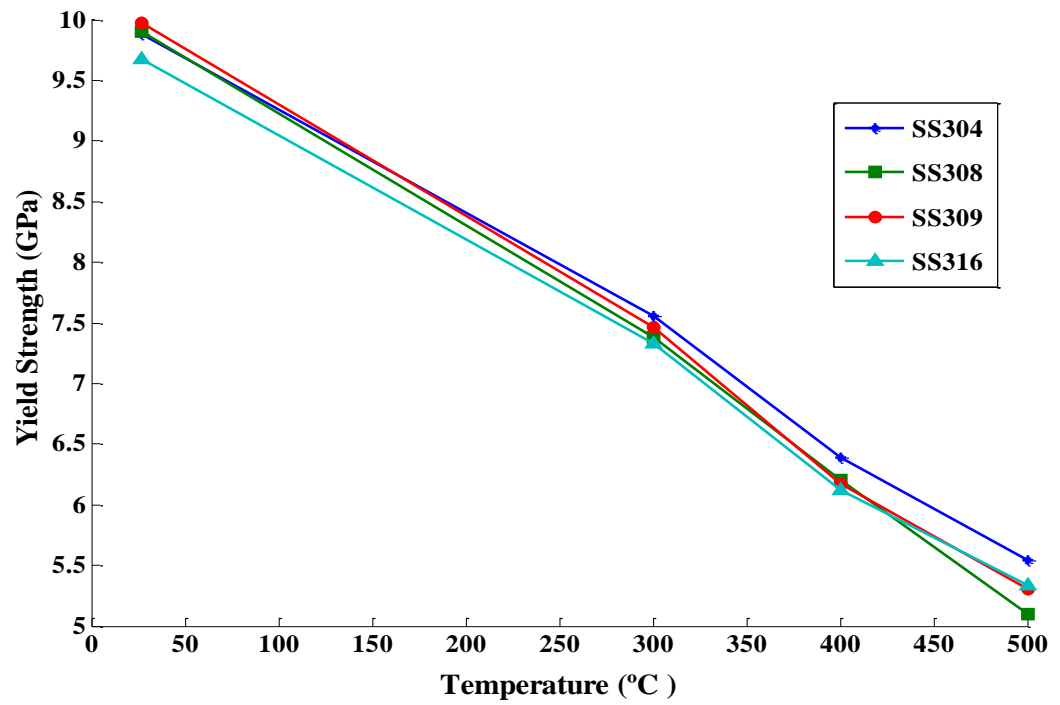


Fig 4.12(b)

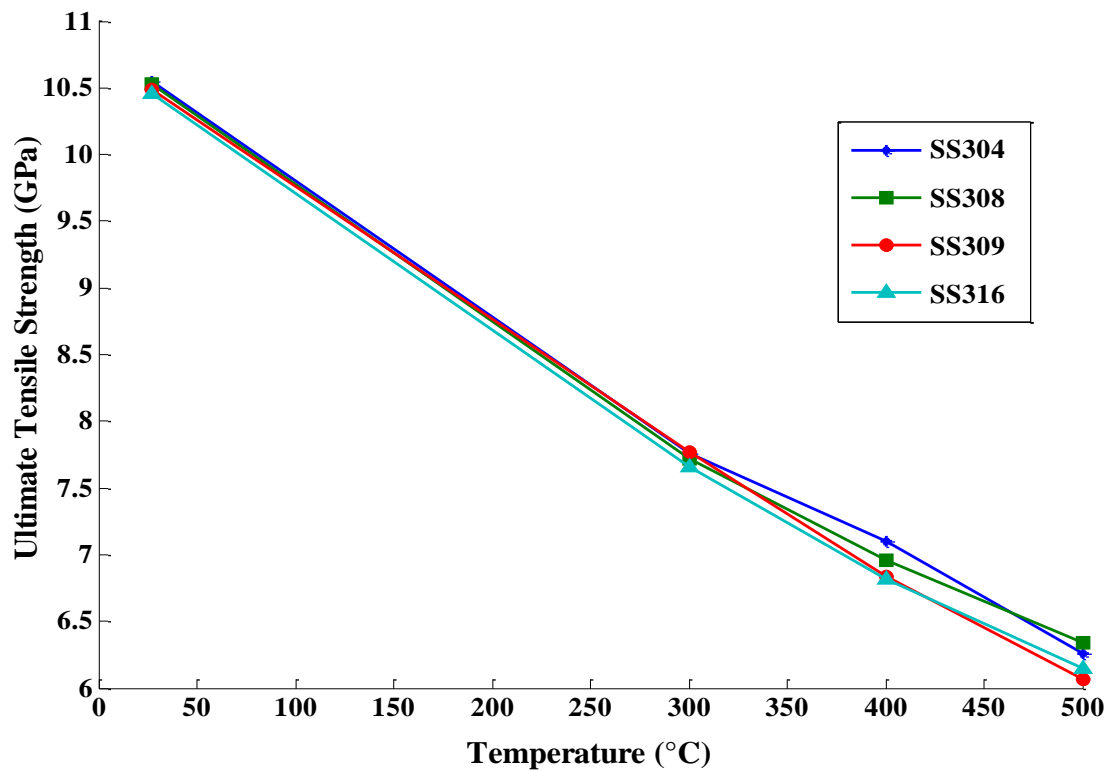


Fig 4.12(c)



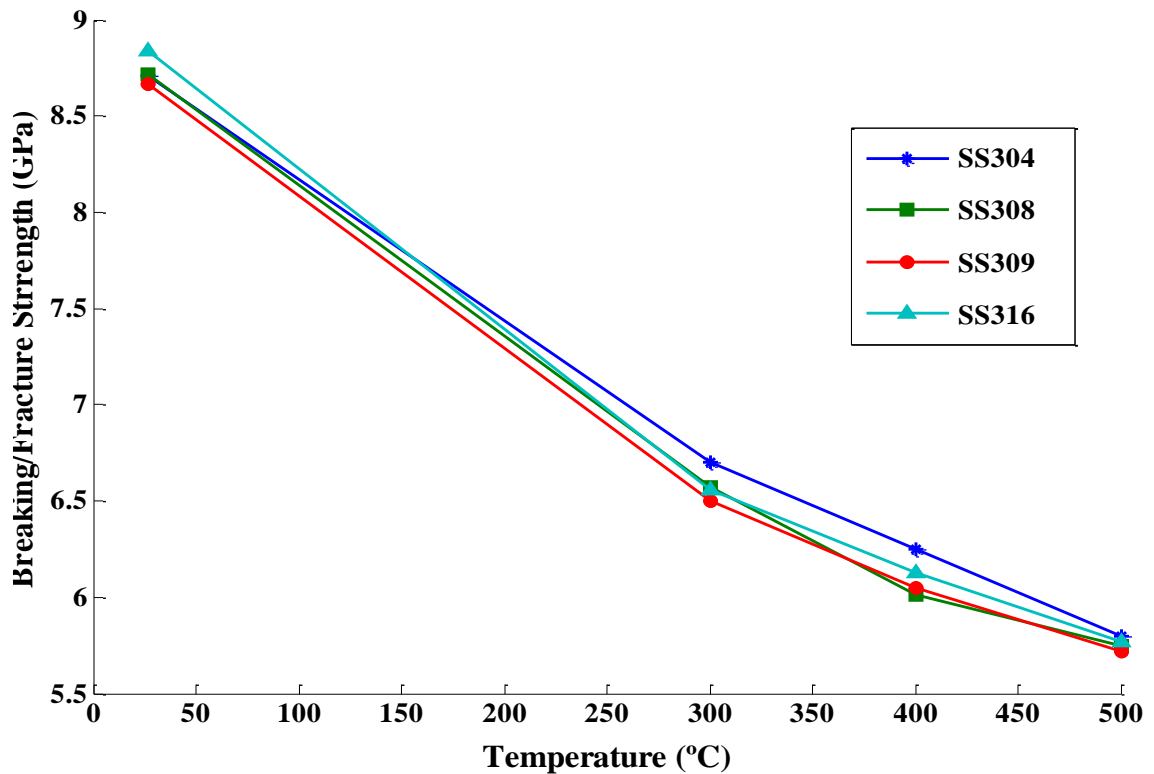


Fig 4.12(d)

Fig 4.12: Variation of (a) Young's Modulus (b) Yield Strength (c) Ultimate Tensile Strength and (d) Breaking or Fracture Strength and of the alloys with respect to ambient and SCW condition.

### 4.3 DISCUSSIONS

#### 4.3.1 General Discussions

In general, neutron irradiation damage and mechanical deterioration of materials are two of the most prevalent reactor structural material challenges in general. Hence in the process of identifying suitable structural materials for the proposed Supercritical Water-Cooled Reactor (SCWR), it was necessary to take candidate materials through these tests.

Based on available knowledge on the Fe-Ni-Cr alloys usage in LWR and fossil fueled boilers and with the assumption that SCWR operation will be based on the two

technologies [6], Fe-Ni-Cr alloys SS304, SS308, SS309 and SS316 were selected. These materials were assessed for their susceptibility to neutron irradiation and mechanical strength using the SRIM – TRIM code and LAMMPS code. Since the reactor core may have a predominantly thermal or fast neutron spectrum depending upon the specific core design [3, 6], the materials were assessed based on the thermal and fast neutron spectrum.

The neutron irradiation assessment in Section 4.1, Appendix III and Appendix V showed that both thermal and the fast neutron caused defects in the alloys. It was realized that due to the high neutron energy in the case of the fast neutron spectrum, it will experience high penetration. This high penetration (infer from Figure 4.2) which led to high energy transfer to the Fe-Ni-Cr target electrons (infer from Figure 4.4) which was dissipated later in a form of heat energy. Also due to the high penetration power in the fast spectrum, the collision cascade was located deeper under the surface of the target resulting in low sputtering yield (infer from Fig 4.8). The closer a collision is to the surface, the higher the energy transferred from the collision cascade to the surface or near surface atom and hence the higher the sputtering. Therefore the fast neutron spectrum had low sputtering yield as compared to the thermal and as such will lead to high heat energy dissipation.

The comparative studies of the irradiation damage of the Fe-Ni-Cr alloys under thermal neutron spectrum of the SCWR in Appendix VII revealed that SS308 as well as SS304 were least damaged by the radiation.

The mechanical parameters extracted from the LAMMPS simulation, Figure 4.11 and Figure 4.12, confirmed the results from the irradiation damage assessment since SS304 as well as SS308 had slightly higher mechanical strength than the other two. Thus, as shown in Figure 4.12, and in Appendix VII, the rate of decrease in the mechanical parameters studied was slower in these two materials than the other two.

### **4.3.2 Discussion on Neutron Irradiation Damage**

#### **4.3.2.1 Projected Range**

The distance measured along the incident ion trajectory at which the highest concentration of incident ions are as shown in Appendix V were found to be same, 11.3  $\mu\text{m}$ , except SS309 which experienced 11.4  $\mu\text{m}$  in thermal neutron spectrum. Also when the materials were exposed to radiation in the fast spectrum SS308 recorded a depth of 32.4  $\mu\text{m}$  while the rest experienced penetration depth of 32.3  $\mu\text{m}$ . Although there was a variation in the penetration depth, there was invariably no significant difference in the values.

The results also revealed that the depth of penetration in the fast neutron spectrum would be thrice that of the thermal and as such much attention should be given to the design of the SCWR should the fast spectrum be considered.

The values seem insignificant since the structural materials are most often in order of millimetres but continual exposure of these materials to be penetrated to this depth will lead to the change in the elastic and plastic properties of the materials through the diffusion of point defects.

#### **4.3.2.2 Energy Loss to Ionization**

Neutrons are uncharged particles, hence do not interact with electrons and therefore do not directly cause excitation and ionization. They do, however, interact with atomic nuclei, sometimes liberating charged particles or nuclear fragments that can directly cause excitation and ionization.

The results revealed in the Figures 4.4 in Section 4.1.4 and Figures 4.16, 4.24, and 4.32 in the Appendix IV and in Appendix V that the % Energy loss to ionization in the fast spectrum was about 2% higher than in the thermal spectrum. The energy loss to ionization

(both from Ions and Recoiling atoms) in the thermal spectrum was low in the SS309 with a percentage loss of 97.14 % (354.5 MeV) followed by SS316 with a percentage of 97.14 % (354.6 MeV). However, SS308 and SS304 were found to have had high energy loss of 97.15 % (354.6 MeV) and 97.18 % (354.7 MeV) to ionization. And in the fast spectrum, the least energy loss to ionization was recorded in SS316 and SS304; 99.33% (1807.9 MeV) energy loss was recorded.

Since the difference in the percentage of energy loss to ionization in the fast spectrum was not different from one another, emphasis would be based on the thermal. That is, the least energy loss was recorded in SS309 which shows how susceptible it is to mechanical damage and that can even be testified with the high number of vacancies produced.

#### **4.3.2.3 Fe-Ni-Cr Alloys' Energy Loss to Phonons**

The energy loss to the target phonons was realized to be higher in the thermal than the fast neutron spectrum reactor design. Figures 4.5 in section 4.1.5 and Fig 4.17, 4.25, and 4.33 in the Appendix IV and in Appendix V. It was seen that in the thermal spectrum, as high as 2.58% (9.43 MeV) was loss by the ions to phonons in SS316, SS309 and SS308 whereas the SS304 recorded a loss of 2.56% (9.34 MeV) to Phonons. However in the fast spectrum all the materials recorded 0.06% energy loss. This implies that there is high vibration in the thermal spectrum than in the fast spectrum and also the SS304 will not experience vibrations as high as the other materials in thermal spectrum and that could be seen from the low number of vacancies produced.

#### **4.3.2.4 Energy Loss to Vacancies Production in Fe-Ni-Cr Alloys (Target Damage Energy)**

Target damage energy as a result of the vacancies produced in the materials could be seen in Appendix V and was extracted from all the collision cascade diagrams (Fig 4.1, Fig 4.13, Fig. 4.21, and Fig 4.29) at the “% Energy Loss” window. It could be seen that there is no significant variation in the percentage loss in both spectrum.

The only difference was with the percentage recorded in the SS304 which was found to be 0.01 % less. This therefore attest to the lower number of vacancies.

It was revealed that the percentage of displaced atoms that were left as vacancies remained same for a particular material for both spectrum. It was seen that 96.5% of the atoms that were displaced in SS304 and SS308 were normally left as vacancies. Also 96.7% of SS316 atoms displaced were left as vacancies and 97 % in the case SS309. This implies that SS304 and SS308 would be least affected by point defects which later agglomerate to form voids leading to swelling, hence SS309 was seen to be much prone that.

#### **4.3.2.5 Energy to Recoil Cascade**

In determining how much energy was transferred to the recoil cascade, all the energies deposited by the recoils were added up as depicted in Fig. 4.1:  $(2.55 \% + 0.26 \% + 2.81 \%) = 5.62 \%$  and  $(0.73 \% + 0.06 \% + 0.60 \%) = 1.39 \%$  of the total energy loss to the target (SS304) recoil cascade representing 20.4 MeV and 25.3 MeV for the thermal and fast neutron spectrum respectively. Thus, 94.38 % (344.5 MeV) of the Ion's energy was deposited to the Fe-Ni-Cr alloy SS304 and only 5.62 % (20.4 MeV) was given up to the recoil cascade in the thermal, whereas 98.60 % (1794.5 MeV) was deposited with 1.39

% (25.3 MeV) given up for the recoil cascade in fast neutron spectrum of the SCWR respectively.

Similar calculations for the other Fe-Ni-Cr alloys showed that recoils in SS308 deposited 6.10 % (22.3MeV) and 1.33 % (24.2 MeV) (see in Fig. 4.13), SS309 deposited 5.79 % (20.9 MeV) and 1.35 % (24.6 MeV) (see in Fig. 4.21) and SS316 deposited 6.05 % (22.1 MeV) and 1.39 % (25.3 MeV) (see in Fig. 4.29) with each pair representing the thermal and fast neutron spectrum respectively.

It can be seen that higher percentage of energy is given up for the recoil cascade in the thermal neutron spectrum than in the fast spectrum leading to less energy deposition by the ion in the thermal spectrum than the latter.

#### **4.3.2.6 Sputtering Yield**

When a collision cascade intersects the surface, sufficient energy can be transferred to a surface atom to overcome its binding to the surface, so that it will be ejected from the solid [96].

The sputtering yield was realized to have decreased from same materials being used in thermal neutron spectrum to the fast neutron spectrum. The SS316 which recorded the highest yield of 0.670 Atoms/Ion reduced to 0.150 Atoms/Ion in the fast spectrum. Also the SS304 which had the least yield of 0.190 Atoms/Ion in the thermal spectrum and then recorded 0.100 Atoms/Ion in the fast spectrum. It illustrates that sputtering yield is inversely proportional to the energy of the incident ions and hence the lower the incident ion's energy, the higher the sputtering.

However, comparing the sputtering yield results with the range of sputtering yield for typical energies of  $10^{-2} < Y < 10^2$ , it could be seen that sputtering would not be a serious damage [97].

### **4.3.3. Discussion on Mechanical Deterioration**

#### **4.3.3.1 Cohesive Energy**

The Equilibrium Lattice constant of 3.489 from the simulation in Appendix VI was seen to be in agreement (only 1 percent difference) with the experimental Equilibrium Lattice constants of 3.499 for the Potential file adapted [94]. This means that the potential file to be adapted is good to use in the simulation since the results from literature or theory tallies statistically with the LAMMPS figure. However the value of the 3.499 was lower than the values used for the simulations as shown in Table 3.5 because the adapted potential was designed for FCC Fe-10Ni-20Cr [94].

The cohesive energy of -4.117 in Appendix VI was also in agreement (only 0.3 percent difference) with the experimental value of -4.120 [94].

The difference 1.0 implies that the potential file was good enough to be used in the simulations.

#### **4.3.3.2 Young's Modulus**

The comparison of the mechanical properties of the materials results in Appendix VII and figure 4.12(a) show that Young's Modulus, which gives the stiffness of the Fe-Ni-Cr alloys decreased with increasing temperature. It was also realized that the Young's modulus for the ambient condition in Table 4.3 was 196 GPa for all the materials, which was within 95% confidence interval for the experimental values from literature in Table 3.1.

The comparison also revealed in fig. 4.12(a) and in Appendix VII that all the materials had a decrease in their Young's Modulus values. The SS304 had the smallest change in its elastic modulus from 196 GPa to 121 GPa (75 GPa) while SS309 and SS316 had greatest change in the modulus from 196 GPa to 118 GPa (78 GPa). This therefore implies SS304 is stiffer than the others since it had high value even at the temperature of 500 °C. [63 and 64] Hence a better material to consider in temperature ranging up to 500 °C as in the proposed SCWR.

#### **4.3.3.3 Yield Strength**

Figure 4.12 (b) and the comparison results in Appendix VII gives the yield strength of the materials at 0.2 % offset. The results indicated that the yield strength which is the minimum stress at which a plastic deformation occur in the materials decreased with an increasing temperature.

The comparison results showed that SS309 though recorded the highest yield strength at ambient condition, recorded lower yield than SS304 when it was further exposed to the SCW condition. Also the highest change in the yield strength was in SS309 material from 9.97 GPa to 5.30 GPa (4.67 GPa) whereas the lowest change was recorded in the SS304 from 9.88 GPa to 5.54 GPa.

#### **4.3.3.4 Ultimate Tensile Strength**

Figure 4.12(c) and in Appendix VII gives the trend of the Ultimate tensile strength (the maximum stress the material can withstand before fracture) of the Fe-Ni-Cr alloys under study. It was seen that the UTS values for the materials also decreased with increasing temperature. However, the values in Appendix VII were not in agreement with the



experimental values in Table 3.1 for the Ambient Conditions. And this might be that we had perfect crystal arrangements with heterogeneous nucleation.

The Ultimate Tensile Strength of the materials were found to be decreasing in the same trend as the Young's Modulus for all the four materials considered. SS308 had the least change of about 4.19 GPa in strength as the temperature increased while SS309 had a fast decrease in UTS from the ambient to the SCW conditions with change of 4.42 GPa. But in general the values registered were of the same order. Also the small change in UTS value of the SS308 indicates that it would not fail as quickly as it is being exposed to extremely harsh conditions.

#### **4.3.3.5 Breaking or Fracture Strength**

The results on the breaking strength, which is the strength at which the material fracture, is shown in Figure 4.12 (c) in Appendix VII. It was realized that the Breaking Strength decreased when the conditions in the reactor became harsh. Thus when the materials were subjected to ambient conditions (pressure = 0.01MPa (1 atm) and temperature = 27 °C) and the SCW condition (pressure= 25 MPa and temperature range of 300 – 500 °C), the breaking strength decreased with an increase in temperature since the pressure was kept constant at the SCW condition.

Though the materials' strength under all the conditions looked same, it was realized that the SS304 had the highest value corresponding to rupture of the materials when the temperature was increased to 500 °C and that can be seen in Table 4.3 in Appendix VI.

#### **4.3.4. Discussions on Coupling Neutron Irradiation Damage and Mechanical**

##### **Deterioration**

The research revealed in the two damage assessments that generally the Fe-Ni-Cr alloys possess similar behavior under irradiation and stress. However, SS304, could be seen in Appendix IV as stronger than the other three materials and hence was less damaged.

The results from the irradiation damage assessment was validated by the LAMMPS code since materials like SS304 and SS308 after the irradiation, were seen to have had a very strong. That is, 96.5 % of the atoms that were displaced in SS304 and SS308 were normally left as vacancies. Also 96.7 % of SS316 atoms displaced were left as vacancies and 97 % in the case SS309.

Also from Fig. 4.11 and 4.12, SS308 and S304 were seen throughout as possessing higher strength. It was evidenced by the fact that there the percentage of atoms vacancies produced from the number of displacements were low and that means that such materials may not experience swelling.

Hence, the need to consider the two materials for in-core structural materials in the SCWR.

## CHAPTER FIVE: CONCLUSIONS AND RECOMMENDATIONS

### 5.1. CONCLUSIONS

The goal of the research was to examine neutron irradiation damage and mechanical degradation of Fe-Cr-Ni alloys (SS304, SS308, SS309 and SS316) by high neutron dose leading to 10 – 30 dpa and 100 – 150 dpa. Thermal and fast neutron bombardments at high pressure and temperature conditions as would pertain in SCW conditions were assessed using Binary Collision Approximation by SRIM-TRIM and Molecular Dynamics simulations by LAMMPS code respectively along with VMD and MATLAB. The research was successful and the conclusions drawn from the outcomes of the thesis were as follows:

- The fast neutron irradiation damage assessment revealed very deep penetration. The incidence ion penetration in the four Fe-Ni-Cr alloys ranged from 11.3  $\mu\text{m}$  to 11.4  $\mu\text{m}$  in the thermal neutron spectrum, the penetration ranged from 32.3  $\mu\text{m}$  to 32.4  $\mu\text{m}$  in the fast spectrum. The difference in penetration depth, for neutron spectrum was significant and the depth of penetration of fast neutrons as compared to the thermal neutrons was about three times that of the thermal neutron spectrum.
- The SS304 required as high as 97.18 % (354.7 MeV) of the Ion's energy for Ionization whiles for SS309 and SS316 required 97.14 % (354.5 MeV) to be ionized in the thermal spectrum. And in the fast spectrum, the least energy loss to ionization was recorded in SS316 and SS304 with 99.33 % (1807.8 MeV) energy loss. There was therefore a marginal difference in energy required to ionize the alloys.
- The energy given off by the recoil atoms as phonons was higher in the thermal neutron spectrum than the fast spectrum. But percentage of energy loss of 2.56 %

recorded by SS304 which was lower than the others implies minimal vibration and hence will lead to fewer atomic displacements.

- The number of defects created by each projectile and energy used up in the production of such defects showed that more energy was used up in the defects creation in the thermal spectrum than in the fast. Also the SS304 and SS308 had the least percentage of displacements left as vacancies.
- The assessment also revealed that the SS316 had high sputtering yield in both spectrum, and hence might experience pitting corrosion.
- The evaluation of mechanical deterioration also revealed that Young's, Ultimate Tensile Strength and the Breaking/ Fracture Strength decreased with increasing temperature.
- The SS304 was found to have high mechanical strength than the other alloys. The strength of the SS304 decreased less than the others when the conditions were changed from the ambient to the supercritical water condition.
- The ultimate tensile strengths, yield strength and breaking strengths were greater than the experimental values.
- Comparing the two methods of assessments, the alloys that performed well in the BCA simulation, equally possessed high mechanical strength from the MD simulation.
- From the damage assessment and the evaluation process SS304 and SS308 were of higher strength than the other alloys and hence could work with least damage under

SCW condition and could be considered in the design of the SCWR internals and pressure vessel.

## **5.2. RECOMMENDATIONS**

Further research work on designing the TRIM.DAT input deck using the computer program, Monte Carlo Neutron Program (MCNP code), which is the code widely used for the transport of Neutron particles through matter should be embarked on. This will ensure that uncertainties in the direction, energy and depth of particles are captured to improve the accuracy of the simulation.

It is also recommended that students who go through the Radiation Damage and Corrosion Models in Reactor Materials course be given demonstrations on special codes such as SRIM-TRIM, ALICE, PHITS, MARS, FLUKA, LAMMPS, AMBER, CHARMM, VMD, and ovito codes since these are the current and efficient codes for material analysis. Additional research work should be done on the two Fe-Ni-Cr alloys, SS304 and 308 to examine on hydrogen embrittlement, swelling and creep, and interactions with the supercritical water environment; an extensive testing and evaluation program is required to assess the corrosion effects that will be seen on the properties of these potential SCWR materials.

## REFERENCES

- [1] Kirillov, P. L. (2008). Supercritical Water Cooled Reactors. *Journal of Thermal Engineering*, Russian Academy of Sciences, Vol. 55, No. 5, pp. 361 -364.
- [2] Yang, W. (2012) Fast Reactor Physics and Computational Methods. *Nuclear Engineering and Technology*, Korean Nuclear Society, Vol. 504, No. 1, pp. 177 -198
- [3] Ojefua, G. O., Amidu, A.M. and Yehwudah, C. E. (2013). Science and Technology of Supercritical Water Cooled Reactors: Review and Status. *Journal of Energy Technologies and Policy*, Vol. 3, No. 7, pp. 1-10
- [4] Peiman, W., Pioro, I., Gabriel, K. (2012). Thermal Aspects of Conventional Alternative Fuel in Supercritical Water-Cooled Reactor (SCWR) Applications. In Prof. Amir Mesquita (Ed.), Nuclear Reactors, InTech, Croatia, pp 1-35
- [5] Technology Roadmap Update for Generation IV Nuclear Energy System <https://www.gen-4.org/gif/upload/docs/application/pdf/2014-03/gif-tru2014.pdf>, 15<sup>th</sup> January, 2015
- [6] Corwin, W., and Nanstad, R. (2003). Supercritical Water Reactor (SCWR); Survey of Materials Experience and R&D Needs to Assess Viability. NEEL/EXT-03-00693 Revision 1, Idaho National Engineering and Environmental Laboratory, Bechtel BWXT Idaho, USA.
- [7] Danielyan, D. (2003). Supercritical-Water-Cooled Reactor System- as one of the most promising type of Generation IV Nuclear Reactor. *Journal of Technology*, American Nuclear Society, USA, pp. 1-18
- [8] Baindur, S. (2008). Materials Challenges for the Supercritical Water-Cooled Reactor. *Bulletin of the Canadian Nuclear Society*, Vol 29, No. 1, pp. 32-38
- [9] Buckthorpe, D. (2010). Materials Challenges for the Next Generation of Fission Reactor Systems. Amec Foster wheeler, Booth Park, Knutsford, Cheshire, UK,.
- [10] Buongiorno, J. (2004). The Supercritical Water-cooled Reactor: Ongoing Research and development in US. In Proc. of International Congress on Advances in Nuclear Power Plants, American Nuclear Society, La Grange Park, United State.
- [11] Oka, Y., Koshizuka, S., Ishiwatari, Y., and Yamaji, A. (2010). Super Light Water Reactors and Super-Fast Reactors. Springer, New York, NY, USA.

- [12] Gladstone, S., and Sesonske, A. (1998). Nuclear Reactor Engineering. 3<sup>rd</sup> Edition, Van Nostrand Reinhold Company, New York, USA, pp. 437 – 463
- [13] Matsui, H., Sato, Y., Saito, N., Kano, F., Ooshima, K., Kaneda, J., Moriya, K., Ohtsuka, S., Oka, Y. (2007). Material Development for Supercritical Water-cooled Reactors. In Proc. of International Congress on Advances in Nuclear Power Plants, Nice, France.
- [14] Design of a Supercritical Water-Cooled Reactor – Pressure Vessel and Internals, [http://elib.uni-stuttgart.de/opus/volltexte/2008/3676/pdf/Dissertation\\_Fischer.pdf](http://elib.uni-stuttgart.de/opus/volltexte/2008/3676/pdf/Dissertation_Fischer.pdf), 16<sup>th</sup> December 2014. pp. 85-90
- [15] Olander, D. R. (1976). Radiation Damage: Fundamental Aspects of Nuclear Reactor Elements. Department of Nuclear Engineering, University of California, Berkeley, USA.
- [16] Ye, B. (2011). Formation and Growth of Irradiation-Induced defects structures. University of Illinois at Urbana-Champaign, USA.
- [17] Tulkki, V. (2006). Supercritical Water Reactors. *Master's Thesis*, Helsinki University of Technology, Helsinki, Finland.
- [18] Pioro, I. L., and Duffey, R. B. (2007). Heat Transfer and Hydraulic Resistance at Supercritical Pressure in Power-Engineering Applications. America Society of Mechanical Engineers, New York, USA.
- [19] Hanninen, H. (2009). Material Development in New Reactor Designs – Gen III and SCWR Concept. Helsinki University of Technology, Espoo, Finland.
- [20] U.S. DOE Nuclear Energy Research Advisory Committee and the Generation IV International Forum. (2002). A Technology Roadmap for Generation IV Nuclear Energy Systems, Report, pp. 1-22
- [21] Cheng, X., Liu X., and Yang Y. (2008). A mixed core for Supercritical Water-Cooled Reactors. *Nuclear Engineering and Technology Journal*, Vol 40, No. 2, pp. 117 – 126
- [22] Schulenberg, T., Starflinger, J., and Aksan, N. (2006). Supercritical Water Reactor Research in GIF context: Current Status and Future Prospects with Emphasis on European Activities. [ftp://ftp.cordis.europa.eu/pub/fp6-euratom/docs/fisa2006\\_irc\\_scur\\_en.pdf](ftp://ftp.cordis.europa.eu/pub/fp6-euratom/docs/fisa2006_irc_scur_en.pdf), 4<sup>th</sup> April 2015.
- [23] Schulenberg, T., and Starflinger, J. (2012). High performance light water reactor – design and analyses. Karlsruhe Institute of Technology Scientific Publishing, Germany.

- [24] Nuclear Energy Agency. (2013). Status Report on Structural Materials for Advanced Nuclear Systems, Report No. 6409, Organization of Economic Co-operation and Development, Paris, France.
- [25] Maloy, S. (2012). Materials Challenges for Fission Energy. Nuclear Energy Program, Los Alamos National Laboratory, and Nuclear and Industrial Safety Agency, USA.
- [26] Ragheb, M. (2014), Fourth Generation Reactor Concepts. *Atomic Energy*, USA
- [27] Supercritical Water Cooled Reactor, [nuclear.inl.gov/deliverables/docs/a2-s-scwr\\_fy07\\_external.pdf](http://nuclear.inl.gov/deliverables/docs/a2-s-scwr_fy07_external.pdf), 11<sup>th</sup> November, 2014
- [28] Dong, N., and Weida, Y. (2009). Several Aspects on Materials Problems for SCWR. In Proc. International Conference on Opportunity and Challenges for Water Cooled Reactors in 21<sup>st</sup> Century, Vienna, Austria.
- [29] Radiation Damage to Materials, Instructional Text, Course 228-Module-4, pp. 1-12
- [30] Vörtler, K., Juslin, N., Bonny, G., Malerba, L and Nordlund, K. (2011)' The effect of prolonged irradiation on defect production and ordering in Fe-Cr and Fe-Ni alloys. *Journal of physics. (Condensed Matter)* Vol. 23, Issue 35.
- [31] Stoller, R. (2012). Radiation Damage: Mechanism and Modeling. Material Science and Technology Division, Oak Ridge National Laboratory,
- [32] Stoller, R.E. (2011). Radiation Damage Fundamentals: Primary Damage Production, Materials Science and Technology Division. Oak Ridge National Laboratory, Joint EFRC Summer School, Knoxville, TN, USA.
- [33] Stoller, R. E. (2004). Advanced Computational Material Science; Application to Fusion and Generation IV Fission Reactors. Workshop Report, USA.
- [34] International Atomic Energy Aagenc. (2009). Integrity of Reactor Pressure Vessels in Nuclear Plants. *IAEA Nuclear Energy Series*, No. NP-T-3.11.
- [35] Meimei, Li. (2012). Radiation Effects in Superconducting Magnet Materials (RESMM12). Femilab, USA.
- [36] O'Neill, C. A. (2006). Computer Simulations of Radiation Shielding Materials for use in the Space Radiation Environment. *M.Sc. Thesis*, College of William and Mary, Williamsburg, Virginia, USA



- [37] Wang, J. J. (2010). Lessons Learned from Developing Reactor Pressure Vessel Steel Embrittlement Database. Oak Ridge National Laboratory, pp. 7-10
- [38] Lui, S. and Cai, J. (2014). Design & optimization of two breeding thorium-uranium mixed SCWR fuel assemblies. *Progress of Nuclear Energy*, vol. 70, pp. 6-19
- [39] Stoller, R. E., and Mansur L. (2005). An Assessment of Radiation Damage Models and Methods, Office of Nuclear Energy Science and Technology. Oak Ridge National Laboratory, Department of Energy, USA.
- [40] Rutherford, A. (2009). Electronic Effects in Radiation Damage Simulation in Metals. *Thesis paper*, pp. 39- 46
- [41] Marsault, Ph., Renault C., Rimpault G., Dumaz P., and Antoni O.(2004). Pre-design studies of SCWR in fast neutron spectrum: evaluation of operating conditions and analysis of the behavior in accidental situations. In. Proc. of International Congress on Advances in Nuclear Power Plants, Pittsburgh, USA.
- [42] Yamada, K., Sakurai, S., Asanuma, Y., Hamazaki, R., Ishiwatari ,Y., and Kitoh, K. (2011). Overview of the Japanese SCWR concept developed under the GIF collaboration. Procedure ISSCWR-5, Vancouver, Canada, pp.13-16.
- [43] Vorteler, K., Juslin N., and Bonny G. (2011). The effect of prolonged irradiation on defect production and ordering in Fe-Cr and Fe-Ni Alloys. *Journal of Physics*. (Condensed Matter), Vol 23, No. 35, pp. 355007
- [44] Vinay, K. M., Verma S., and Shobha V. (2014). 100 MeV Si<sup>7+</sup> Ion Irradiation Induced Modifications in Electrical Characteristics of Si Photo Detector: An In-Situ Reliability Study. *Journal of Material Sciences Research*, Vol 3, No. 3 pp. 24-32.
- [45] Radiation Damage, <http://www4.ncsu.edu/~murty/NE509/NOTES/Ch3-RadiationDamage.pdf>, , 5<sup>th</sup> April, 2014
- [46] Fasso, A., Ferrari, A., Smirnov, G., Sommerer, F., and Vlachoudis V. (2001). FLUKA Realistic Modelling of Radiation Induced Damage. *Progress in Nuclear Science and Technology*, Vol. 2, pp. 769 – 775
- [47] Radiation Damage I ,  
[http://defects.materials.ox.ac.uk/uploads/files/Radiation\\_Damage\\_Lecture\\_1.pdf](http://defects.materials.ox.ac.uk/uploads/files/Radiation_Damage_Lecture_1.pdf), , 10<sup>th</sup> April, 2014

- [48] Was, G. S. (2007). *Fundamentals of Radiation Materials Science. Metals and Alloys*, Springer-Verlag Belin Heidelberg, New York, USA.
- [49] Olander, D., and Motta, A. (2013). *Light Water Reactor Materials*. Chapter 12: Radiation Damage, pp. 1-44
- [50] Bratchenko, M.I., Bryk, V.V., Dyuldy, S. V., Kalchenko, A.S., Lazarev, N.P, and Voyevodin, V.N. (2013). Comments on DPA calculation methods for ion beam driven simulation irradiations. Kharkov Institute of Physics and Technology, Kharkov, Ukraine, Vol. 84, No. 2, pp. 1-6.
- [51] Wirth, B., and Olander, D. (2006). Neutron Irradiation Effects. Berkeley, USA.
- [52] Kinchin, G. H., and Pease, R. S. (1983). The Displacement of Atoms in Solids. *Rep. Progress Physics*, Vol. 18, pp. 70-77
- [53] Bradley, C. R. (1988). Calculations of Atomic Sputtering and Displacement cross-sections in solid elements by electrons with energies from threshold to 1.5 MV. Material Science Division, Argonne National Laboratory, Tennessee, USA.
- [54] Wootan, D. (2014). DPA Calculation Methodologies used in Fission and Fusion Reactor Materials. Pacific Northwest National Laboratory, USA.
- [55] Wirth, B. D. (2006). An introduction to Material Degradation in Nuclear Environment. Lecture Notes, NE120 Section 1, Nuclear Engineering department , University of California, Berkeley, USA, Section 1, pp. 24
- [56] Poivey, C., and Hopkinson G. (2009). Displacement Damage Mechanism and Effects. Space Radiation and its effect of EEE components, EPFL Space Centre, pp. 2-24
- [57] Development of Radiation resistant reactor core structural materials, (2014). [http://www.iaea.org/About/Policy/GC/GC51/GC51InfDocuments/English/gc51inf-3-att7\\_en.pdf](http://www.iaea.org/About/Policy/GC/GC51/GC51InfDocuments/English/gc51inf-3-att7_en.pdf), pp. 2
- [58] Wessel, J.K. (2004). Handbook of Advanced Materials. Wessel and Associate, Oak Ridge, Tennessee, USA.
- [59] Outokumpu high performance steel (2013). *Handbook of Stainless Steel.*, Avesta, Sweden.
- [60] [http://www.aksteel.com/pdf/markets\\_products/stainless/stainless\\_steel\\_comparator.pdf](http://www.aksteel.com/pdf/markets_products/stainless/stainless_steel_comparator.pdf), 11<sup>th</sup> November, 2014.

- [61] Austenitic Stainless Steels (2008). Stainless Steels for Design Engineers. pg. 1-12
- [62] Appiah-Ofori, F.F. (2014). Assessment of gamma irradiation heating and damage in miniature neutron source reactor vessel using computational methods and simulation codes. *MPhil Thesis*, Department of Nuclear Engineering, School of Nuclear and Allied Science, University of Ghana, Legon, Ghana
- [63] Gurbuz, R., and Cevik, G. (2003). Tension Test. *Experiment 1*, Department of Metallurgical and Materials Engineering, Middle East Technical University,
- [64] Degarmo, E. P., Black, J. T., Kohser, R. A. (2003). Materials and Processes in Manufacturing. Wiley, 9th ed., p. 32.
- [65] Robinsin, M., and Torrens, I. (1974). Computer Simulation of atomic-displacement cascades in solids in the binary-collision approximation. *Physical Review*, Vol.9, No.12 pp. 5008
- [66] Moliere, G. (1947). Naturforsch Z. Vol. **2A**, pp. 133.
- [67] Yamamura, Y., and Mizuno, Y. (1985). Low-Energy Sputterings with the Monte Carlo Program ACAT. *Inst. Plasma Phys.*, Nagoya Univ., Japan, IPPJ-AM-40
- [68] Andersen, H. H., and Ziegler, J. F. (1977). The Stopping and Ranges of Ions in Matter. Vol. 3, Pergamum Press, Oxford, UK.
- [69] Stopping and Range of Ions in Matter,  
[http://en.wikipedia.org/wiki/Stopping\\_and\\_Range\\_of\\_Ions\\_in\\_Matter](http://en.wikipedia.org/wiki/Stopping_and_Range_of_Ions_in_Matter), , 13<sup>th</sup> April, 20
- [70] Lindhard, J., Scharff, M., Schiött, H. E., and Dan, K. (1963).. *Vidensk. Selsk, Mat. Fys. Medd.*, Vol. 33, No. 14.
- [71] Lee, J.G. (2012). Computational Materials Sciences: An Introduction. CRC Press, Taylor & Francis Group, 1<sup>st</sup> Edt., New York, USA
- [72] Capps, N.A. (2013). Molecular Dynamics Simulations of Cascade Evolution near Pre – Existing Defects. *Master's Thesis*, University of Tennessee,  
[http://trace.tennessee.edu/utk\\_gradthes/2599](http://trace.tennessee.edu/utk_gradthes/2599)
- [73] Cuendet, M. (2008). Molecular Dynamics Simulation. EMBL

- [74] Crozier, P., Plimpton, S., Thompson, A, and Brown, M.(2010). A brief survey of the LAMMPS MD code; intro, case studies, and future development. *LAMMPS Users' Workshop*, CSRI Building, Albuquerque, pp. 8
- [75] Sika-Boafo, D. (2012). Simulation of Defects in (Be and Al) by Neutron Irradiation in the Ghana Research Reactor (GHARR – 1) Core using the MCNP5 and TRIM Codes. *MPhil Thesis*, Department of Nuclear Engineering, School of Nuclear and Allied Science, University of Ghana, Legon, Ghana
- [76] Ziegler, J.F., Biersack, J.P., and Littmark, U. (1996). The Stopping and Range of Ions in Solids. Pergamum Press, New York, USA
- [77] Ziegler, J. F., Biersack, J. P. and Ziegler, M. D. (2008). SRIM-The Stopping and Range of Ions in Matter (SRIM). Pergamon Press, New York, USA
- [78] Ziegler, J. F., Ziegler, M. D., and Biersack, J. P. (2010). SRIM – The Stopping and Range of Ions in Matter. Pergamum Press, New York, USA.
- [79] Ferguson, A. L. (2014). Molecular Dynamics with LAMMPS. ICME Research Workshop, Department of Materials Science and Engineering, University of Illinois, Urban-Champaign, USA.
- [80] <http://lammps.sandia.gov/doc/Manual.pdf>, LAMMPS User's Manual
- [81] [http://www.ks.uiuc.edu/Research/vmd/allversions/what\\_is\\_vmd.html](http://www.ks.uiuc.edu/Research/vmd/allversions/what_is_vmd.html), Beckman Institute for Advanced Science and Technology, 14<sup>th</sup> June, 2015
- [82] Humphrey, W., Dalke, A. and Schulten, K. (1996). VMD - Visual Molecular Dynamics. *Journal of Molecular Graphics*, Vol. 14, No.1, pp. 33-38.
- [84] ASM Metals Handbook (1980), Vol 3, 9<sup>th</sup> Ed.
- [85] [http://www.aksteel.com/pdf/markets\\_products/stainless/stainless\\_steel\\_comparator.pdf](http://www.aksteel.com/pdf/markets_products/stainless/stainless_steel_comparator.pdf), 5th January, 2015.
- [86] Outokumpu high performance steel. (2013). Handbook of Stainless Steel. Avesta, Sweden
- [87] DOE Fundamentals handbook (1993), *Material Science*, Vol. 2, No. 2,
- [88] Wessel, J.K. (2004). Handbook of Advanced Materials. *Wessel and Associate*, Oak Ridge, Tennessee, USA.

- [89] Robinson, M.T. (1994). Universal Interatomic potential. *Journal of Nuclear Matter*, Vol. 216, No. 1
- [90] Sigmund, P. (1969). Theory of sputtering I. Sputtering yield of Amorphous and Polycrystalline Targets. *Phys. Rev.* Vol. 184, No. 383
- [91] Nascimento, F. C. (2009). A comparative study of Mechanical and Tribological Properties of AISI-304 and AISI-316 Submitted to Glow Discharge Nitriding. *Materials Research*, Vol.12, No.2, pp. 173-180
- [92] Verlet, L. (1968). Computer “experiments” on classical fluids II, Equilibrium correlation functions. *Phys. Rev.* Vol.165, pp. 201-214.
- [93] Arachchige, N. D. M. (2012). Molecular Dynamics Study of Geometric Defects on the Mechanical Properties of Graphene. *Master of Applied Science Thesis*, Faculty of Graduate Studies, University of British Columbia, Vancouver, pp. 30- 37
- [94] Bonny, G., Terentyev, D., Pasianot, R. C., Ponce, S., and Bakaev, A. (2011). Interatomic potential to study plasticity in stainless steels: the FeNiCr model alloy. *Modelling and Simulation in Material Science and Engineering*, Vol. 085008, No. 19., USA.
- [95]  
<http://libvolume7.xyz/physics/bsc/semester5/nuclearphysics1andsolidstatephysics1/propertiesofcrystals/propertiesofcrystalstutorial1.pdf>
- [96] Moller, W. (2002). Fundamentals of Ion-Surface Interaction. Lecture Note, Technical University of Dresden, pp. 1-17
- [97] Anderson, H.H. and Bay H.L. (1981). Sputtering Yield Measurements in Sputtering by Particle Bombardment I. *Physical Sputtering of Single-Element Solids*, ed. R. Behrisch, Springer Verlag, Berlin, pp. 145-218

## APPENDICES

## APPENDIX I

## TRIM.DAT Input Deck For SRIM-TRIM Simulation of Neutron Irradiation Damage Assessment of Fe-Ni-Cr Alloys

Û	BBBBBBBBBB TRIM with various Incident Ion Energies/Angles and Depths	BBBBBBBBBBBBBBÛ
Û	Top 10 lines are user comments, with line #8 describing experiment.	Û
Û	Line #8 will be written into all TRIM output files (various files: *.TXT).	Û
Û	Data Table line consist of: EventName (5 char) +8 numbers separated by spaces.	Û
Û	The Event Name consists of any 5 characters to identify that line.	
Û		
Û	Cos(X) = 1 for normal incidence, and Cos(X) = -1 for backwards.	
	BBBBBBBBBBBBBBBBBBBBBBBBBBBBBBBB Typical Data File is shown below	BB

### ÉÍ Neutron Ions from Uranium into Stainless Steel 0.46m thick (Energies 1GeV), Various Angles)

Event Name	Atom Numb	Energy (eV)	Depth X_(A)	Lateral-Position			----- Atom Direction -----		
				Y_(A)	Z_(A)	Cos(X)	Cos(Y)	Cos(Z)	
A-1	92	1E9	7E5	3.5E4	0	1.00000	-.002000	-.100010	
A-2	92	1E9	7E5	3.5E4	0	1.00000	-.022000	-.100020	
A-3	92	1E9	7E5	3.5E4	0	1.00000	-.300000	-.100030	
A-4	92	1E9	7E5	3.5E4	0	1.00000	-.000000	-.100040	
A-5	92	1E9	7E5	3.5E4	0	1.00000	.000000	-.100050	
A-6	92	1E9	7E5	3.5E4	0	1.00000	-.000000	-.100060	
A-7	92	1E9	7E5	3.5E4	0	1.00000	-.000000	-.100070	
A-8	92	1E9	7E5	3.5E4	0	1.00000	-.000000	-.100080	
A-9	92	1E9	7E5	3.5E4	0	1.00000	-.000000	-.100090	
A-10	92	1E9	7E5	3.5E4	0	1.00000	-.000000	-.100100	
.	.	.	.	.	.	.	.	.	
.	.	.	.	.	.	.	.	.	
.	.	.	.	.	.	.	.	.	
A-91	92	1E9	7E5	3.5E4	0	1.00000	-.000000	-.131000	
A-92	92	1E9	7E5	3.5E4	0	1.00000	-.000000	-.132000	
A-93	92	1E9	7E5	3.5E4	0	1.00000	-.000000	-.133000	
A-94	92	1E9	7E5	3.5E4	0	1.00000	-.000000	-.134000	
A-95	92	1E9	7E5	3.5E4	0	1.00000	-.000000	-.135000	
A-96	92	1E9	7E5	3.5E4	0	1.00000	-.000000	-.136000	
A-97	92	1E9	7E5	3.5E4	0	1.00000	-.000000	-.137000	
A-98	92	1E9	7E5	3.5E4	0	1.00000	-.000000	-.138000	
A-99	92	1E9	7E5	3.5E4	0	1.00000	-.000000	-.139000	
A-100	92	1E9	7E5	3.5E4	0	1.00000	-.000000	-.140000	

## APPENDIX II

### Input Files for Molecular Dynamics Simulation of Mechanical Damage Assessment

#### a) Potential File

The potential file **FeNiCr.eam.alloy** modified for the simulation was downloaded from NIST Interatomic Potentials Repository Project (<http://www.ctcms.nist.gov/potentials>)

#### b) Input file for the Cohesive energy determination

# Determination of the cohesive energy and equilibrium lattice constant of the FeNiCr.eam.alloy potential with fcc configuration Adapted from Mark Tschopp, 2010

#By Collins Nana Andoh (10443957)

```
# ----- Initialize Simulation -----
clear
units metal
dimension 3
boundary p p p
atom_style atomic
atom_modify map array
# ----- Create Atoms -----
lattice      fcc 4
region       box block 0 1 0 1 0 1 units lattice
create_box   1 box

lattice      fcc 4 orient x 1 0 0 orient y 0 1 0 orient z 0 0 1
create_atoms 1 box
replicate 1 1 1
# ----- Define Interatomic Potential -----
pair_style eam/alloy
pair_coeff * * FeNiCr.eam.alloy.u3 Fe
neighbor 2.0 bin
neigh_modify delay 10 check yes
# ----- Define Settings -----
compute eng all pe/atom
compute eatoms all reduce sum c_eng

# ----- Run Minimization -----
reset_timestep 0.001
fix 1 all box/relax iso 0.0 vmax 0.001
thermo 10
thermo_style custom step pe lx ly lz press pxx pyy pzz c_eatoms
min_style cg
minimize 1e-25 1e-25 5000 100000
run 0
variable natoms equal "count(all)"
variable teng equal "c_eatoms"
variable teng equal "pe"
variable length equal "lx"
variable ecoh equal "v_teng/v_natoms"

print "Total energy (eV) = ${teng};"
print "Number of atoms = ${natoms};"
print "Lattice constant (Angstroms) = ${length};"
print "Cohesive energy (eV) = ${ecoh};"
print "All done!"
```

### c) A copy of the 16 Input Files used for this work

```
# This program is aimed at evaluating the mechanical integrity (Youngs modulus, Ultimate tensile Strength, Fracture point) of SS 304 treated under Ambient Temperature condition
# Adapted from materials developed by Mark A. Tschopp (US ARL) and hosted at https://icme.hpc.msstate.edu
# Designed By: Collins Nana Andoh 1044395 2015
#####

# ----- Initialize Simulation -----
clear
units          metal
dimension      3
boundary       p          p          p
atom_style     atomic

# ----- Create Atoms -----
lattice        fcc 3.5918
region         new_region block 0 10 0 10 0 10
create_box     1 new_region
lattice        fcc 3.5918 orient x 1 0 0 orient y 0 1 0 orient z 0 0 1
create_atoms   1 region new_region
replicate      1 1 1

# ----- Define Interatomic Potential -----
pair_style     eam/alloy
pair_coeff     * * FeNiCr.eam.alloy.u3 Fe
neighbor       2.0 bin
neigh_modify   delay 0 every 10 check yes

# ----- Define Settings -----
compute       csym all centro/atom fcc
compute       eng all pe/atom
# ----- Equilibration-----
#reset timer
reset_timestep 0
#2 fs time step
timestep      0.002
#initial velocities
velocity      all create 300 12345 mom yes rot no
#thermostat + barostat (1 degree= 273 K and 1 MPa= 10 bar
fix           1 all npt temp 473 473 2 iso 250 250 1 drag 1.0
# instrumentation and output
variable s1 equal "time"
variable s2 equal "lx"
variable s3 equal "ly"
variable s4 equal "lz"
variable s5 equal "vol"
variable s6 equal "press"
variable s7 equal "pe"
variable s8 equal "ke"
variable s9 equal "etotal"
variable s10 equal "temp"
fix writer all print 250 "${s1} ${s2} ${s3} ${s4} ${s5} ${s6} ${s7} ${s8} ${s9} ${s10}" #file Fe_eq.txt screen no
#thermo
thermo        500
thermo_style  custom step time cpu cpuremain lx ly lz press pe temp
#dumping trajectory
dump          1 all atom 250 dump.eq.lammpstrj
#24 ps MD Simulation (assuming 2 fs time step)
run           12000
#clearing fixes and dumps
unfix         1
undump        1

#saving equilibrium length for strain calculation
variable tmp equal "lx"
```



```

variable L0 equal ${tmp}
print "Initial Length, L0: ${L0}"
#-----DEFORMATION-----
#reset timer
reset_timestep          0
#2 fs time step
timestep                0.002
# thermostat + barostat
fix                     1 all npt temp 300 300 1 y 0 0 1 z 0 0 1 drag 1.0
#nonequilibrium straining in x-direction at strain rate = 5e-3
variable srate1 equal   5e-3
fix                     2 all deform 1 x erate ${srate1} units box remap x
#instrumentation and output for units metal, pressure is in #[bars] = 100 [kPa]= 1/10000 [GPa] => p2, p3, p4, are in GPa
variable strain equal "(lx - v_L0)/v_L0"
variable p1 equal "v_strain"
variable p2 equal "-pxx/10000"
variable p3 equal "-pyy/10000"
variable p4 equal "-pzz/10000"
fix writer all print 125 "${p1} ${p2} ${p3} ${p4}" file Fe.deform.txt screen no
#thermo
thermo                  1000
thermo_style            custom step cpuremain v_strain v_p2 v_p3 v_p4 press pe temp
#dumping standard atom trajectories
dump                    1 all atom 5000 dump.deform.lammpstrj
#dumping custom cfg files containing coords + ancillary variables
dump                    2 all cfg 5000 dump.deform_*.cfg mass type xs ys zs c_csym c_eng fx fy fz
dump_modify             2 element Fe
#40 ps MD Simulation (assuming 2 fs time step)
run                     20000
# clearing fixes and dumps
unfix                   1
unfix                   2
unfix                   writer
undump                  1
undump                  2
#####
print "All done"

```

### **APPENDIX III**

#### **Algorithm for Animation of Tensile Deformation Using VMD**

1. Open the VMD program
2. In the Main VMD window, click on file
3. In the file menu, select new molecules
4. In the Molecule file browser, browse for the dumb file (dump.deform.lammpstrj), select file type(LAMMPS trajectory) and load
5. In the Main VMD window, click on the Graphics and select Representation
6. In the Graphical Representation dialog box, select Name, VDW and Opaque in the Colouring Method, Drawing Method and Material slot and then click on the apply.
7. In the Main VMD window, click on the play bottom to give you the animation of the deformation.

## APPENDIX IV

### SRIM-TRIM Simulation Output Spectra for Neutron Irradiation Damage Assessment

#### i) SS308

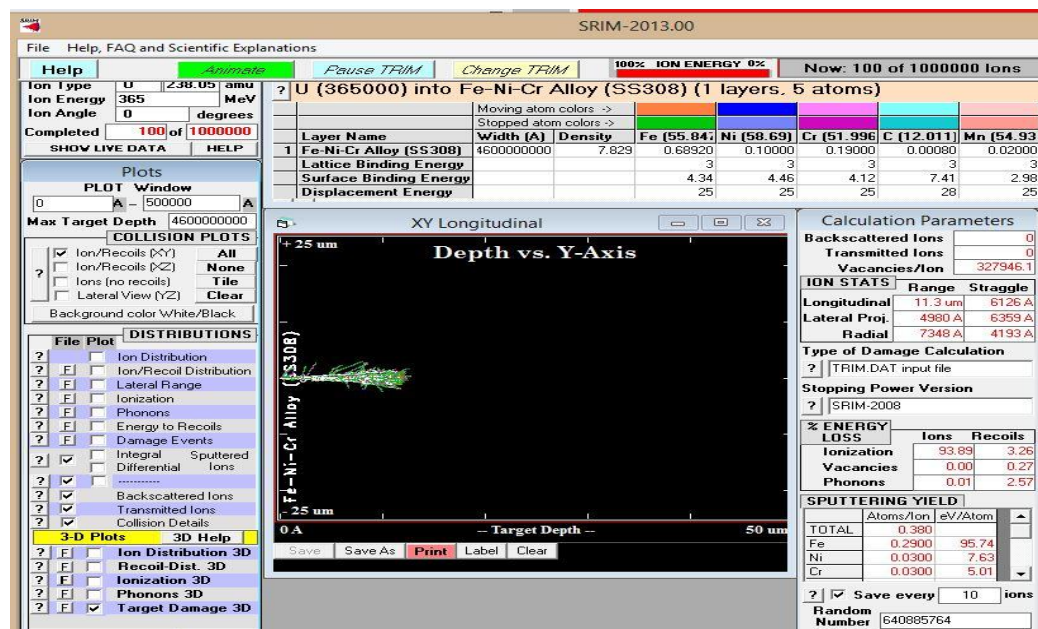


Fig 4.13(a)

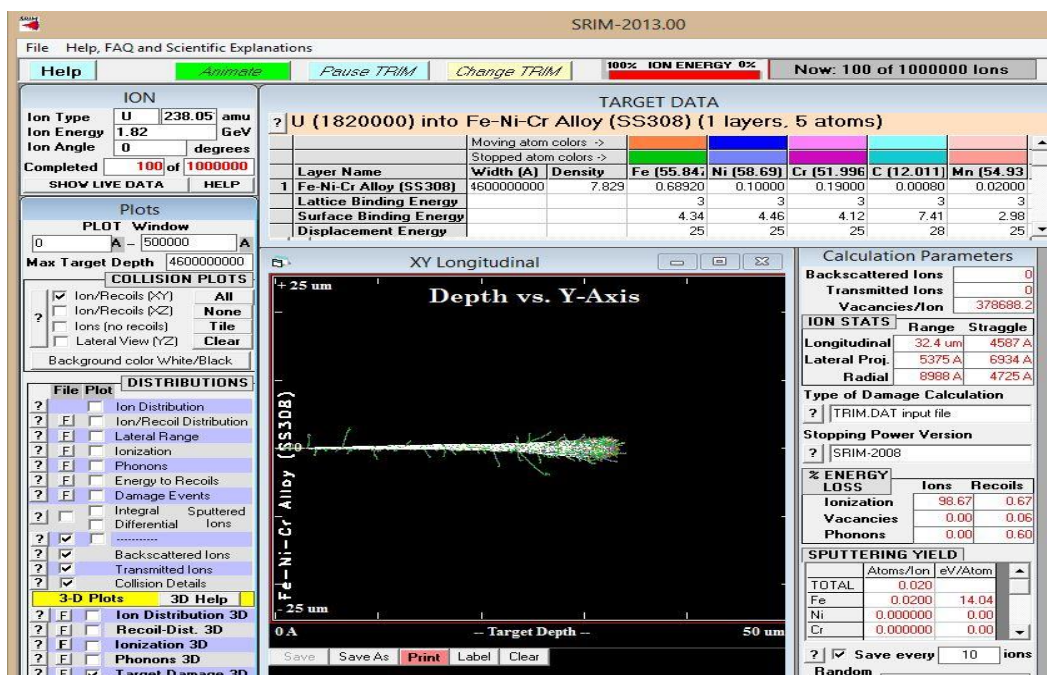


Fig 4.13(b)

Fig. 4.13: Collision Cascade for (a) thermal and (b) fast neutron damage for SS308

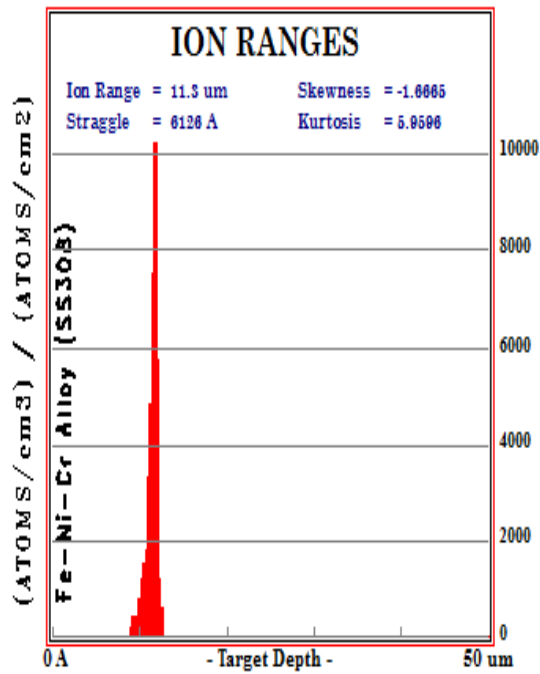


Fig 4.14 (a)

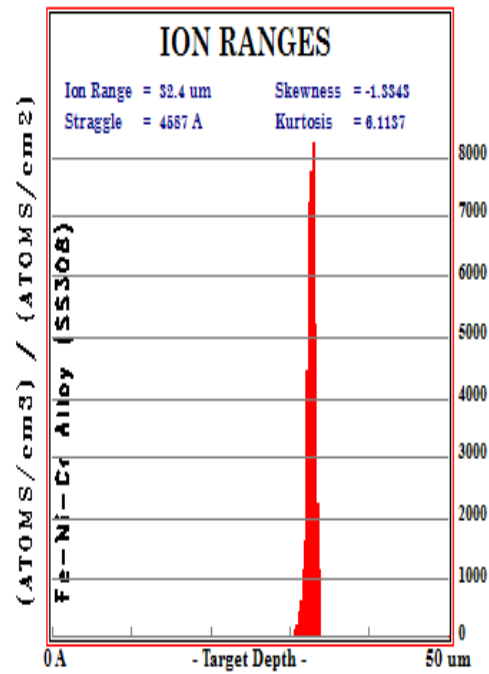


Fig 4.14 (b)

Fig 4.14: Depth of penetration of (a) thermal and (b) fast neutrons in the SS308

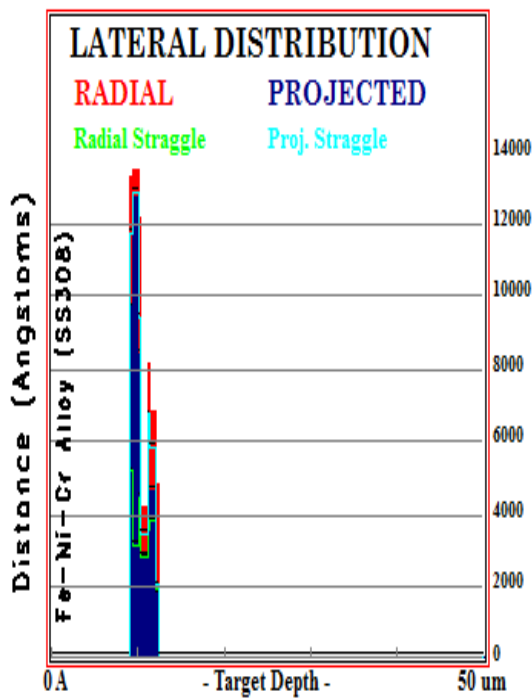


Fig 15 (a)

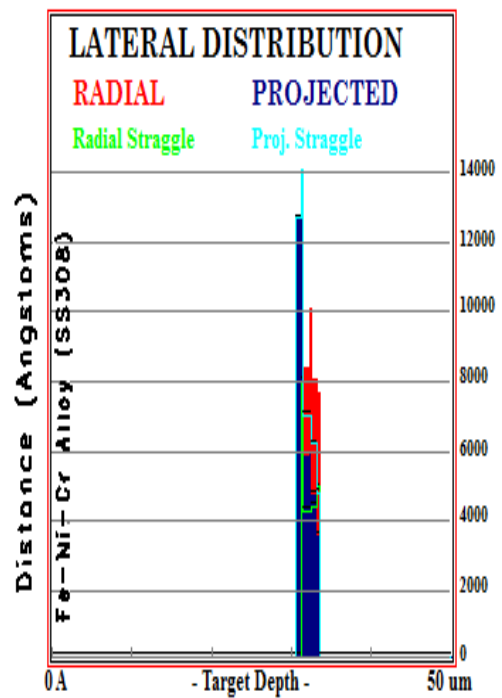


Fig 15 (b)

Fig 4.15: Lateral Range Distribution of (a) thermal and (b) fast neutrons in the SS308

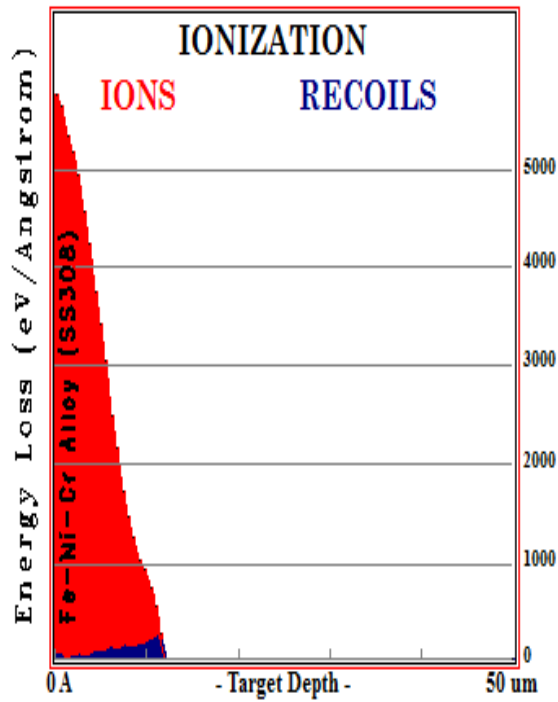


Fig 4.16(a)

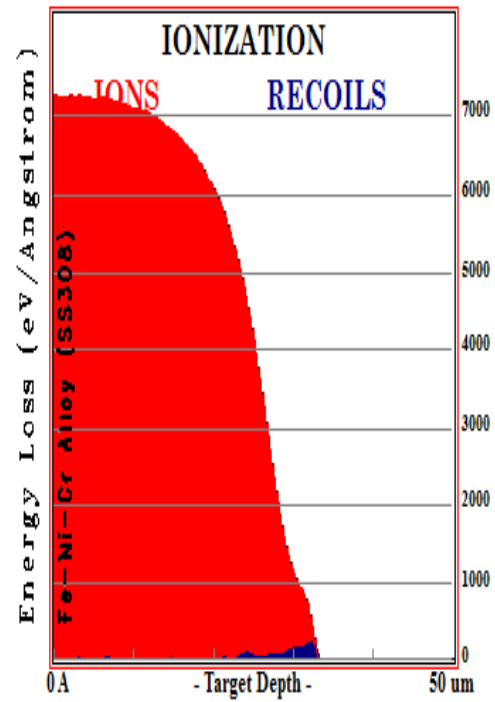


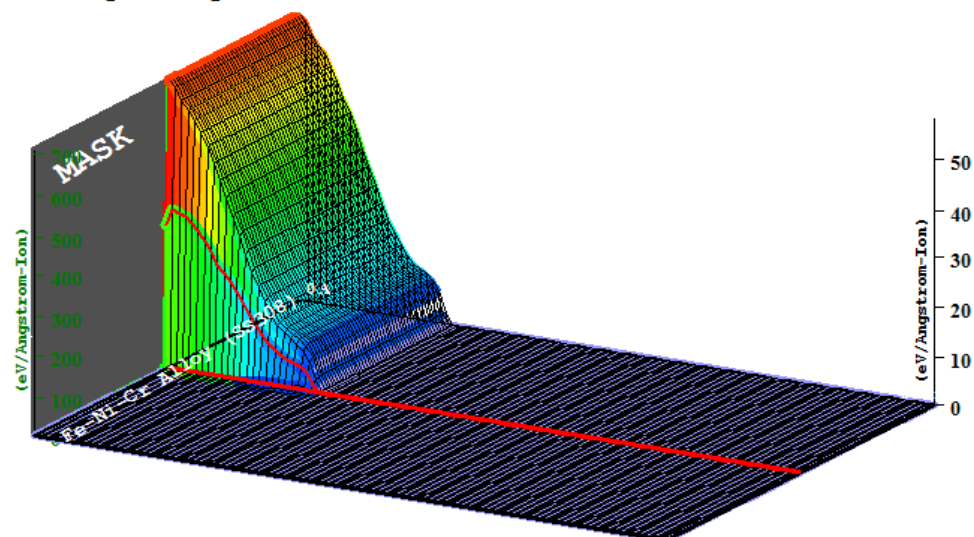
Fig 4.16(b)

## Target Ionization

Total Ionization = 354607.7 keV / Ion

Total Phonons = 9408.8 keV / Ion

Total Target Damage = 983.48 keV / Ion



Plot Window goes from 0 A to 50 um; cell width = 5000 A  
Press PAUSE TRIM to speed plots. Rotate plot with Mouse.

**Ion = U (365. MeV)**

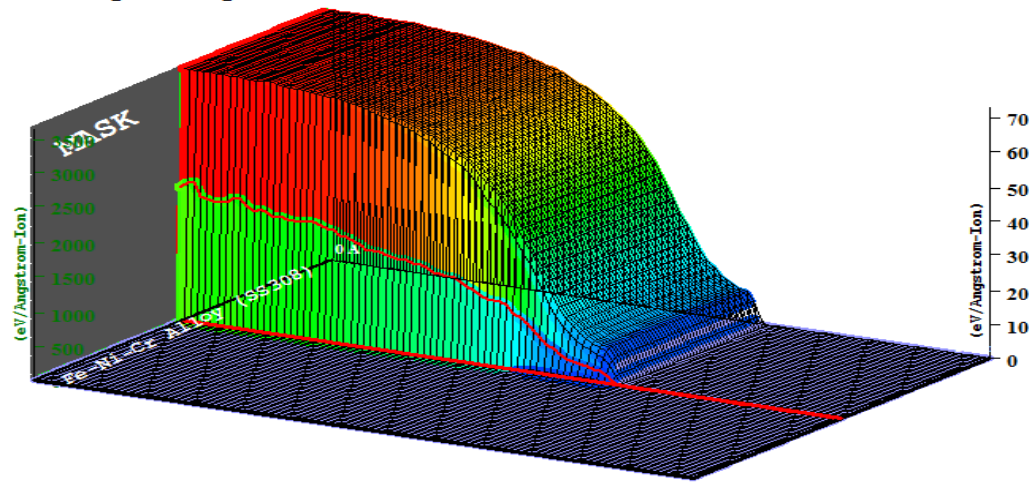
Fig 16(c)

## Target Ionization

Total Ionization = 1807965.8 keV / Ion

Total Phonons = 10898.2 keV / Ion

Total Target Damage = 1135.95 keV / Ion



Plot Window goes from 0 A to 50 um; cell width = 5000 A.  
Press PAUSE TRIM to speed plots. Rotate plot with Mouse.

**Ion = U (1820. MeV)**

Fig. 16(d)

Fig 4.16: 2D and 3D view of Ionization energy distribution of the Fe-Ni-Cr alloy SS308 in the both thermal and fast neutron spectrum

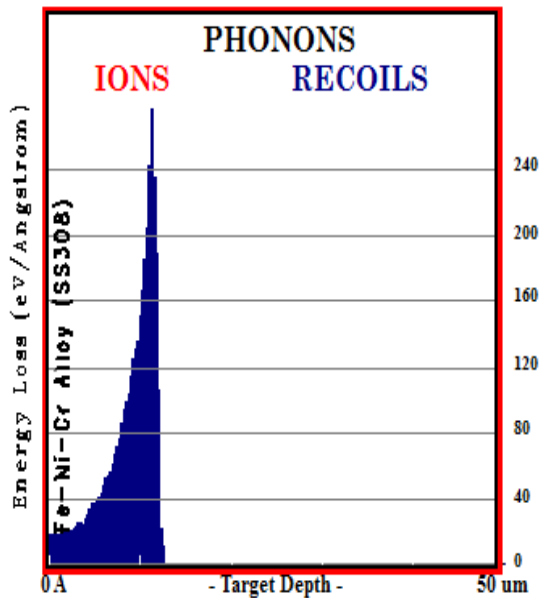


Fig 4.17 (a)

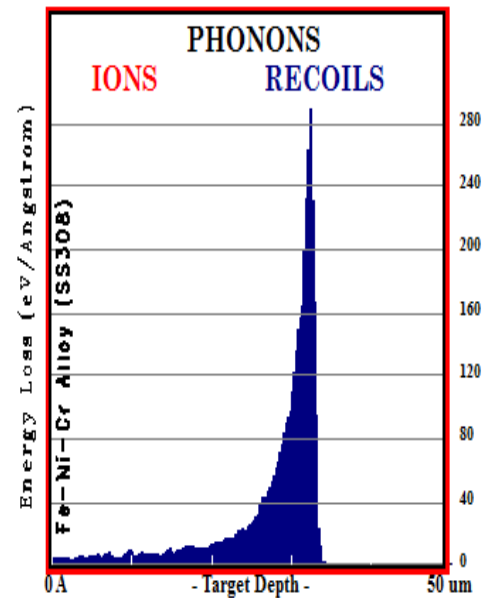


Fig 4.17 (b)

Fig 4.17: Distribution of Energy Loss as Phonons by the Fe-Ni-Cr Alloy SS308 in the (a) thermal and (b) fast neutron spectrum

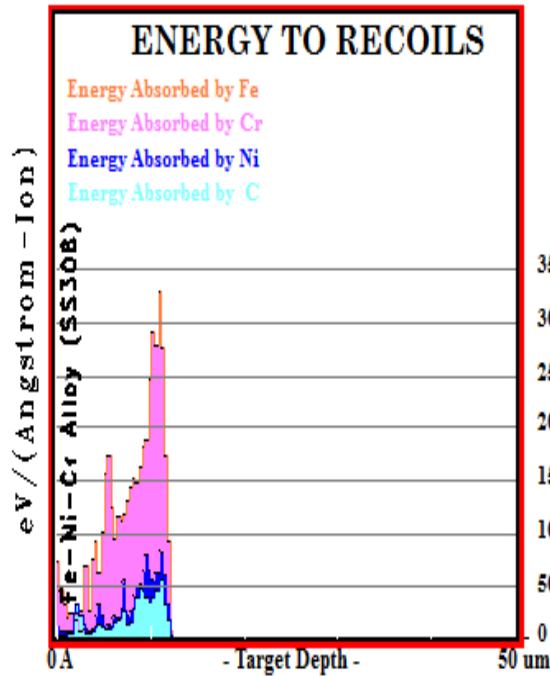


Fig. 4.18(a)

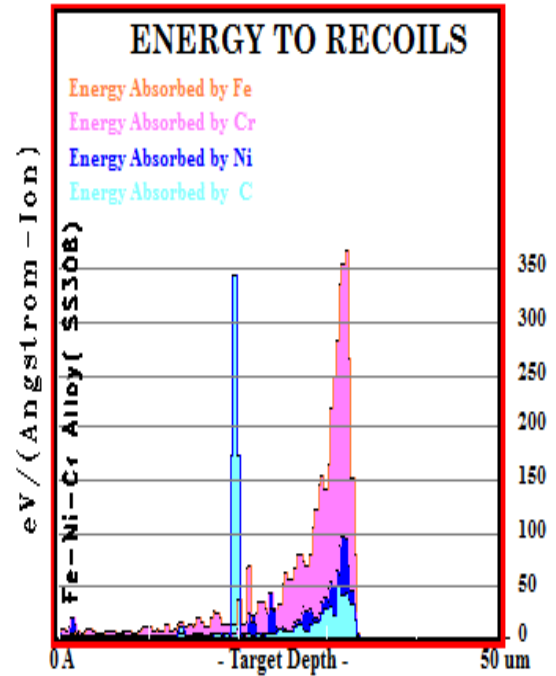


Fig. 4.18(b)

Fig 4.18: Plot of Energy absorbed by each element in the SS308 in the (a) thermal and (b) fast neutron spectrum.

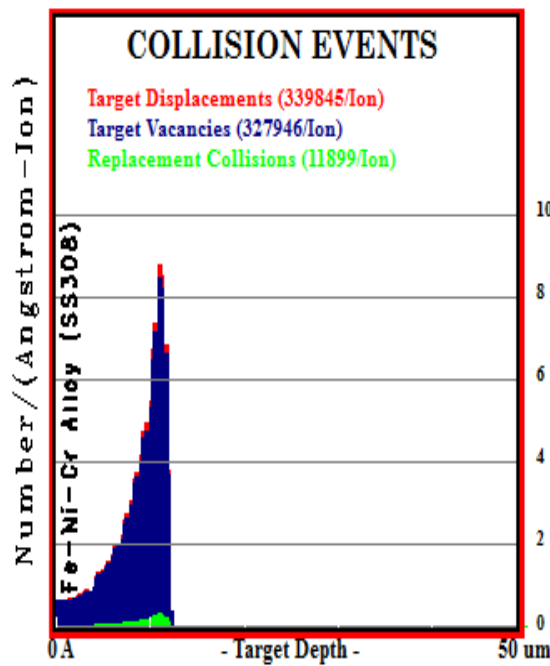


Fig 4.19(a)

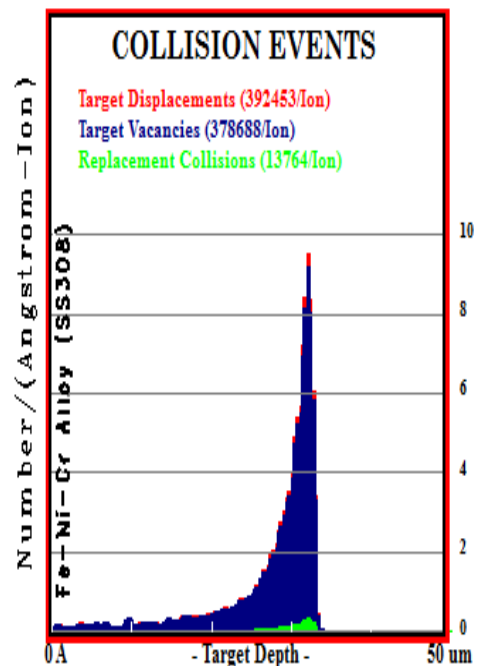


Fig 4.19(b)

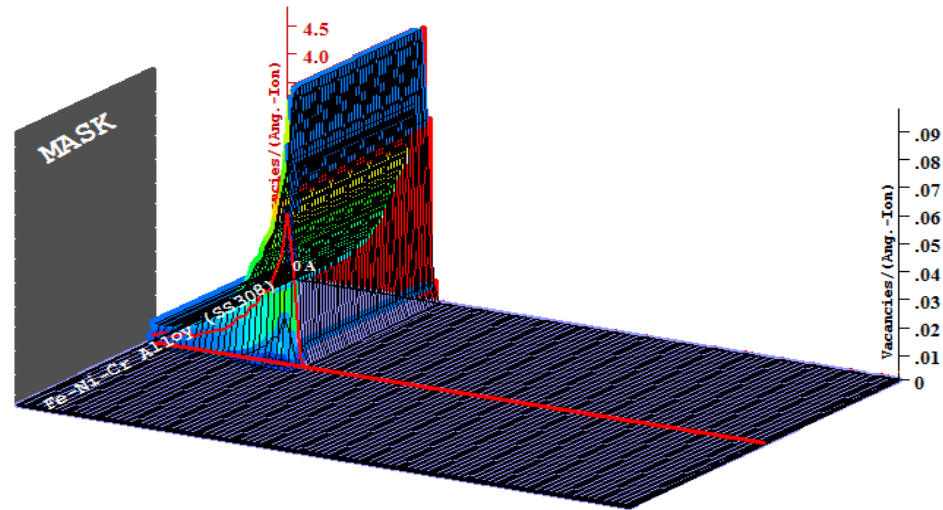


## Target Vacancies

Total Displacements = 339845 / Ion

Total Vacancies = 327946 / Ion

Replacement Collisions = 11899 / Ion



Plot Window goes from 0 Å to 50  $\mu\text{m}$ ; cell width = 5000 Å.  
Press PAUSE TRIM to speed plots. Rotate plot with Mouse.

**Ion = U (365. MeV)**

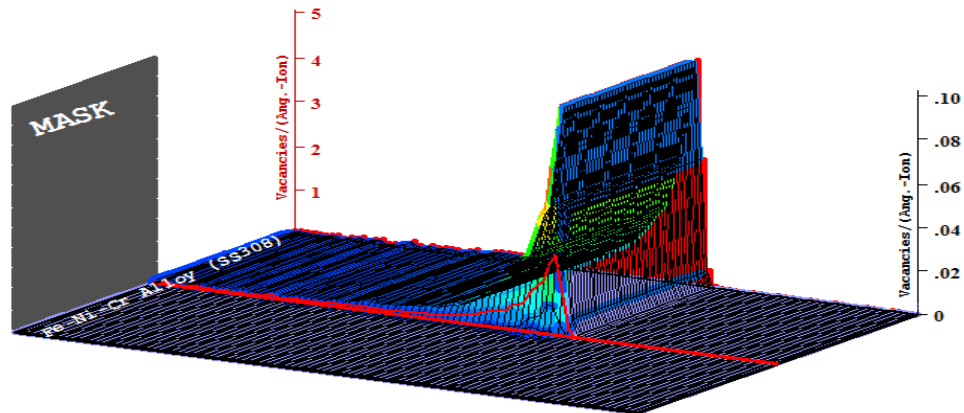
Fig 4.19(c)

## Target Vacancies

Total Displacements = 392453 / Ion

Total Vacancies = 378688 / Ion

Replacement Collisions = 13764 / Ion



Plot Window goes from 0 Å to 50  $\mu\text{m}$ ; cell width = 5000 Å.  
Press PAUSE TRIM to speed plots. Rotate plot with Mouse.

**Ion = U (1820. MeV)**

Fig 4.19(d)

Fig 4.19: Collision events of SS308 in 2D and 3D view respectively in the thermal and fast neutron spectrum



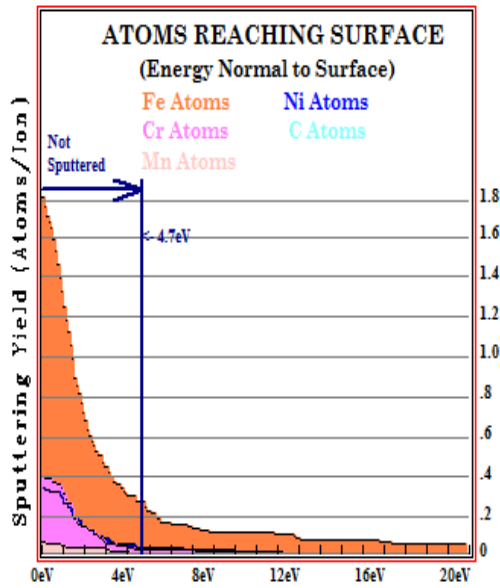


Fig 4.20(a)

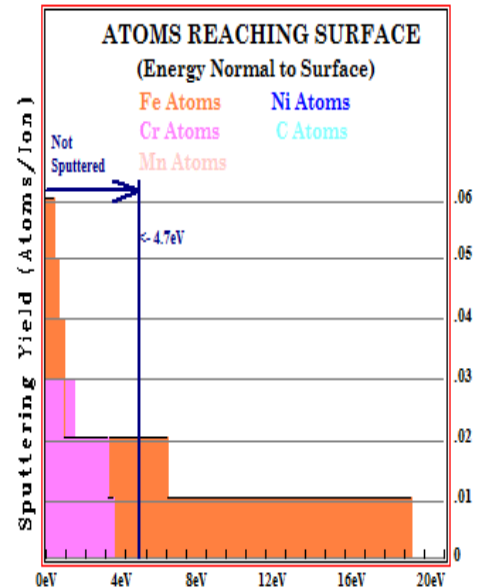


Fig 4.20(b)

Fig 4.20: Plots of integral sputtering yield of SS308 in (a) thermal and (b) fast neutron spectrum

ii) SS309

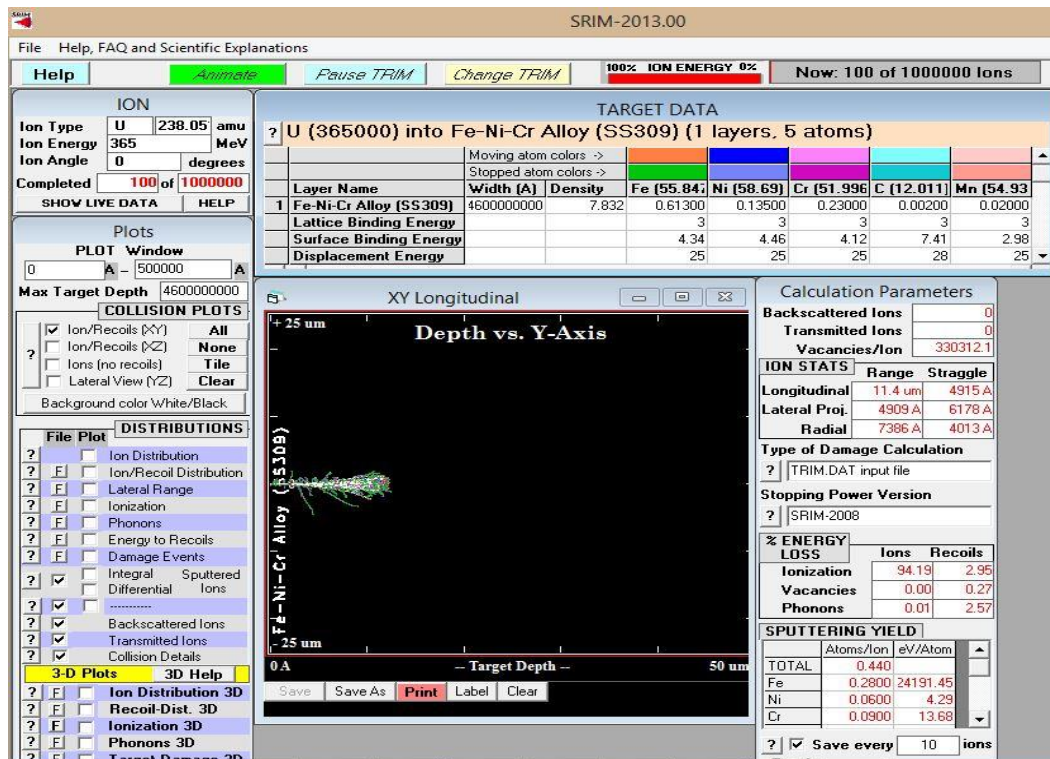


Fig. 4.21(a)

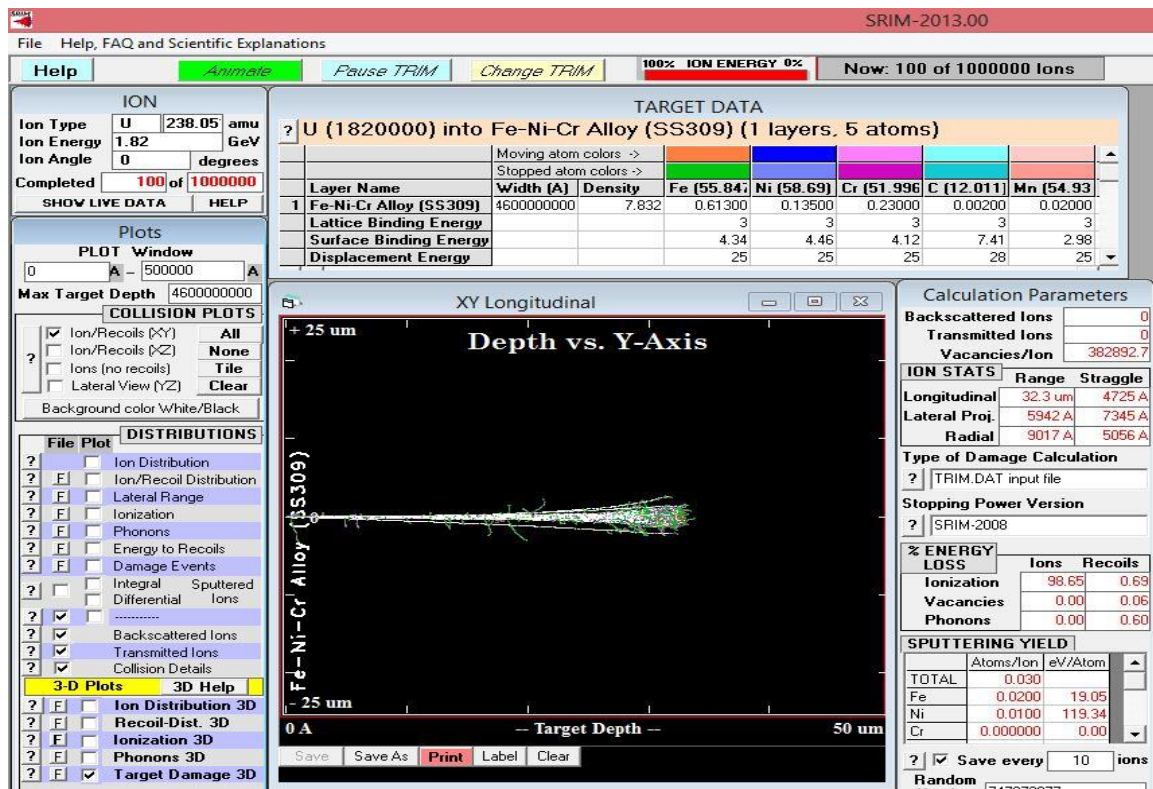


Fig 4.21(b)

Fig. 4.21: Collision cascades for (a) thermal and (b) fast neutron irradiation damage in S309

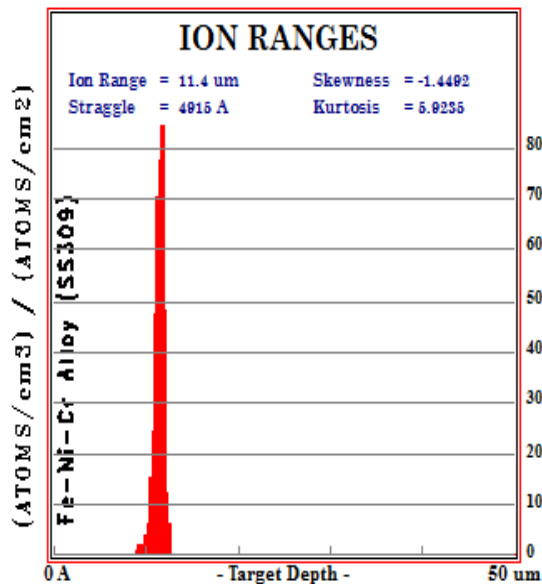


Fig 4.22 (a)

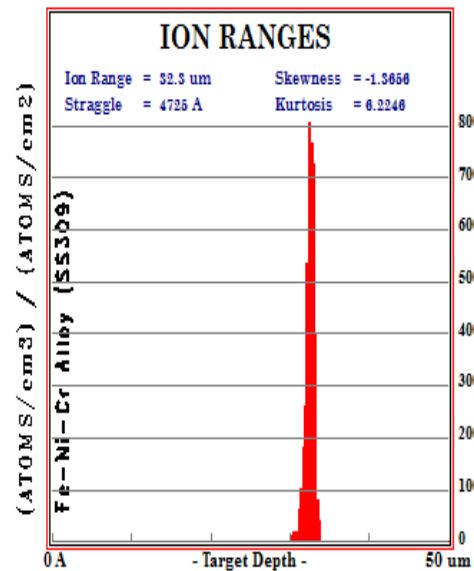


Fig 4.22 (b)

Fig 4.22: Depth of penetration of (a) thermal and (b) fast neutron in the SS309

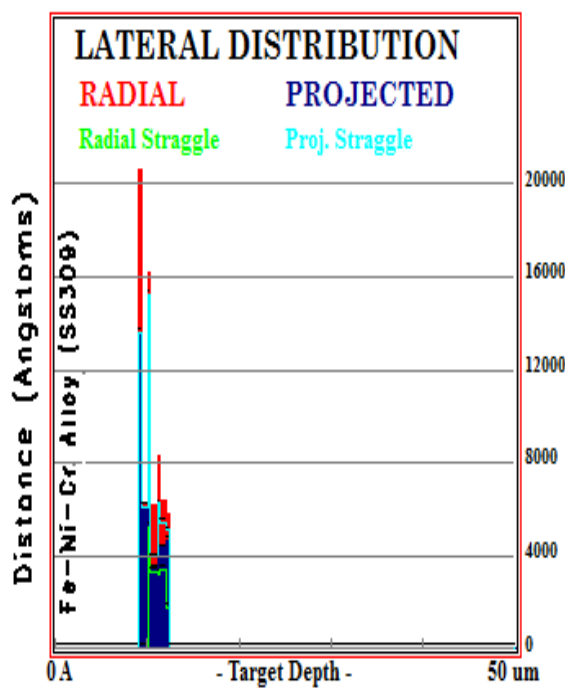


Fig 4.23(a)

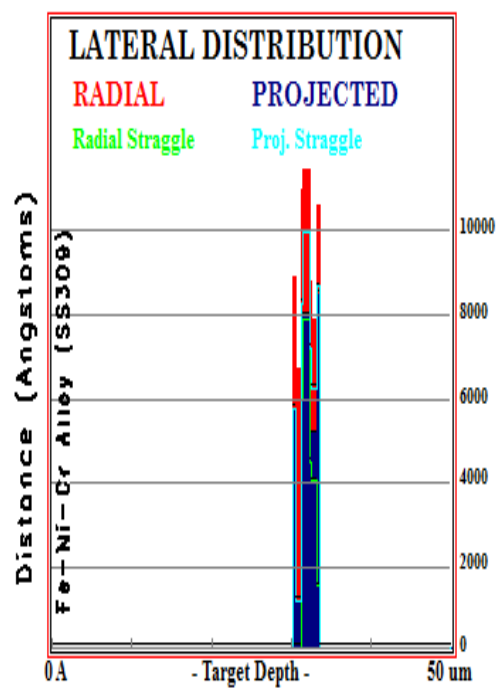


Fig 4.23(b)

Fig 4.23: Lateral Range Distribution of (a) thermal and (b) fast neutron in the SS309

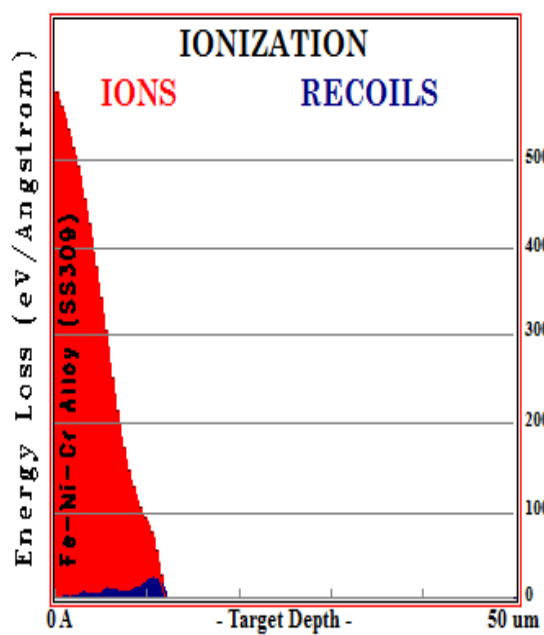


Fig 4.24(a)

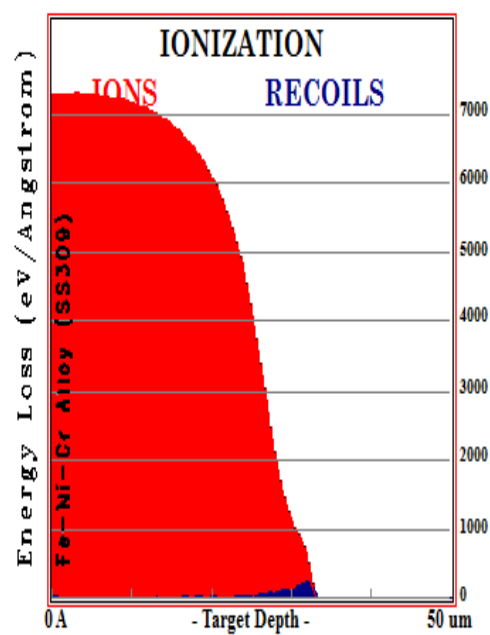


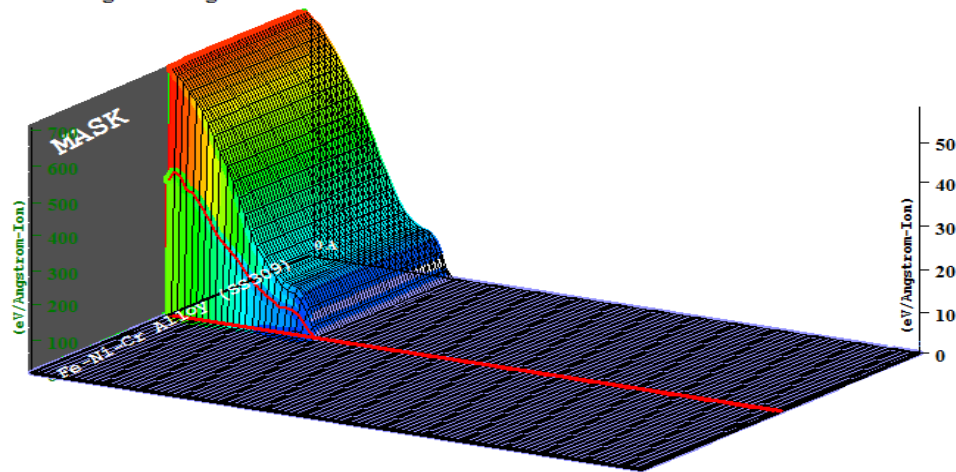
Fig 4.24(b)

## Target Ionization

Total Ionization = 354573.1 keV / Ion

Total Phonons = 9436.3 keV / Ion

Total Target Damage = 990.59 keV / Ion



Plot Window goes from 0 A to 50 um; cell width = 5000 A  
Press PAUSE TRIM to speed plots. Rotate plot with Mouse.

**Ion = U (365. MeV)**

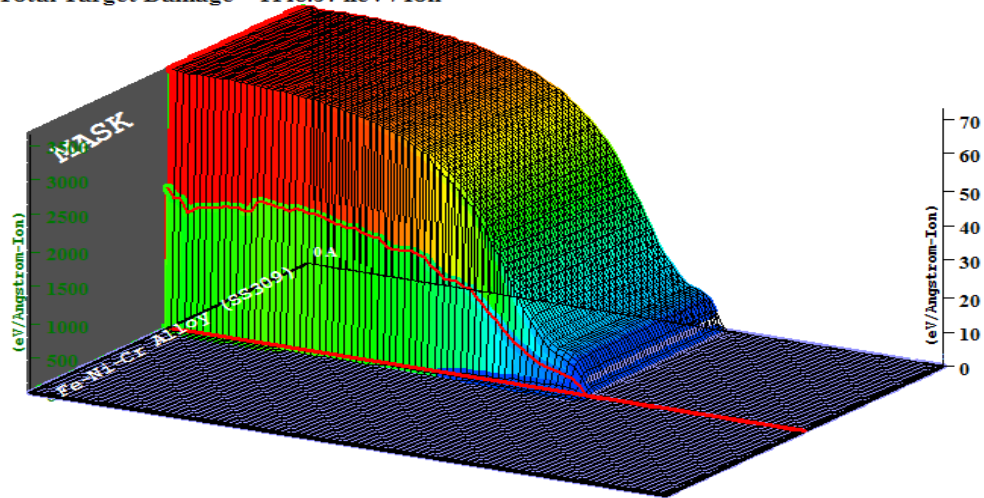
Fig. 4.24(c)

## Target Ionization

Total Ionization = 1807878.1 keV / Ion

Total Phonons = 10973.3 keV / Ion

Total Target Damage = 1148.57 keV / Ion



Plot Window goes from 0 A to 50 um; cell width = 5000 A  
Press PAUSE TRIM to speed plots. Rotate plot with Mouse.

**Ion = U (1820. MeV)**

Fig. 4.24(d)

Fig 4.24: 2D and 3D view of Ionization energy distribution of the Fe-Ni-Cr alloy SS309 in the thermal and fast4neutron spectrum

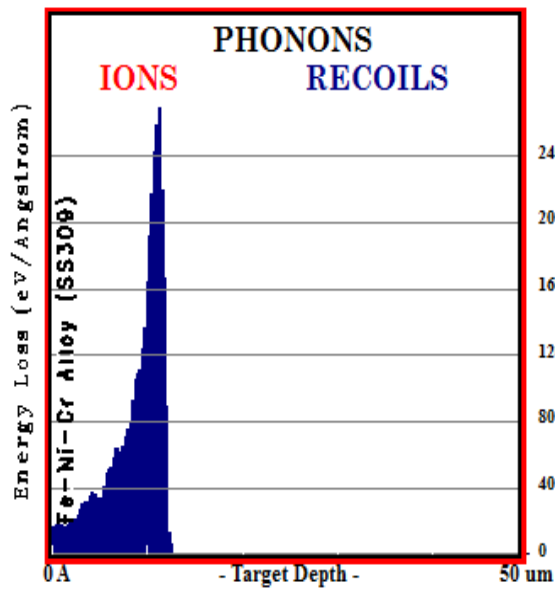


Fig 4.25(a)

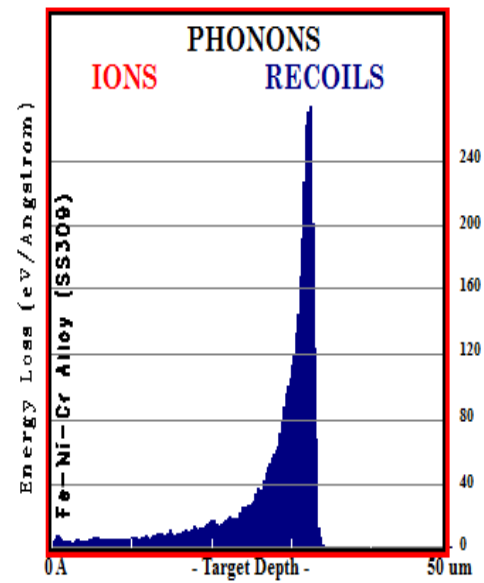


Fig 4.25(b)

Fig 4.25: The Distribution of Energy Loss as Phonons by the Fe-Ni-Cr Alloy SS309 in the (a) thermal and (b) fast neutron irradiation

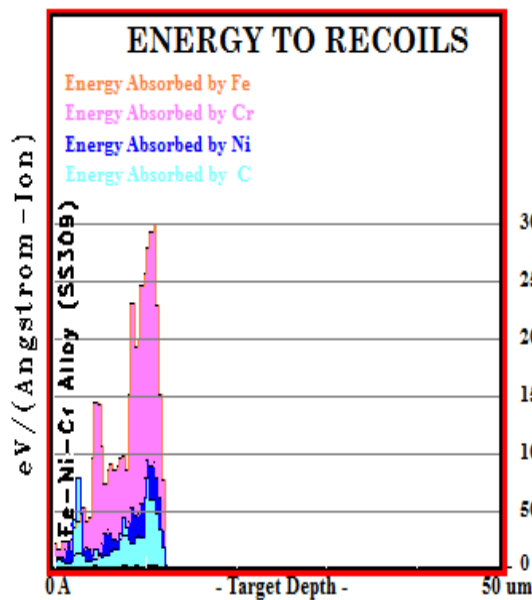


Fig. 4.26(a)

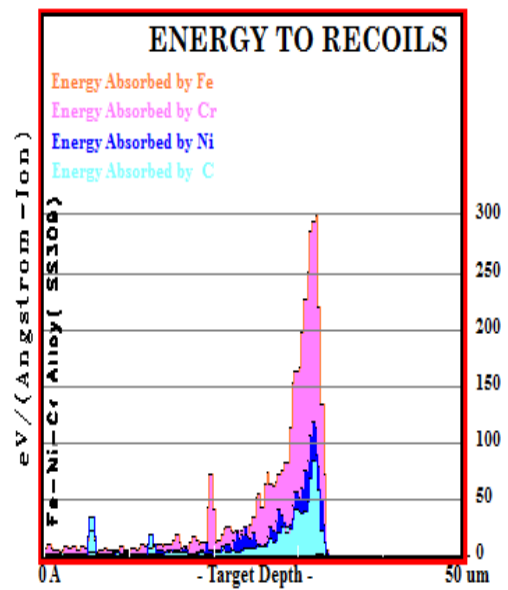


Fig. 4.26(b)

Fig 4.26: Plot of energy absorbed by elements of the SS309 Fe-Ni-Cr Alloys in the (a) thermal and (b) fast neutron spectrum.

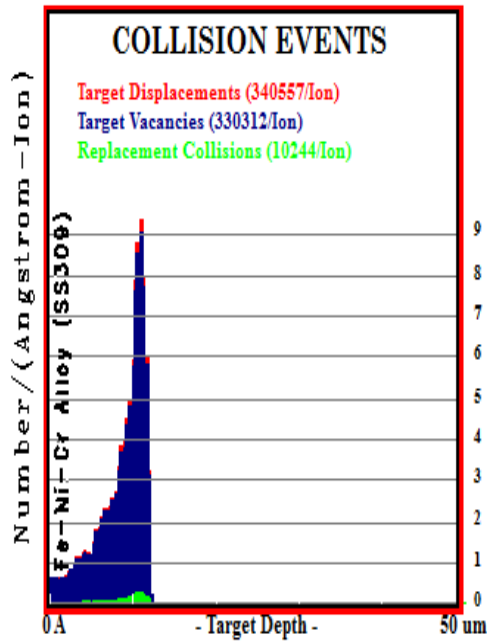


Fig 4.27(a)

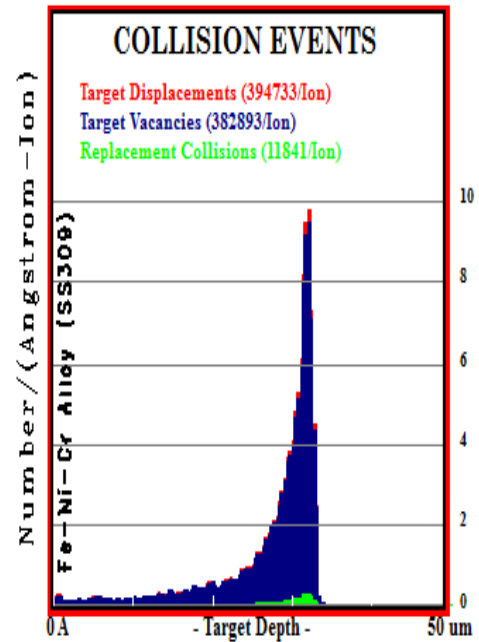


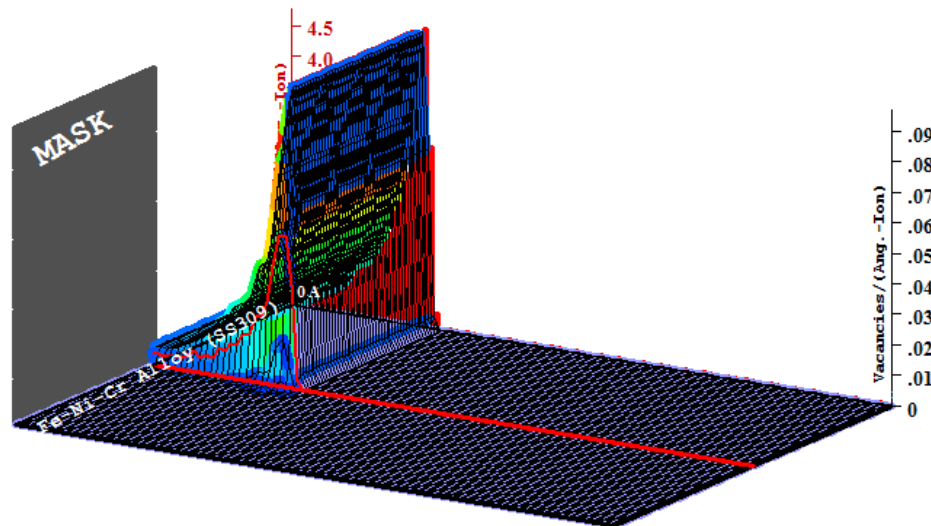
Fig 4.27(b)

## Target Vacancies

Total Displacements = 340557 / Ion

Total Vacancies = 330312 / Ion

Replacement Collisions = 10244 / Ion



Plot Window goes from 0 A to 50 um; cell width = 5000 A  
Press PAUSE TRIM to speed plots. Rotate plot with Mouse.

**Ion = U (365. MeV)**

Fig. 4.27(c)

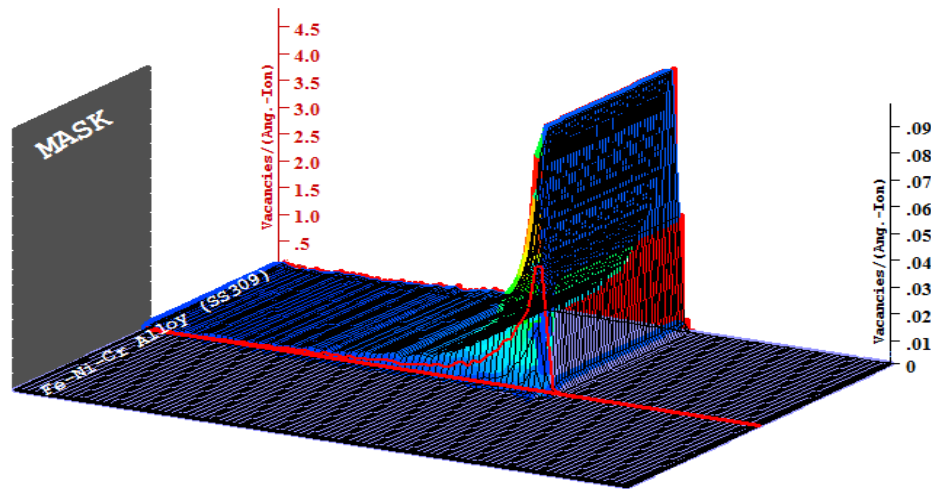


## Target Vacancies

Total Displacements = 394733 / Ion

Total Vacancies = 382893 / Ion

Replacement Collisions = 11841 / Ion



Plot Window goes from 0 Å to 50  $\mu\text{m}$ ; cell width = 5000 Å  
Press PAUSE TRIM to speed plots. Rotate plot with Mouse.

**Ion = U (1820. MeV)**

Fig 4.27(d)

Fig. 4.27: Collision events of SS309 in 2D and 3D view in the thermal and fast neutron spectrum

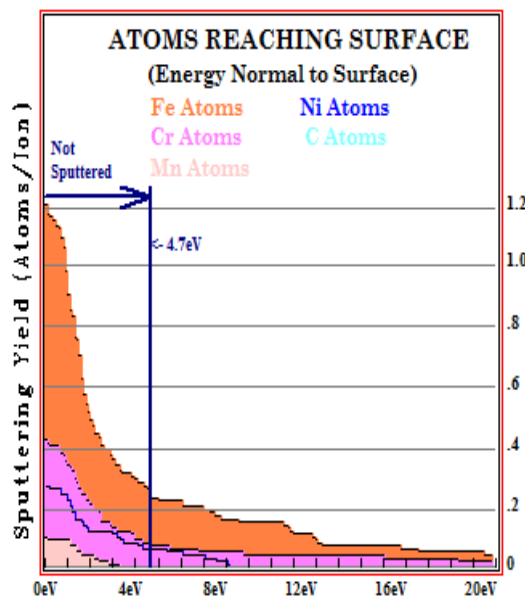


Fig 4.28(a)

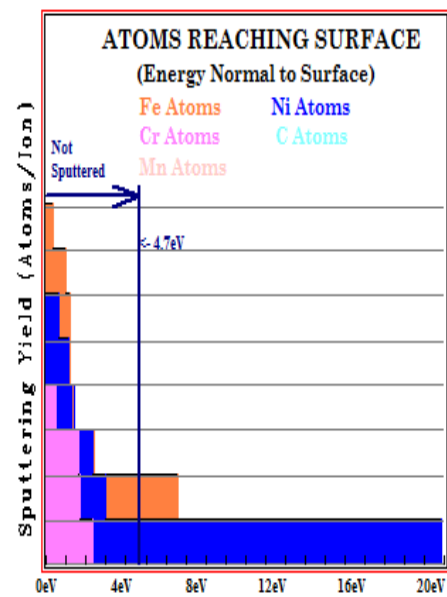


Fig 4.28(b)

Fig 4.28: Plot of integral sputtering yield of SS309 in both spectrum

iii) SS316

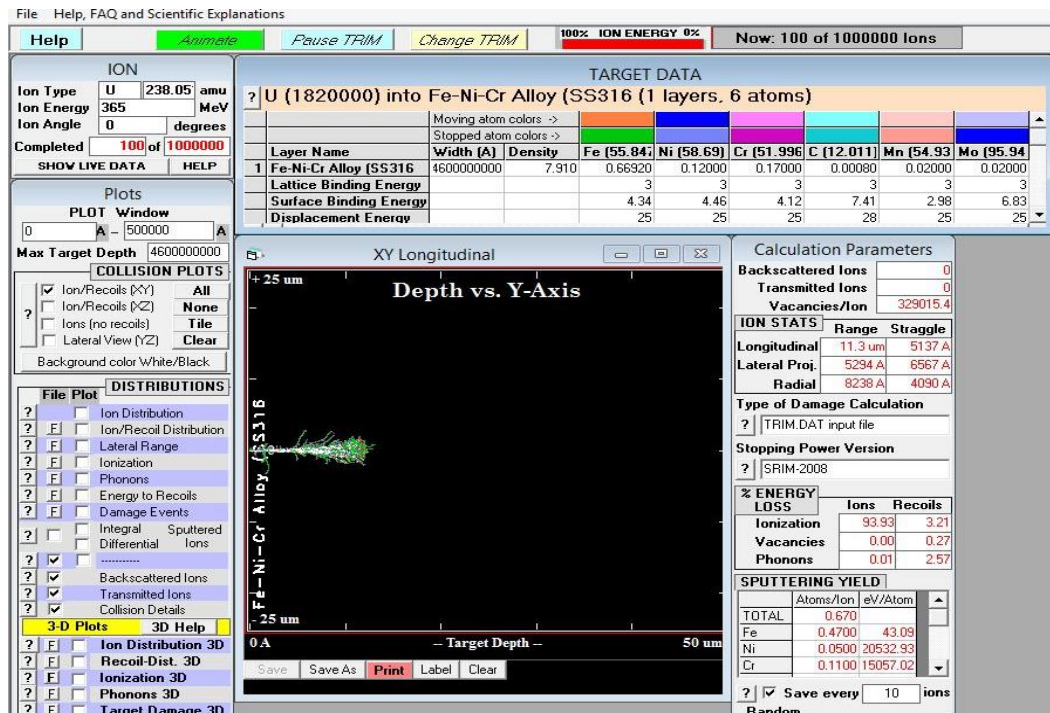


Fig. 4.29 (a)

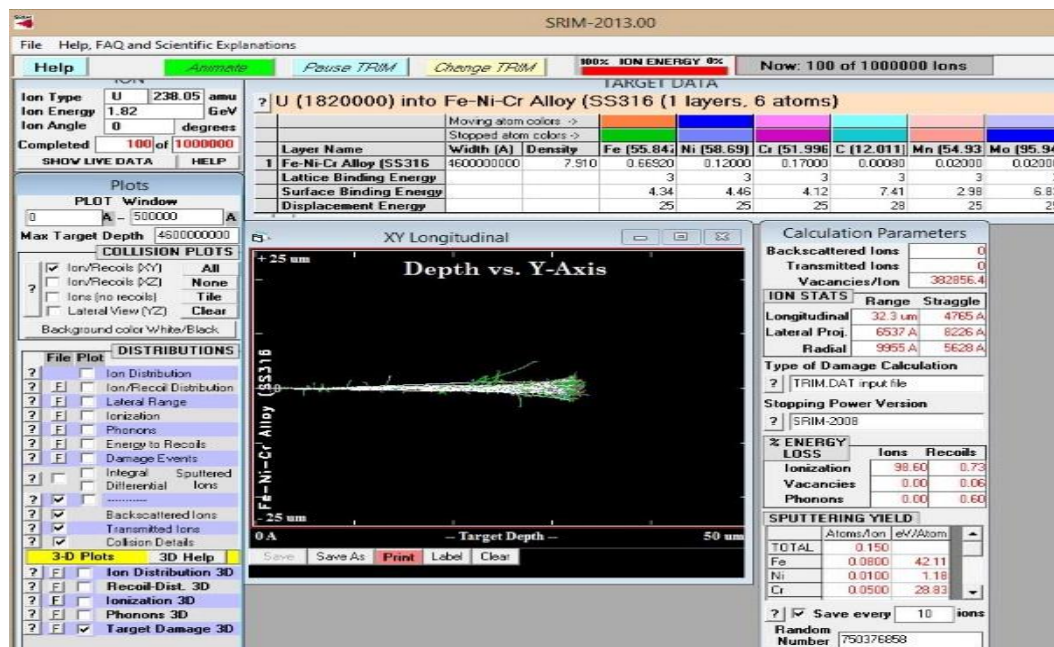


Fig 4.29(b)

Fig. 29: Collision Cascade for (a) thermal and fast neutron irradiation damage in Fe-Ni-Cr alloy SS316



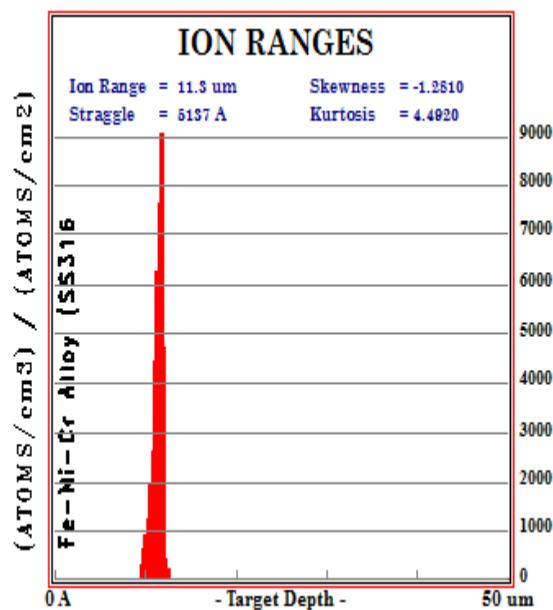


Fig 4.30 (a)

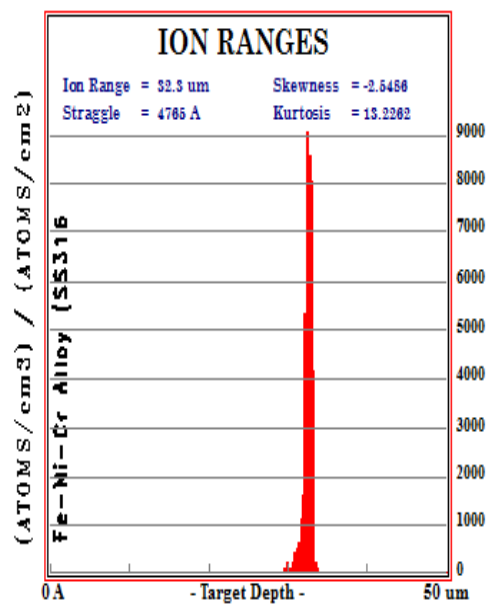


Fig 4.30(b)

Fig 4.30: Projected Range Distribution of (a) thermal and (b) fast neutron in the Fe-Ni-Cr Alloy SS316

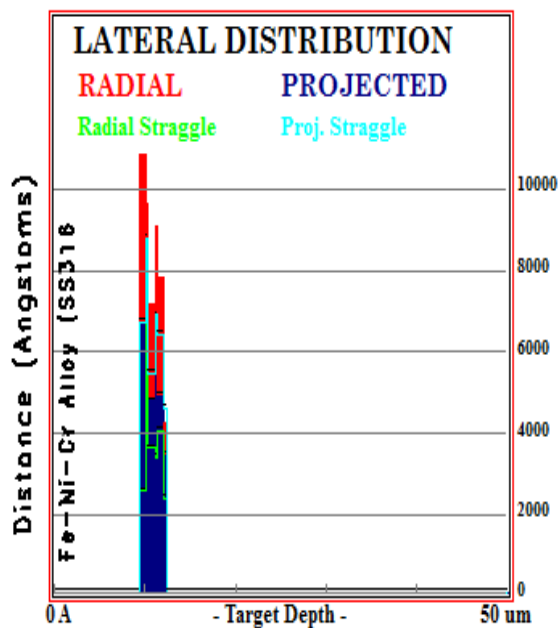


Fig 4.31(a)

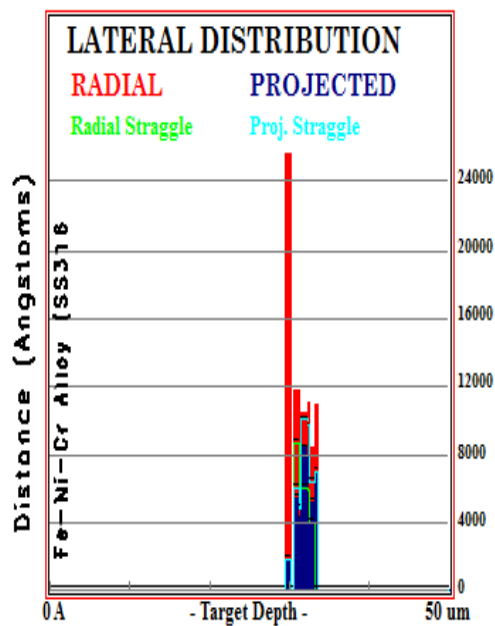


Fig 4.31(b)

Fig 4.31: Lateral Range Distribution of (a) thermal and (b) fast neutrons in SS316

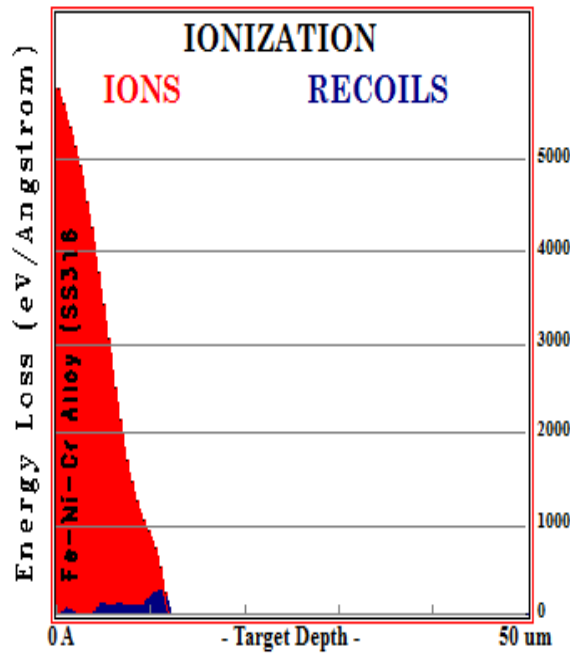


Fig 4.32(a)

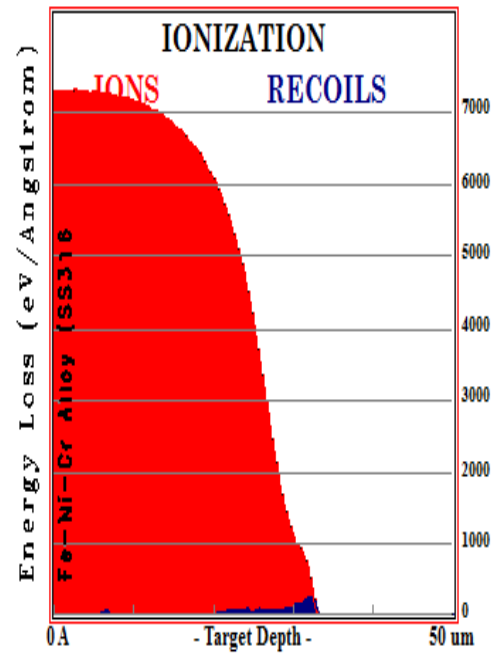


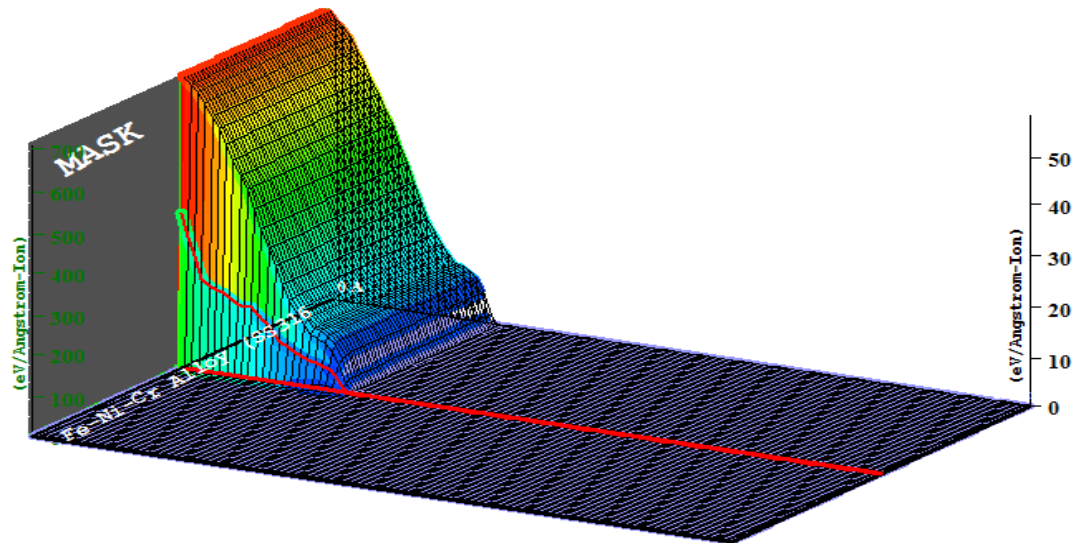
Fig 4.32(b)

## Target Ionization

Total Ionization = 354586.6 keV / Ion

Total Phonons = 9426.7 keV / Ion

Total Target Damage = 986.71 keV / Ion



Plot Window goes from 0 A to 50 um; cell width = 5000 A.  
Press PAUSE TRIM to speed plots. Rotate plot with Mouse.

**Ion = U (365. MeV)**

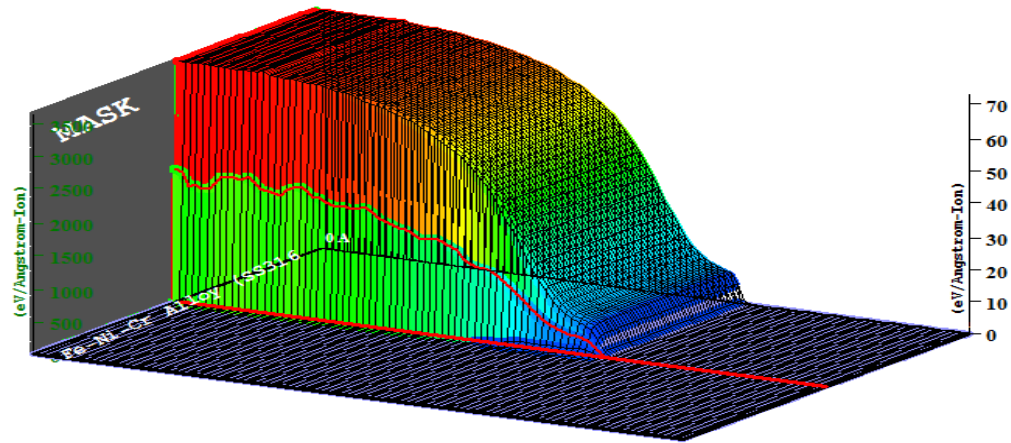
Fig 4.32(c)

## Target Ionization

Total Ionization = 1807847.4 keV / Ion

Total Phonons = 11004.2 keV / Ion

Total Target Damage = 1148.46 keV / Ion



Plot Window goes from 0 A to 50 um; cell width = 5000 A  
Press PAUSE TRIM to speed plots. Rotate plot with Mouse.

**Ion = U (1820. MeV)**

Fig 4.32(d)

Fig 4.32: 2D and 3D view of Ionization energy distribution of SS316 in the thermal and fast neutron spectrum

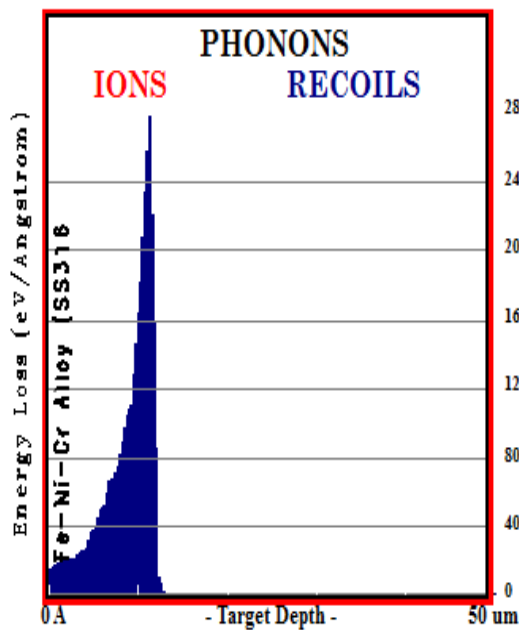


Fig 4.33(a)

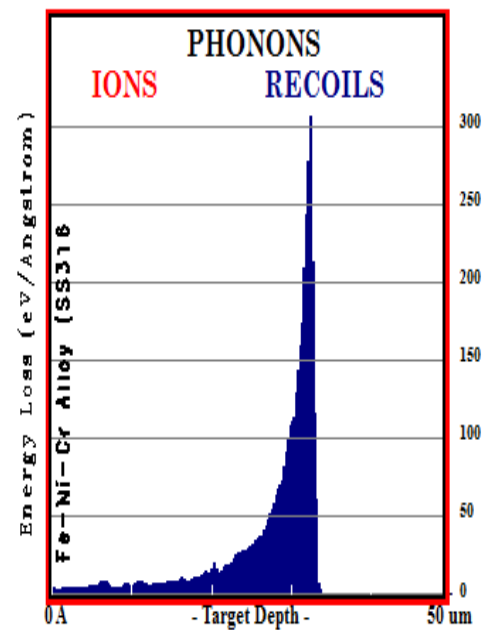


Fig 4.33(b)

Fig 4.33: The Distribution of Energy Loss as Phonons in SS316 by (a) thermal and (b) fast neutron irradiation

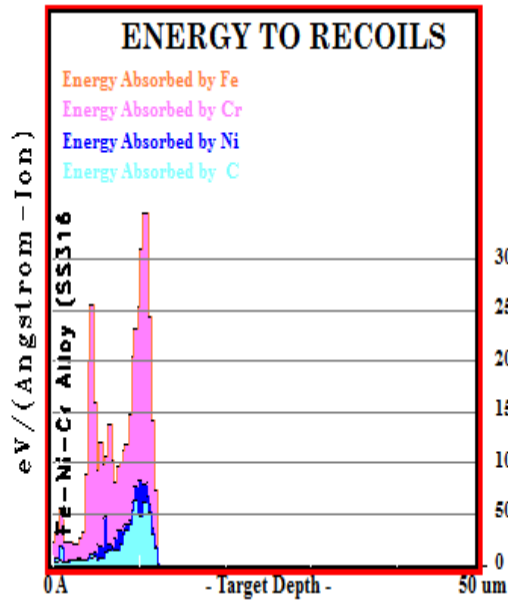


Fig 4.34(a)

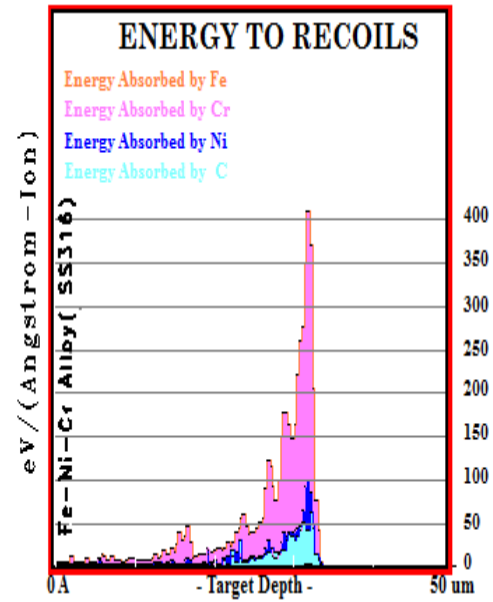


Fig 4.34(b)

Fig 4.34: Plots of energy absorbed by elements in the SS309 in the (c) thermal and (d) fast neutron spectrum.

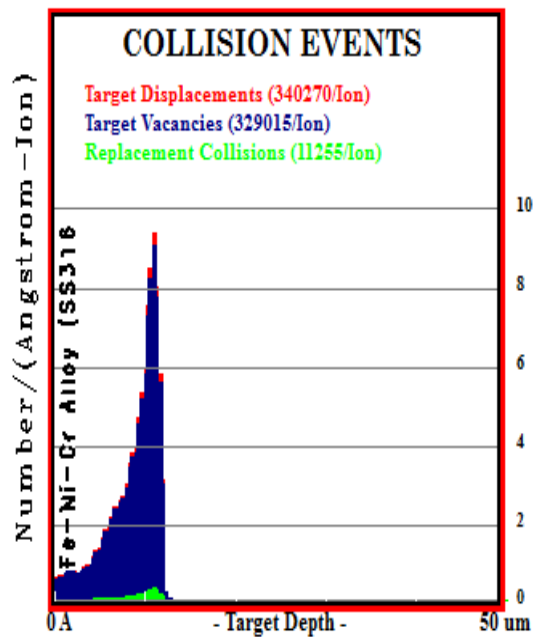


Fig 4.35(a)

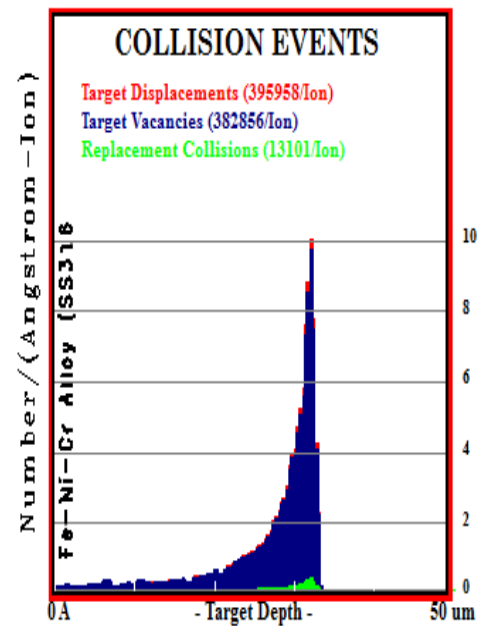


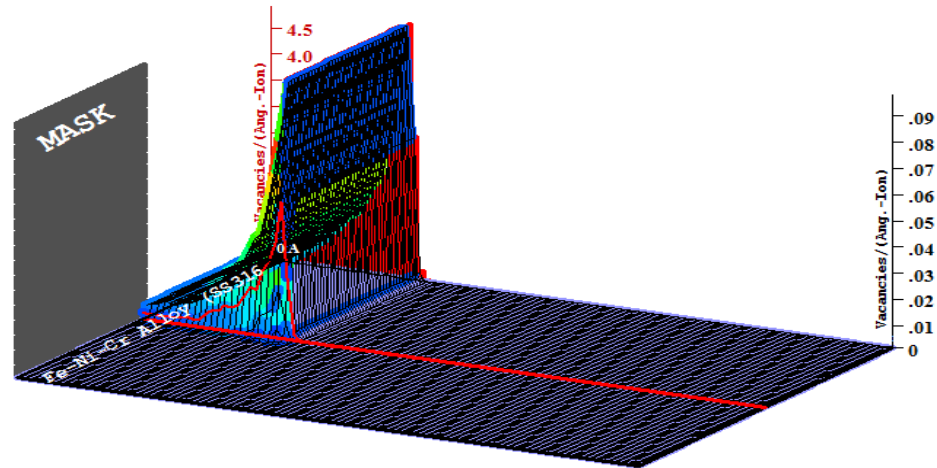
Fig 4.35(b)

## Target Vacancies

Total Displacements = 340270 / Ion

Total Vacancies = 329015 / Ion

Replacement Collisions = 11255 / Ion



Plot Window goes from 0 A to 50 um; cell width = 5000 A  
Press PAUSE TRIM to speed plots. Rotate plot with Mouse.

**Ion = U (365. MeV)**

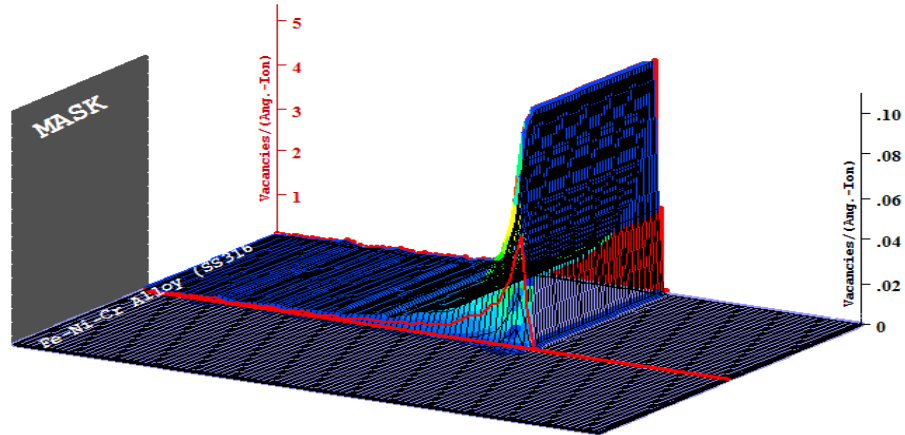
Fig 4.35(c)

## Target Vacancies

Total Displacements = 395958 / Ion

Total Vacancies = 382856 / Ion

Replacement Collisions = 13101 / Ion



Plot Window goes from 0 A to 50 um; cell width = 5000 A  
Press PAUSE TRIM to speed plots. Rotate plot with Mouse.

**Ion = U (1820. MeV)**

Fig 4.35(d)

Fig 4.35: Collision events of SS316 in 2D and 3D view in the thermal and fast neutron spectrum

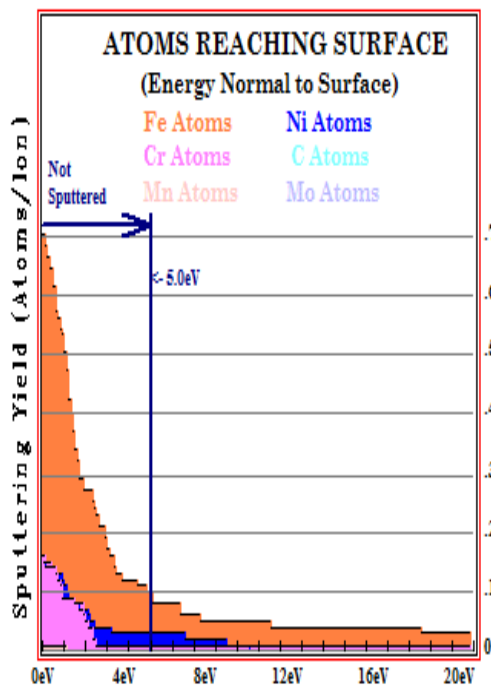


Fig 4.36(a)

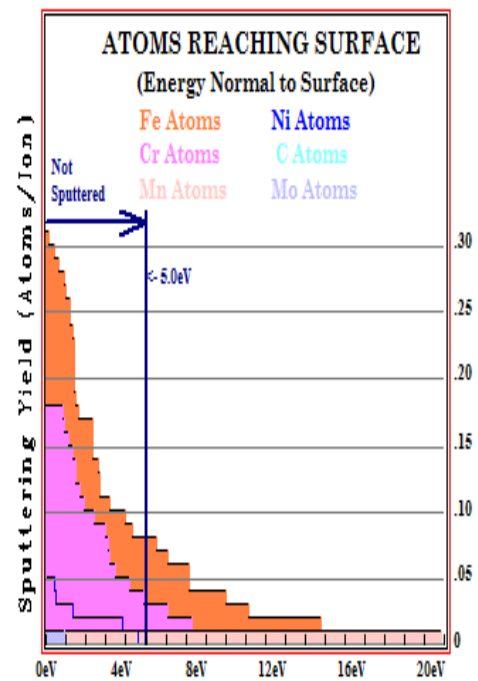


Fig 4.36(b)

Fig 4.36: Plots of integral sputtering yield of SS316 in both spectrum

## APPENDIX V

### Comparison of the Irradiation Damage of All Fe-Ni-Cr Alloys Both under Thermal and Fast Neutron Spectrum of the SCWR

DAMAGE TYPE	THERMAL NEUTRON SPECTRUM				FAST NEUTRON SPECTRUM			
	SS304	SS308	SS309	SS316	SS304	SS308	SS309	SS316
<b>Ion Projected Range in Target (<math>\mu\text{m}</math>)</b>	11.3	11.3	11.4	11.3	32.3	32.4	32.3	32.3
<b>Target Displacement (/Ion)</b>	337242	339845	340557	340270	394519	392453	394733	395958
<b>Replacement Collisions (/Ion)</b>	11963	11899	10244	11255	13991	13764	11841	13101
<b>Target Vacancies (/Ion)</b>	325279	327946	330312	329015	380528	378688	382893	382856
<b>Ion's Energy to the Target Electrons (Ionization) (keV/Ion)</b>	354684.3 (97.18%)	354607.7 (97.15%)	354573.1 (97.14%)	354586.6 (97.14%)	1807893.2 (99.33%)	1807965.8 (99.34%)	1807878.1 (99.34%)	1807847.4 (99.33%)
<b>Ion's Energy loss to the Target Phonons (keV/Ion)</b>	9340.3 (2.56%)	9408.8 (2.58%)	9436.3 (2.58%)	9426.7 (2.58%)	10965.3 (0.60%)	10898.2 (0.60%)	10973.3 (0.60%)	11004.2 (0.60%)
<b>Total Target Damage Energy (keV/Ion)</b>	983.13 (0.26%)	983.48 (0.27%)	990.59 (0.27%)	986.71 (0.27%)	1141.47 (0.06%)	1135.95 (0.06%)	1148.57 (0.06%)	1148.46 (0.06%)
<b>Sputtering Yield (Atoms/Ion)</b>	0.190	0.380	0.440	0.670	0.100	0.020	0.030	0.150

## APPENDIX VI

### Output Files of Molecular Dynamics Simulation of Mechanical Damage Assessment

#### a) Cohesive energy and equilibrium lattice parameter simulation output file

```

LAMMPS (30 Sep 2014-ICMS)
WARNING: OMP_NUM_THREADS environment is not set. (./comm.cpp:88)
  using 1 OpenMP thread(s) per MPI task
# Determination of the cohesive energy and equilibrium lattice constants of the FeNiCr.eam.alloy potential wit fcc
configuration Adapted from Mark Tschopp, 2010

#By Collins Nana Andoh(10443957)
# ----- Initialize Simulation -----
clear
WARNING: OMP_NUM_THREADS environment is not set. (./comm.cpp:88)
  using 1 OpenMP thread(s) per MPI task
units metal
dimension 3
boundary p p p
atom_style atomic
atom_modify map array
# ----- Create Atoms -----
lattice fcc 4
Lattice spacing in x,y,z = 4 4 4
region box block 0 1 0 1 0 1 units lattice
create_box 1 box
Created orthogonal box = (0 0 0) to (4 4 4)
  1 by 1 by 1 MPI processor grid

lattice fcc 4 orient x 1 0 0 orient y 0 1 0 orient z 0 0 1
Lattice spacing in x,y,z = 4 4 4
create_atoms 1 box
Created 4 atoms
replicate 1 1 1
  orthogonal box = (0 0 0) to (4 4 4)
  1 by 1 by 1 MPI processor grid
  4 atoms
# ----- Define Interatomic Potential -----
pair_style eam/alloy
pair_coeff * * FeNiCr.eam.alloy.u3 Fe
neighbor 2.0 bin
neigh_modify delay 10 check yes
# ----- Define Settings -----
compute eng all pe/atom
compute eatoms all reduce sum c_eng
# ----- Run Minimization -----
reset_timestep 0.001
fix 1 all box/relax iso 0.0 vmax 0.001
thermo 10
thermo_style custom step pe lx ly lz press pxx pyy pzz c_eatoms
min_style cg
minimize 1e-25 1e-25 5000 100000
WARNING: Resetting reneighboring criteria during minimization (./min.cpp:168)
Memory usage per processor = 3.4108 Mbytes
Step PotEng Lx Ly Lz Press Pxx Pyy Pzz c_eatoms
  0 -14.730235      4      4      4 -94068.38 -94068.38 -94068.38 -94068.38 -14.730235
 10 -14.844402    3.96    3.96    3.96 -99515.996 -99515.996 -99515.996 -99515.996 -14.844402
 20 -14.966592    3.92    3.92    3.92 -111956.11 -111956.11 -111956.11 -111956.11 -14.966592
 30 -15.106693    3.88    3.88    3.88 -136808.6 -136808.6 -136808.6 -136808.6 -15.106693
 40 -15.280204    3.84    3.84    3.84 -175730.14 -175730.14 -175730.14 -175730.14 -15.280204
 50 -15.492881    3.8    3.8    3.8 -210627.33 -210627.33 -210627.33 -210627.33 -15.492881
 60 -15.725423    3.76    3.76    3.76 -218502.3 -218502.3 -218502.3 -218502.3 -15.725423
 70 -15.945101    3.72    3.72    3.72 -196772.77 -196772.77 -196772.77 -196772.77 -15.945101

```



```

      80 -16.128136    3.68    3.68    3.68 -158787.1 -158787.1 -158787.1 -158787.1 -16.128136
      90 -16.267326    3.64    3.64    3.64 -118869.93 -118869.93 -118869.93 -118869.93 -16.267326
     100 -16.365806    3.6    3.6    3.6 -82373.473 -82373.473 -82373.473 -82373.473 -16.365806
     110 -16.429061    3.56    3.56    3.56 -49883.162 -49883.162 -49883.162 -49883.162 -16.429061
     120 -16.461675    3.52    3.52    3.52 -19192.249 -19192.249 -19192.249 -19192.249 -16.461675
     130 -16.466526  3.4986965  3.4986965  3.4986965 1.3519338e-009 1.3509121e-009 1.3550405e-009 1.3498488e-009 -
16.466526

```

Loop time of 0.0636024 on 1 procs for 130 steps with 4 atoms  
73.7% CPU use with 1 MPI tasks x 1 OpenMP threads

#### Minimization stats:

Stopping criterion = energy tolerance  
Energy initial, next-to-last, final =  
-14.730235479 -16.4665256808 -16.4665256808  
Force two-norm initial, final = 11.2729 1.25995e-013  
Force max component initial, final = 11.2729 1.23948e-013  
Final line search alpha, max atom move = 1 1.23948e-013  
Iterations, force evaluations = 130 135

#### MPI task timings breakdown:

Section	min time	avg time	max time	%varavg	%total
Pair	0.013032	0.013032	0.013032	0.0	20.49
Neigh	0	0	0	0.0	0.00
Comm	0.0016911	0.0016911	0.0016911	0.0	2.66
Output	0.0054446	0.0054446	0.0054446	0.0	8.56
Modify	0	0	0	0.0	0.00
Other		0.04344			68.29

Nlocal: 4 ave 4 max 4 min  
Histogram: 1 0 0 0 0 0 0 0 0  
Nghost: 662 ave 662 max 662 min  
Histogram: 1 0 0 0 0 0 0 0 0  
Neighs: 496 ave 496 max 496 min  
Histogram: 1 0 0 0 0 0 0 0 0

Total # of neighbors = 496

Ave neighs/atom = 124

Neighbor list builds = 0

Dangerous builds = 0

run 0

Memory usage per processor = 2.42293 Mbytes

Step PotEng Lx Ly Lz Press Pxx Pyy Pzz eatoms

```

      130 -16.466526  3.4986965  3.4986965  3.4986965 1.3519338e-009 1.3509121e-009 1.3550405e-009 1.3498488e-009 -
16.466526

```

Loop time of 1.57894e-006 on 1 procs for 0 steps with 4 atoms  
0.0% CPU use with 1 MPI tasks x 1 OpenMP threads

#### MPI task timings breakdown:

Section	min time	avg time	max time	%varavg	%total
Pair	0	0	0	0.0	0.00
Neigh	0	0	0	0.0	0.00
Comm	0	0	0	0.0	0.00
Output	0	0	0	0.0	0.00
Modify	0	0	0	0.0	0.00
Other		1.579e-006			100.00

Nlocal: 4 ave 4 max 4 min  
Histogram: 1 0 0 0 0 0 0 0 0  
Nghost: 1094 ave 1094 max 1094 min  
Histogram: 1 0 0 0 0 0 0 0 0  
Neighs: 736 ave 736 max 736 min  
Histogram: 1 0 0 0 0 0 0 0 0

Total # of neighbors = 736

Ave neighs/atom = 184

Neighbor list builds = 0

Dangerous builds = 0

```
variable natoms equal "count(all)"
variable teng equal "c_eatoms"
variable teng equal "pe"
variable length equal "lx"
variable ecoh equal "v_teng/v_natoms"

print "Total energy (eV) = ${teng};"
Total energy (eV) = -16.4665256808311;
print "Number of atoms = ${natoms};"
Number of atoms = 4;
print "Lattice constant (Angstroms) = ${length};"
Lattice constant (Angstroms) = 3.49869654884664;
print "Cohesive energy (eV) = ${ecoh};"
Cohesive energy (eV) = -4.11663142020778;

print "All done!"
All done!
```

## b) A copy of the 16 Output Files from the Mechanical Damage Assessment

```
LAMMPS (30 Sep 2014-ICMS)
WARNING: OMP_NUM_THREADS environment is not set. (../comm.cpp:88)
  using 1 OpenMP thread(s) per MPI task
#      This program is aimed at evaluating the mechanical      #
#      integrity of (Youngs modulus, Ultimate tensile Strength, #
#      Fracture point)SS 308 treated under Ambient Temperature #
#      condition                                              #
#      Adapted from materials developed by Mark A. Tschopp   #
#      (US ARL) and hosted at https://icme.hpc.msstate.ed     #
#      Designed By:                                           #
#      Collins Nana Andoh                                     #
#      (10443957)                                             #
#      JULY 2015                                              #
#####

# ----- Initialize Simulation -----
clear
WARNING: OMP_NUM_THREADS environment is not set. (../comm.cpp:88)
  using 1 OpenMP thread(s) per MPI task
units      metal
dimension  3
boundary   p      p      p
atom_style atomic

# ----- Create Atoms -----
lattice    fcc 3.5918
Lattice spacing in x,y,z = 3.5918 3.5918 3.5918
region     new_region block 0 10 0 10 0 10
create_box 1 new_region
Created orthogonal box = (0 0 0) to (35.918 35.918 35.918)
  1 by 1 by 1 MPI processor grid
lattice    fcc 3.5918 orient x 1 0 0 orient y 0 1 0 orient z 0 0 1
Lattice spacing in x,y,z = 3.5918 3.5918 3.5918
create_atoms 1 region new_region
Created 4000 atoms
replicate  1 1 1
  orthogonal box = (0 0 0) to (35.918 35.918 35.918)
  1 by 1 by 1 MPI processor grid
  4000 atoms
# ----- Define Interatomic Potential -----
pair_style  eam/alloy
pair_coeff   * * FeNiCr.eam.alloy.u3 Fe
neighbor     2.0 bin
neigh_modify delay 0 every 10 check yes
# ----- Define Settings -----
compute     csym all centro/atom fcc
compute     eng all pe/atom
# ----- Equilibration-----
```

```

#reset timer
reset_timestep      0
#2 fs time step
timestep            0.002

#initial velocities
velocity            all create 300 12345 mom yes rot no
#thermostat + barostat (1 degree= 273 K and 1 MPa= 10 bar
fix                 1 all npt temp 300 300 1 iso 0 0 1 drag 1.0
# instrumentation and output
variable s1 equal "time"
variable s2 equal "lx"
variable s3 equal "ly"
variable s4 equal "lz"
variable s5 equal "vol"
variable s6 equal "press"
variable s7 equal "pe"
variable s8 equal "ke"
variable s9 equal "etotal"
variable s10 equal "temp"
fix writer all print 250 "${s1} ${s2} ${s3} ${s4} ${s5} ${s6} ${s7} ${s8} ${s9} ${s10}" #file Fe_eq.txt screen no
# thermo
thermo              500
thermo_style         custom step time cpu cpuremain lx ly lz press pe temp
#dumping trajectory
dump                1 all atom 250 dump.eq.lammpstrj
#24 ps MD Simulation (assuming 2 fs time step)
run 12000
Memory usage per processor = 3.83823 Mbytes
Step Time CPU CPULeft Lx Ly Lz Press PotEng Temp
0          0          0          0 35.918 35.918 35.918 -71838.912 -16381.467 300
500        1 18.584189 427.43641 35.034852 35.034852 35.034852 450.24634 -16387.164 161.01856
1000       2 36.363724 400.00099 35.040522 35.040522 35.040522 143.52865 -16381.732 173.20264
1500       3 57.872914 405.11042 35.047976 35.047976 35.047976 -740.27458 -16376.154 185.43939
2000       4 78.080024 390.40013 35.054911 35.054911 35.054911 -920.00382 -16372.052 200.44801
2500       5 96.593284 367.05449 35.053863 35.053863 35.053863 -510.4307 -16366.336 212.00241
3000       6 115.86609 347.59828 35.057679 35.057679 35.057679 -325.06191 -16360.184 222.06993
3500       7 133.09892 323.24025 35.055293 35.055293 35.055293 620.05444 -16355.15 233.37309
4000       8 147.4487 294.89741 35.058801 35.058801 35.058801 662.6319 -16349.486 242.27498
4500       9 163.50968 272.51614 35.060156 35.060156 35.060156 695.84364 -16347.193 256.23858
5000      10 180.13933 252.19506 35.073473 35.073473 35.073473 -396.87126 -16341.825 262.64355
5500      11 191.12924 225.88002 35.079207 35.079207 35.079207 -541.74259 -16338.201 270.64093
6000      12 197.72709 197.7271 35.079115 35.079115 35.079115 -55.798557 -16333.099 273.92674
6500      13 211.83854 179.248 35.068296 35.068296 35.068296 1470.9688 -16331.589 282.26106
7000      14 229.76504 164.11789 35.081638 35.081638 35.081638 392.05289 -16327.514 283.7951
7500      15 250.78482 150.47089 35.0801 35.0801 35.0801 369.02822 -16328.686 293.61679
8000      16 268.44122 134.22061 35.084015 35.084015 35.084015 48.125551 -16326.448 295.17463
8500      17 285.57829 117.59106 35.082331 35.082331 35.082331 231.76867 -16323.385 293.54886
9000      18 302.41941 100.80647 35.087561 35.087561 35.087561 -121.07472 -16322.314 294.26339
9500      19 319.33058 84.034366 35.092638 35.092638 35.092638 -1139.8359 -16325.895 302.6849
10000     20 336.19715 67.23943 35.082182 35.082182 35.082182 763.536 -16323.02 297.69095
10500     21 353.11178 50.44454 35.078052 35.078052 35.078052 873.88557 -16327.591 306.60518
11000     22 369.90504 33.627731 35.085554 35.085554 35.085554 365.48526 -16325.715 302.87981
11500     23 386.7937 16.817118 35.086145 35.086145 35.086145 -255.94453 -16323.474 298.43594
12000     24 403.63164 0 35.085311 35.085311 35.085311 -31.053508 -16324.877 301.05577

```

Loop time of 403.632 on 1 procs for 12000 steps with 4000 atoms  
 97.3% CPU use with 1 MPI tasks x 1 OpenMP threads  
 Performance: 5.137 ns/day 4.672 hours/ns 29.730 timesteps/s

#### MPI task timings breakdown:

Section	min time	avg time	max time	%varavg	%total
Pair	391.82	391.82	391.82	-1.5	97.07
Neigh	0.049093	0.049093	0.049093	-1.5	0.01
Comm	1.6115	1.6115	1.6115	0.0	0.40
Output	0.93485	0.93485	0.93485	0.0	0.23
Modify	8.6272	8.6272	8.6272	0.0	2.14
Other		0.5938			0.15

```

Nlocal: 4000 ave 4000 max 4000 min
Histogram: 1 0 0 0 0 0 0 0 0
Nghost: 8195 ave 8195 max 8195 min
Histogram: 1 0 0 0 0 0 0 0 0
Neighs: 347899 ave 347899 max 347899 min
Histogram: 1 0 0 0 0 0 0 0 0
FullNghs: 0 ave 0 max 0 min
Histogram: 1 0 0 0 0 0 0 0 0

Total # of neighbors = 347899
Ave neighs/atom = 86.9748
Neighbor list builds = 1
Dangerous builds = 0
#clearing fixes and dumps
unfix 1
undump 1
#saving equilibrium length for strain calculation
variable tmp equal "lx"
variable L0 equal ${tmp}
variable L0 equal 35.0853114166038
print "Initial Length, L0: ${L0}"
Initial Length, L0: 35.0853114166038
#-----DEFORMATION-----
#reset timer
reset_timestep 0
#2 fs time step
timestep 0.002
# thermostat + barostat
fix 1 all npt temp 300 300 1 y 0 0 1 z 0 0 1 drag 1.0
#nonequilibrium straining in x-direction at strain rate = 1x 10^10 / s = 1x10^2 / ps in units metal
#variable srate equal 1.0e10
variable srate1 equal 5e-3
fix 2 all deform 1 x erate ${srate1} units box remap x
fix 2 all deform 1 x erate 0.005 units box remap x
#instrumentation and output for units metal, pressure is in #[bars] = 100 [kPa] = 1/10000 [GPa] => p2, p3, p4, are in GPa
variable strain equal "(lx - v_L0)/v_L0"
variable p1 equal "v_strain"
variable p2 equal "-pxx/10000"
variable p3 equal "-pyy/10000"
variable p4 equal "-pzz/10000"
fix writer all print 125 "${p1} ${p2} ${p3} ${p4}" file Fe.deform.txt screen no
#thermo
thermo 1000
thermo_style custom step cpuremain v_strain v_p2 v_p3 v_p4 press pe temp

#dumping standard atom trajectories
dump 1 all atom 5000 dump.deform.lammpstrj

#dumping custom cfg files containing coords + ancillary variables
dump 2 all cfg 5000 dump.deform_*.cfg mass type xs ys zs c_csym c_eng fx fy fz
dump_modify 2 element Fe

#40 ps MD Simulation (assuming 2 fs time step)
run 20000
Memory usage per processor = 5.6434 Mbytes
Step CPULeft strain p2 p3 p4 Press PotEng Temp
0 0 0 -0.0076650229 -0.029189782 0.046170857 -31.053508 -16324.877 301.05577
1000 642.87472 0.01 1.2081609 0.111532 -0.027848267 -4306.1487 -16321.834 300.05982
2000 603.66976 0.02 2.8906892 0.019841745 0.058671507 -9897.3414 -16316.581 301.21928
3000 559.83536 0.03 5.0431753 0.0087265977 0.048737926 -17002.133 -16305.377 299.81327
4000 522.55349 0.04 7.1591005 -0.02937889 -0.002314307 -23758.024 -16287.932 298.94816
5000 487.08493 0.05 9.228635 -0.077490074 0.0048635651 -30520.028 -16260.929 294.19783
6000 452.56928 0.06 10.396876 0.15961449 0.11953291 -35586.744 -16230.937 297.02056
7000 419.60397 0.07 9.886064 -0.051682975 -0.09163781 -32475.811 -16201.752 303.20434
8000 386.75543 0.08 9.2446009 -0.083955391 -0.16194994 -29995.652 -16173.548 303.05972
9000 356.54987 0.09 8.7976293 0.07863788 0.066336597 -29808.679 -16145.52 299.1521
10000 322.27974 0.1 8.7883277 0.071221379 0.14441091 -30013.2 -16120.017 295.91005
11000 288.39697 0.11 8.7161044 0.12374144 0.057888762 -29659.115 -16093.755 293.76039
12000 254.94453 0.12 8.4664141 0.11590022 0.053137264 -28784.839 -16072.727 302.16151
13000 222.10061 0.13 8.0312734 0.15479095 -0.00030987981 -27285.848 -16045.735 298.09456

```

14000	189.48254	0.14	7.7593529	-0.067589459	0.023748449	-25718.373	-16021.048	296.6428
15000	157.24164	0.15	7.9620057	0.01935174	0.050888236	-26774.152	-15999.543	298.13657
16000	125.28295	0.16	7.9896281	-0.048697529	-0.2138625	-25756.893	-15981.117	305.28058
17000	93.654386	0.17	8.2825068	-0.14928122	-0.14198715	-26637.461	-15957.539	304.10016
18000	62.183767	0.18	8.4965527	-0.13383076	-0.20882948	-27179.641	-15925.861	289.97497
19000	30.970483	0.19	8.7027568	0.038033547	0.10172549	-29475.053	-15906.179	300.92811
20000	0	0.2	-4.1421569	-0.021888035	-0.25205478	14720.332	-16246.264	491.39709

Loop time of 618.338 on 1 procs for 20000 steps with 4000 atoms

99.1% CPU use with 1 MPI tasks x 1 OpenMP threads

Performance: 5.589 ns/day 4.294 hours/ns 32.345 timesteps/s

MPI task timings breakdown:

Section | min time | avg time | max time | %varavg | %total

```

-----
Pair | 596.11 | 596.11 | 596.11 | 0.0 | 96.41
Neigh | 0.89945 | 0.89945 | 0.89945 | 0.0 | 0.15
Comm | 2.4723 | 2.4723 | 2.4723 | 0.0 | 0.40
Output | 0.70232 | 0.70232 | 0.70232 | 0.0 | 0.11
Modify | 17.229 | 17.229 | 17.229 | 0.0 | 2.79
Other | | 0.9249 | | | 0.15

```

Nlocal: 4000 ave 4000 max 4000 min

Histogram: 1 0 0 0 0 0 0 0 0

Nghost: 7625 ave 7625 max 7625 min

Histogram: 1 0 0 0 0 0 0 0 0

Neighs: 326047 ave 326047 max 326047 min

Histogram: 1 0 0 0 0 0 0 0 0

FullNeighs: 652353 ave 652353 max 652353 min

Histogram: 1 0 0 0 0 0 0 0 0

Total # of neighbors = 652353

Ave neighs/atom = 163.088

Neighbor list builds = 29

Dangerous builds = 0

# clearing fixes and dumps

```

unfix          1
unfix          2
unfix          writer
undump          1
undump          2
#####
print "All done"
All done

```

### c) A copy of The Fe.deform file for SS304 under Ambient condition

# Fix print output for fix writer

0.00123999999999994	0.116564402264013	0.0464473137802112	0.00483803562523464
0.00248999999999981	0.210664407775859	0.0858898567310265	-0.0709971455330863
0.00373999999999987	0.421341288008089	0.00823323158588431	0.0164441171243528
0.00498999999999994	0.688853553139099	0.0761472295910508	-0.0350464974244329
0.00623999999999998	0.800749381530345	-0.0809253302455162	0.0287497894857198
0.00748999999999987	0.910864019197009	0.11111911577158	-0.0260790839192865
0.00873999999999994	1.05752203264959	0.0033984323810364	0.0787816266495031
0.00998999999999998	1.20817284939227	0.111533102518238	-0.0278485424353967
.	.	.	.
.	.	.	.
.	.	.	.
0.16499	8.12468386732701	-0.122944433536806	-0.0629838339958507
0.16624	8.11121348645094	-0.0384931493606099	0.027073254269727
0.16749	8.22193204181988	0.0132259402227129	0.016886999119873

0.16874	8.18549920458727	-0.0954506289353622	-0.034732462635077
0.16999	8.28257759850691	-0.149282498303458	-0.141988368546309
0.17124	8.16345362543331	-0.0517945740057542	0.212603558695045
0.17249	8.28532678775858	0.0973838026767817	-0.0556655732552118
0.17374	8.33910632558225	0.0596424427678164	0.127755425697117
0.17499	8.35843778172521	0.0476820982142403	0.0354455163312715
0.17624	8.51631398059371	-0.00437531520986944	-0.0202301738650157
0.17749	8.46420804508895	0.00466010646728243	-0.0613997507025128
0.17874	8.37424278825909	0.0605217673410995	0.123093211465606
0.17999	8.49662466993194	-0.133831893335373	-0.208831248122214
0.18124	8.527957214023	0.030841747126963	0.0865655139947751
0.18249	8.52155398857506	0.165568812827459	0.158139344473259
0.18374	8.59531778441364	-0.0311383408288015	-0.0757330534870769
0.18499	8.60876451235429	-0.0665652530762197	-0.0622507067245766
0.18624	8.6965311777411	0.0923774166672753	0.00485308358310499
0.18749	8.61297499331869	0.02197279695611	0.149731469725766
0.18874	8.82854342641751	-0.0310480018312249	-0.155761526898982
0.18999	8.70282992130393	0.0380338668337344	0.101726343363716
0.19124	8.72246972603824	0.10215769205209	0.129522289471954
0.19249	8.70457054346254	-0.104732146381689	-0.208038310710638
0.19374	8.50732843319348	0.118066390027674	-0.106694703945573
0.19499	7.84998792874669	0.954151930411956	-0.217671611946641
0.19624	2.65161285144032	5.13773233925456	-2.72628959691421
0.19749	-2.52303837908483	2.15217169535593	-1.82216890834444
0.19874	-4.45373027963355	-0.372475631916491	0.25491075346315
0.19999	-4.14219144687075	-0.0218882176094841	-0.252056883048852

## APPENDIX VII

### Mechanical Properties of the Fe-Ni-Cr Alloys under ambient temperature and supercritical water conditions

SPECIMEN TESTING CONDITION	YOUNGS MODULUS (E) (GPa)				ULTIMATE TENSILE STRENGTH (UTS)(GPa)				BREAKING STRENGTH(GPa)			
	304	308	309	316	SS304	SS308	SS309	SS316	SS304	SS308	SS309	SS316
<b>27 °C</b>	196	196	196	196	10.55 (0.07%)	10.53 (0.06%)	10.49 (0.06%)	10.46 (0.06%)	8.71 (0.19%)	8.72 (0.20%)	8.67 (0.193%)	8.84 (0.19%)
<b>300 °C</b>	156	157	154	155	7.76 (0.07%)	7.72 (0.09%)	7.77 (0.07%)	7.66 (0.07%)	6.7 (0.16%)	6.57 (0.16%)	6.50 (0.154%)	6.56 (0.15%)
<b>400 °C</b>	139	139	136	137	7.10 (0.08%)	6.96 (0.09%)	6.84 (0.07%)	6.82 (0.07%)	6.25 (0.15%)	6.01 (0.15%)	6.05 (0.148%)	6.13 (0.15%)
<b>500 °C</b>	121	119	118	119	6.26 (0.11%)	6.34 (0.14%)	6.07 (0.10%)	6.15 (0.08%)	5.80 (0.15%)	5.75 (0.15%)	5.72 (0.143%)	5.77 (0.14%)

Note: The values in the bracket are the corresponding strain values of UTS and Breaking Strength.

## Yield Strength of the Fe-Ni-Cr Alloys under ambient temperature and supercritical water condition

SPECIMEN TESTING CONDITION	YIELD STRENGTH (GPa)			
	SS304	SS308	SS309	SS316
<b>AMBIENT CONDITIONS</b>	9.88	9.90	9.97	9.77
<b>T=27 °C</b>	(0.07%)	(0.07%)	(0.07%)	(0.07%)
<b>P=0.01 MPa (1atm)</b>				
<b>SCW Condition</b>	7.56	7.38	7.46	7.33
<b>T = 300 °C</b>	(0.07%)	(0.07%)	(0.06%)	(0.07%)
<b>P = 25 MPa</b>				
<b>SCW Condition</b>	6.39	6.20	6.17	6.12
<b>T = 400 °C</b>	(0.07)	(0.06%)	(0.05%)	(0.06%)
<b>P = 25 MPa</b>				
<b>SCW Condition</b>	5.54	5.10	5.30	5.34
<b>T = 500 °C</b>	(0.06%)	(0.06%)	(0.05%)	(0.06%)
<b>P = 25 MPa</b>				